CORROSION-INDUCED FAILURE ANALYSIS OF Cu WIRE BONDED PACKAGES

By

Yuelin Wu

A DISSERTATION

Submitted to
Michigan State University
in partial fulfillment of the requirements
for the degree of

Chemical Engineering – Doctor of Philosophy

2018

ABSTRACT

CORROSION-INDUCED FAILURE ANALYSIS OF Cu WIRE BONDED PACKAGES

By

Yuelin Wu

Due to the demand of cost reduction and higher input-output density in the integrated circuit (IC), Cu has become the material of choice over Au in the wire bonded electronic package. Although high-quality Cu wire bonds can be achieved by modifying the bonding conditions and process parameters, the long-term service reliability of the Cu-Al ball-bond interface in humid condition remains a major concern, especially to the automobile industry. At the Cu-Al ball-bond interface, two thin layers of intermetallics, Cu_9Al_4 and $CuAl_2$, are sandwiched between the Cu wire and the Al pad. Accelerated humidity reliability tests showed Cu_9Al_4 disappeared, while Cu, $CuAl_2$, and Al remained. The disappearance of Cu_9Al_4 cannot be explained based on the nobility ranking of the metallic entities present. Consequently, the corrosion-induced failure mechanism of the Cu-Al ball-bond interface remains unclear. This dissertation focuses on understanding the preferential attack on Cu_9Al_4 and its role in the ball-bond failure by using electrochemical and non-electrochemical techniques. Corrosion-mitigating mechanisms of current solutions can also be explained.

Galvanic corrosion is considered as a major cause of bond failure due to the direct contact between dissimilar metallic entities at the ball-bond interface. Due to encapsulation, the galvanic corrosion should occur in a thin layer of the electrolyte at the mold-bond interface. The high ohmic resistance of this thin-layer electrolyte may constrain the galvanic corrosion at the contact interfaces between adjacent entities. Galvanic current density measurements showed the galvanic corrosion rate was higher between Cu_9Al_4 and $CuAl_2$ than those between Cu and Cu_9Al_4 as well as between $CuAl_2$ and Al. A crack should propagate faster along the interface between Cu_9Al_4

and $CuAl_2$. A large area of residual alumina, which originates from the Al pad, is found between Cu_9Al_4 and $CuAl_2$. Due to weak bonding between alumina and the intermetallics, the electrolyte can seep in more easily and accelerate the corrosion-induced crack growth. Due to the influx of Cu, $CuAl_2$ is slowly transformed to Cu_9Al_4 during the annealing. Voids form within the residual alumina between Cu_9Al_4 and $CuAl_2$ due to internal stress buildup. These voids between Cu_9Al_4 and $CuAl_2$ can also facilitate the crack propagation. Therefore, the Cu-Al ball bond should fail at the interface between Cu_9Al_4 and $CuAl_2$. The failure separates Cu and Cu_9Al_4 from $CuAl_2$ and Al. For the Cu-Cu_9Al_4 couple, Cu_9Al_4 the anode should corrode much faster due to strong galvanic effect imposed by a larger area of Cu. For the $CuAl_2$-Al couple, Al the anode should not be affected since the galvanic effect imposed by a small area of $CuAl_2$ is weak. Therefore, Cu_9Al_4 appears to corrode faster than Cu, $CuAl_2$, and Al.

Pd-coated Cu wire and the "green" molding compound with a low chloride concentration are commonly used to mitigate the bond corrosion. Galvanic current density measurements showed that reducing the chloride concentration lowered the galvanic corrosion rate between Cu_9Al_4 and $CuAl_2$ due to a lower anodic dissolution rate of $CuAl_2$. On the contrary, Pd addition increased the galvanic corrosion rate between Cu_9Al_4 and $CuAl_2$ due to a higher cathodic activity of Cu_9Al_4. But, Pd reduces the intermetallic growth rate and the associated internal stress buildup. The improved bond strength outweighs the increasing galvanic corrosion rate and leads to a lower bond failure rate.

ACKNOWLEDGEMENTS

I am extremely grateful to my advisor Dr. Andre Lee for providing me the opportunity to study in MSU and equipping me with the necessary tools to tackle difficulties I face in research and life in general. I am grateful to Dr. Scott Barton and Dr. Donald Morelli for their generosity in providing lab equipment. I would also like to express my sincere gratitude and appreciation to Dr. Mathew Varughese from NXP Semiconductors, Dr. Kejun Zeng from Texas Instruments (TI), and Semiconductor Research Corporation (SRC). This work would not have been done without their intellectual guidance and financial support.

TABLE OF CONTENTS

LIST OF TABLES vii

LIST OF FIGURES viii

CHAPTER 1 INTRODUCTION AND RESEARCH STRATEGIES 1
1.1 Electronic Packaging Hierarchy 1
1.1.1 Wire Bonding 1
1.1.2 Flip Chip Bonding 4
1.1.3 Tape Automated Bonding 7
1.1.4 A Comparison of Wire Bonding, Flip Chip Bonding, and TAB 9
1.2 A Comparison between Cu wire and Au wire 10
1.3 Processing Concerns of Cu Wire Bonding 11
1.3.1 Oxidation 11
1.3.2 Hardness 12
1.4 Service Reliability Concerns of Cu Wire Ball Bonds 12
1.4.1 Thermal Reliability 13
1.4.2 Humidity Reliability 13
1.5 Current Corrosion-mitigating Strategies 15
1.5.1 Wire Metallization 15
1.5.2 Pad Metallization 18
1.5.3 Molding Compound Chemistry 19
1.5.4 IMC Coverage 20
1.6 Problem Statements and Research Strategies 21

CHAPTER 2 SAMPLE PREPARATION, EXPERIMENTAL TECHNIQUES, AND DATA ANALYSIS 23
2.1 Sample Preparation 23
2.2 XRD Analysis on (Pd-doped) IMCs 25
2.3 Electrochemical Characterization 25
2.3.1 Working Electrode Preparation 25
2.3.2 Electrolyte Preparation 26
2.3.3 Open Circuit Potential Measurement 27
2.3.4 Potentiodynamic Polarization Measurement 28
2.3.5 Zero Resistance Ammetry 33
2.4 Mass Loss Experiment 34

CHAPTER 3 ELECTROCHEMICAL STUDIES OF THE METALLIC ENTITIES AT THE BALL-BOND INTERFACE 36
3.1 Introduction 36
3.2 Results and Discussion 36
3.2.1 XRD Pattern Analysis 36
3.2.2 Corrosion Behavior of Cu, γ, θ, and Al 37
3.2.3 Synergic Effect of Pd and Chloride 41

3.2.4 Synergic Effect of pH and Pd 49
3.2.5 Synergic Effect of Temperature and Pd 55
3.3 Conclusions 61
3.3.1 Pd and Chloride Effect 61
3.3.2 Pd and pH Effect 63
3.3.3 Pd and Temperature Effect 64

CHAPTER 4 FAILURE MECHANISM OF THE Cu-Al BALL-BOND INTERFACE 66
4.1 Introduction 66
4.2 Results and Discussion 67
4.2.1 Mass Loss Experimental of the Cu-γ-θ-Al Galvanic System 67
4.2.2 Polarization Analysis of the Cu-γ-θ-Al Galvanic System 69
4.2.3 Crack Propagation between γ and θ: Galvanic Corrosion under Ohmic Control 75
4.2.4 Crack Propagation between γ and θ: Residual Alumina and Stress Buildup 77
4.2.5 Corrosion Mechanism of an Encapsulated Cu Ball Bond Interface 78
4.3 Conclusions 79

CHAPTER 5 PALLADIUM AND CHLORIDE EFFECT ON THE BOND FAILURE MECHANISM AND RATE 81
5.1 Introduction 81
5.2 Results and Discussions 81
5.2.1 Chloride Effect on the i_g Values 81
5.2.2 Chloride Effect on the Bond Failure Mechanism and Failure Rate 85
5.2.3 Pd Effect on the i_g Values 88
5.2.4 Pd Effect on the Bond Failure Mechanism and Failure Rate 92
5.2.5 i_g*(CuPd:Pd-doped γ)* at Low Chloride Concentration and High Pd Addition 94
5.3 Conclusions 95

CHAPTER 6 SUMMARY AND RECOMMENDATIONS 97
6.1 Summary 97
6.2 Recommendations 99

APPENDICES 100
APPENDIX A: Electrochemical Characterizations of Cu-Ni Alloy and Ni-doped γ 101
APPENDIX B: Pd Effect on the Electrochemical Behavior of Cu and γ in a Bromide-containing Solution 104
APPENDIX C: Electrochemical Behavior of (Pd-doped) Cu and γ in a Water Extract of the Molding Compound 106
APPENDIX D: Galvanic Corrosion Rate between Adjacent Entities as Influenced by Oxygen 111

REFERENCES 115

LIST OF TABLES

Table 1.1 Properties of Au and Cu [12] (©2012 IEEE).....11

Table 1.2 Standard testing conditions for common thermal and humidity reliability tests.....13

Table 2.1 Nominal composition of the samples used.....25

Table 4.1. Fractional mass loss of Cu, γ, θ, and Al ingots after two-week immersion under galvanic coupling.....68

Table 4.2. Fractional mass loss of each entity after five weeks of immersion in a pH 6, 20ppm NaCl solution.....76

Table 5.1 The stabilized values of i_g at 12 hour-point in solutions containing different chloride concentrations.....83

Table 5.2 Pd effect on the values of i_g(Cu:γ) and i_g(γ:θ) at 12-hour point in a near neutral 20ppm NaCl solution.....90

Table A.1 Vickers hardness of the Cu-Ni and Cu-Pd alloys.....101

Table C.1 Comparison of measured solution resistance.....107

LIST OF FIGURES

Figure 1.1 A typical wedge-wedge bonding process: step 1-3 illustrate the first wedge bond formation, step 4-5 illustrate the second wedge bond formation, step 6 shows wire beak-off. [3] (copy with permission from McGraw-Hill Education).....2

Figure 1.2 A typical ball-wedge bonding process: step 1-3 illustrate the ball bond formation, step 4-6 illustrate the wedge bond formation, step 7 shows the wire beak-off. [3] (copy with permission from McGraw-Hill Education).....3

Figure 1.3 C4 and C2 bump formation by the electroplating method [4] (copy with permission from ASME Publications).....5

Figure 1.4 A typical bonding process with a C4 flip chip [6] (©2004 IEEE).....6

Figure 1.5 Typical layout of a TAB tape (updated from [7] (©1987 IEEE).....7

Figure 1.6 TAB bonding process (a) inner lead bonding (ILB) and (b) outer lead bonding (OLB) (redrawn from [8]).....8

Figure 1.7 Three common types of TAB tapes: (a) one-layer, (b) two-layer, and (c) three-layer (redrawn from [9]).....9

Figure 2.1 Working electrode with a known exposed surface area (color online). The sample was first soldered to a Cu wire for electrical connection and then encapsulated in an epoxy resin. A portion of specimen surface was exposed by the standard metallographic preparation.....26

Figure 2.2 Two-electrode setup for the open circuit potential measurement.....28

Figure 2.3 Three-electrode configuration for the potentiodynamic polarization measurements...28

Figure 2.4 The instantaneous potential increase, ΔE, and decrease, $\Delta E'$ in one current pulse in the current interrupt method. Either ΔE and $\Delta E'$ can be divided by the applied current, 5μA to obtain the R_{soln} value.....29

Figure 2.5 (a) cathodic polarization curves of Cu obtained from one-way sweep (black) and two-way sweep (red); (b) anodic polarization curves of Cu obtained from one-way sweep (black) and two-way sweep (red). The electrolyte was 20 ppm NaCl with a pH level of 6.....31

Figure 2.6 Experimental setup for the ZRA measurement.....34

Figure 2.7 Four-metal mass loss experimental setup. The electrolyte used was 20ppm NaCl solution of pH 6.....35

Figure 3.1 XRD spectra of powdered (a) γ IMCs and (b) θ IMCs; the powder was made from the as-produced samples via arc melting. γ #1 and θ #1 were made with pure Cu. γ #2 and θ #2 were

made with Cu-2Pd alloy. γ #3 and θ #3 were made with Cu-9Pd alloy. Orientation effect was observed for γ #3 because its high ductility made powder preparation more difficult.....37

Figure 3.2 Cathodic polarization curves of Cu, γ, θ, and Al. All the polarization curves were measured in a 20 ppm NaCl electrolyte with a nearly neutral pH.....38

Figure 3.3 (a) Anodic polarization curves of Cu and Al. (b) Anodic polarization curves of γ and θ. "Breakdown" points and values of the Tafel slopes are marked in the figure.....40

Figure 3.4 Polarization curves of Cu, Cu-2Pd, and Cu-9Pd in near neutral electrolyte solution containing (a) 100ppm NaCl, (b) 20ppm NaCl, (c) 1ppm NaCl. The values of potential were corrected by R_{soln}, and the linear regime of the cathodic branch was extrapolated back to E_{oc} to obtain i_{corr}.....42

Figure 3.5 E_{corr} and log i_{corr} of Cu, Cu-2Pd, and Cu-9Pd in a nearly neutral electrolyte solution of different NaCl concentrations (■: 100ppm; ●: 20ppm; ▲: 1ppm).....43

Figure 3.6 Polarization curves of γ #1, γ #2, and γ #3 in near neutral electrolyte containing (a) 100ppm NaCl, (b) 20ppm NaCl solution, (c) 1ppm NaCl. The potentials were corrected by R_{soln}, and the linear regime of the anodic branch was extrapolated back to E_{oc} to obtain i_{corr}.....45

Figure 3.7 E_{corr} and log i_{corr} of γ #1, γ #2 and γ #3 in near neutral electrolyte of different NaCl concentrations (■: 100ppm; ●: 20ppm; ▲: 1ppm).....47

Figure 3.8 Polarization curves of θ #1, θ #2, and θ #3 in near neutral electrolyte containing 100ppm NaCl.....48

Figure 3.9 Effect of pH on the polarization curves of (a) Cu, (b) Cu-2Pd, (c) Cu-9Pd in a 20ppm NaCl solution. The i_{corr} values were obtained by extrapolating the linear regimes of the cathodic polarization curves back to E_{oc}.....49

Figure 3.10 E_{corr} and log i_{corr} of Cu and Cu-Pd alloys in a 20ppm NaCl solution (■: pH=9; ●: pH=6; ▲: pH=4).....50

Figure 3.11 Effect of pH on the polarization curves of (a) γ #1, (b) γ #2, (c) γ #3 in the 20ppm NaCl. The values of i_{corr} were obtained by extrapolating the linear regimes of the anodic polarization curves back to E_{oc}.....53

Figure 3.12 E_{corr} and log i_{corr} of γ #1, γ #2 and γ #3 in a 20ppm NaCl solution (■: pH=9; ●: pH=6; ▲: pH=4).....54

Figure 3.13 Effect of temperature on the polarization curves of (a) Cu, (b) Cu-2Pd, (c) Cu-9Pd in a 20ppm NaCl solution. The values of i_{corr} were obtained by extrapolating the linear regimes of the cathodic polarization curves back to E_{oc}.....56

Figure 3.14 E_{corr} and log i_{corr} of Cu and Cu-Pd alloys in the 20ppm NaCl solution (■: 25°C; ●:45°C; ▲:65°C)..... 57

Figure 3.15 Effect of temperature on the polarization curves of (a) γ #1, (b) γ #2, (c) γ #3 in the 20ppm NaCl. The values of i_{corr} were obtained by extrapolating the linear regimes of the anodic polarization curves back to E_{oc}.....60

Figure 3.16 E_{corr} and log i_{corr} of γ #1, γ #2 and γ #3 in the 20ppm NaCl solution (■: 25°C; ●:45°C; ▲:65°C).....61

Figure 4.1 The outer surface of Cu, γ, θ, and Al ingots before and after two weeks of immersion in a near neutral 20 ppm NaCl solution.....67

Figure 4.2 (a) E_{oc} and (b) i_{corr} values of Cu, γ, θ, and Al.....69

Figure 4.3 Evaluate the anodic dissolution current density i_a of Cu, γ, θ, and Al when they form a four-metal galvanic system. It was assumed that all the entities corroded at $E_{oc,Cu}$. Values of $i_{a,Cu}$ and $i_{a,\gamma}$ were obtained by the linear extrapolation, while values of $i_{a,\theta}$ and $i_{a,Al}$ were obtained directly from their anodic polarization curves.....71

Figure 4.4 Anodic dissolution current density i_a of each entity after the crack at the Cu-γ interface separating Al from the other entities. $i_{a,Cu}$ was obtained by extrapolating the linear regime of its anodic polarization curve to $E_{oc,Cu}$. $i_{a,\gamma}$, $i_{a,\theta}$, and $i_{a,Al}$ was obtained by extrapolating linear regimes of their anodic polarization curves to $E_{oc,Al}$. $i_{a,Al}$ turns out to be the highest among all the entities.....72

Figure 4.5 Anodic current density i_a of each entity after the crack propagates across the interface between γ and θ. $i_{a,Cu}$ and $i_{a,\gamma}$ were obtained by extrapolating the linear regimes of their anodic polarization curves to $E_{oc,Cu}$. $i_{a,\theta}$ and $i_{a,Al}$ was obtained by extrapolating the linear regimes of their anodic polarization curves to $E_{oc,Al}$. $i_{a,\gamma}$ turns out to be the highest among all the entities, which is consistent with the observed disappearance of γ.....73

Figure 4.6 Anodic current density i_a of each entity after the crack propagates across the interface between θ and Al. $i_{a,Cu}$ and $i_{a,\gamma}$ were obtained by extrapolating the linear regimes of their anodic polarization curves to $E_{oc,Cu}$. $i_{a,\gamma}$ was directly obtained from its anodic polarization curve. $i_{a,Al}$ was obtained by extrapolating the linear regime of its anodic polarization curve to $E_{oc,Al}$. $i_{a,\theta}$ turns out to be the highest among all the entities.....74

Figure 4.7 Values of $i_{g,Cu-\gamma}$, $i_{g,\gamma-\theta}$, and $i_{g,\theta-Al}$ as a function of the immersion time in a near neutral 20ppm NaCl solution.....75

Figure 4.8 Corrosion behavior of an encapsulated Cu-Al ball bond interface. Step 1: cracks preferentially propagate along the interface between two adjacent entities due to the ohmic control. Step 2: the crack propagates much faster along the interface between γ and θ due to a higher i_g value. Step 3: As the metal erodes away and dissolves in the electrolyte, the ohmic effect is weakened. However, the crack continues propagating fast between γ and θ until bond failure due to the high anodic polarization imposed on θ and interfacial defects between them. Step 4: γ disappears due to the galvanic effect imposed by a large area of the cathode Cu.....79

Figure 5.1 (a) values of i_g(Cu:γ), (b) values of i_g(γ:θ), (c) values of i_g(θ:Al) with the immersion time measured in solutions containing 100ppm, 20ppm, and 1ppm NaCl.....82

Figure 5.2 The mixed potential plot for the γ-θ galvanic couple in a near neutral 20 ppm NaCl solution. The current density at the crossover, i_{couple} equals the galvanic current density, $i_g(\gamma:\theta)$ measured via ZRA based on the mixed potential theory.....84

Figure 5.3 Values of i_{couple} obtained from the crossovers of the anodic polarization curves of θ and the cathodic polarization curves of γ measured in 100ppm, 20ppm, and 1ppm NaCl solutions of pH 6. The i_{couple} value decreased with a decreasing chloride concentration due to the decrease in the anodic current density of θ. This explains why $i_g(\gamma:\theta)$ decreased with a decreasing chloride concentration in the ZRA measurement.....85

Figure 5.4 Anodic polarization curves of Cu, γ, θ, and Al measured in a 100ppm NaCl solution. The i_a values of all entities were obtained by linear extrapolation methods and marked in the figure.....86

Figure 5.5 Anodic polarization curves of Cu, γ, θ, and Al measured in a 20ppm NaCl solution. The i_a values of all entities were obtained by linear extrapolation methods and marked in the figure.....87

Figure 5.6 Anodic polarization curves of Cu, γ, θ, and Al measured in a 1ppm NaCl solution. The i_a values of all entities were obtained by linear extrapolation methods and marked in the figure.....88

Figure 5.7 (a) values of i_g(CuPd:Pd-doped γ) and (b) values of i_g(Pd-doped γ:θ) measured in a 20ppm NaCl solution.....89

Figure 5.8 Values of i_{couple} obtained from the intercepts between the anodic polarization curves of θ and the cathodic polarization curves of γ #1, γ #2, and γ #3 measured in a near neutral 20ppm NaCl solutions. The i_{couple} value increased with an increasing Pd addition in γ due to the increase in the cathodic current density 90

Figure 5.9 Values of i_{couple} obtained from the intercepts between the anodic polarization curves of Cu, Cu-2Pd, and Cu-9Pd and the cathodic polarization curves of γ #1, γ #2, and γ #3 measured in a near neutral 20ppm NaCl solutions. The i_{couple} values were marked in the figure. The i_{couple} value did not consistently decrease with Pd addition like the i_g value due to the overestimation of the cathodic current density of the Cu-Pd alloys.....91

Figure 5.10 (a) Anodic polarization curves of Cu-2Pd, γ #2, θ, and Al, (b) Anodic polarization curves of Cu-9Pd, γ #3, θ, and Al. All the polarization curves were measured in a 20ppm NaCl solution. The i_a values of all entities were obtained by linear extrapolation methods and marked in the figure.....93

Figure 5.11 the value of i_g(Cu-9Pd:γ#3) as a function of the immersion time in a 1ppm NaCl solution.....95

Figure A.1 XRD spectra of powdered Ni-doped (a) γ and (b) θ; the powder was made from the as-produced samples via arc melting. Ni-doped IMCs were prepared using the Cu-1Ni alloy...102

Figure A.2 Anodic and cathodic polarization curves of Cu and Cu-1Ni alloy measured in a pH 6, 20ppm NaCl solution.....103

Figure A.3 Anodic and cathodic polarization curves of undoped γ and Ni-doped γ measured in a pH 6, 20ppm NaCl solution. The Ni-doped γ was prepared using Cu-1Ni alloy.....103

Figure B.1 Anodic and cathodic polarization curves of Cu, Cu-2Pd, and Cu-9Pd measured in a pH 6, 20ppm NaBr solution.....105

Figure B.2 Anodic and cathodic polarization curves of γ #1, γ #2, and γ #3 measured in a pH 6, 20ppm NaBr solution.....105

Figure C.1 Anodic and cathodic polarization curves of (a) Cu, (b) Cu-2Pd, and (3) Cu-9Pd measured in the water extract of EMC, 20ppm NaCl solution, and 1ppm NaCl solution.....108

Figure C.2 Anodic and cathodic polarization curves of (a) γ #1, (b) γ #2, and (3) γ #3 measured in the water extract of EMC, 20ppm NaCl solution, and 1ppm NaCl solution.....109

Figure D.1 Galvanic current density of (a) Cu:γ #1couple, (b) Cu-2Pd:γ #2 couple, and (3) Cu-9Pd:γ #3 couple in a 20ppm NaCl electrolyte open to air and purged with nitrogen.....112

Figure D.2 Galvanic current density of (a) γ #1:θ couple, (b) γ #2:θ couple, and (3) γ #3:θ couple in a 20ppm NaCl electrolyte open to air and purged with nitrogen.....113

CHAPTER 1 INTRODUCTION AND RESEARCH STRATEGIES

1.1 Electronic Packaging Hierarchy

A simplified definition of the electronic packaging is the housing and interconnections of integrated circuit (IC) chips [1]. The housing protects the chip from the environment and the interconnections allow the power and signal flow to and from a chip. A typical electronic system consists of three levels of interconnection [1]. Level 0 refers to the gate-to-gate interconnection on an IC chip; Level 1 refers to the chip-to-substrate interconnection in a chip package; Level 2 refers to the interconnection between the chip packages and the printed circuit board. Level 0 packaging is accomplished during the IC fabrication. Level 1 and 2 packaging are achieved via similar technologies. The chip-to-substrate interconnection in level 1 packaging is the primary focus of this introduction. The following three technologies: wire bonding, flip chip bonding, and tape automated bonding (TAB), are commonly used to form a chip-to-substrate interconnection [1].

1.1.1 Wire Bonding

Wire bonding is an interconnection technology that joins a metallic wire with a metallic pad using a combination of heat, force, and ultrasonic energy [2]. Two types of wire bonds: ball-wedge bonds and wedge-wedge bonds, are commonly used [3]. The ball bonding is achieved by thermocompression or thermosonic bonding and the wedge bonding is achieved by thermosonic or ultrasonic bonding [3]. A typical wedge-wedge bonding process using ultrasonic bonding is described in Fig. 1.1 [3].

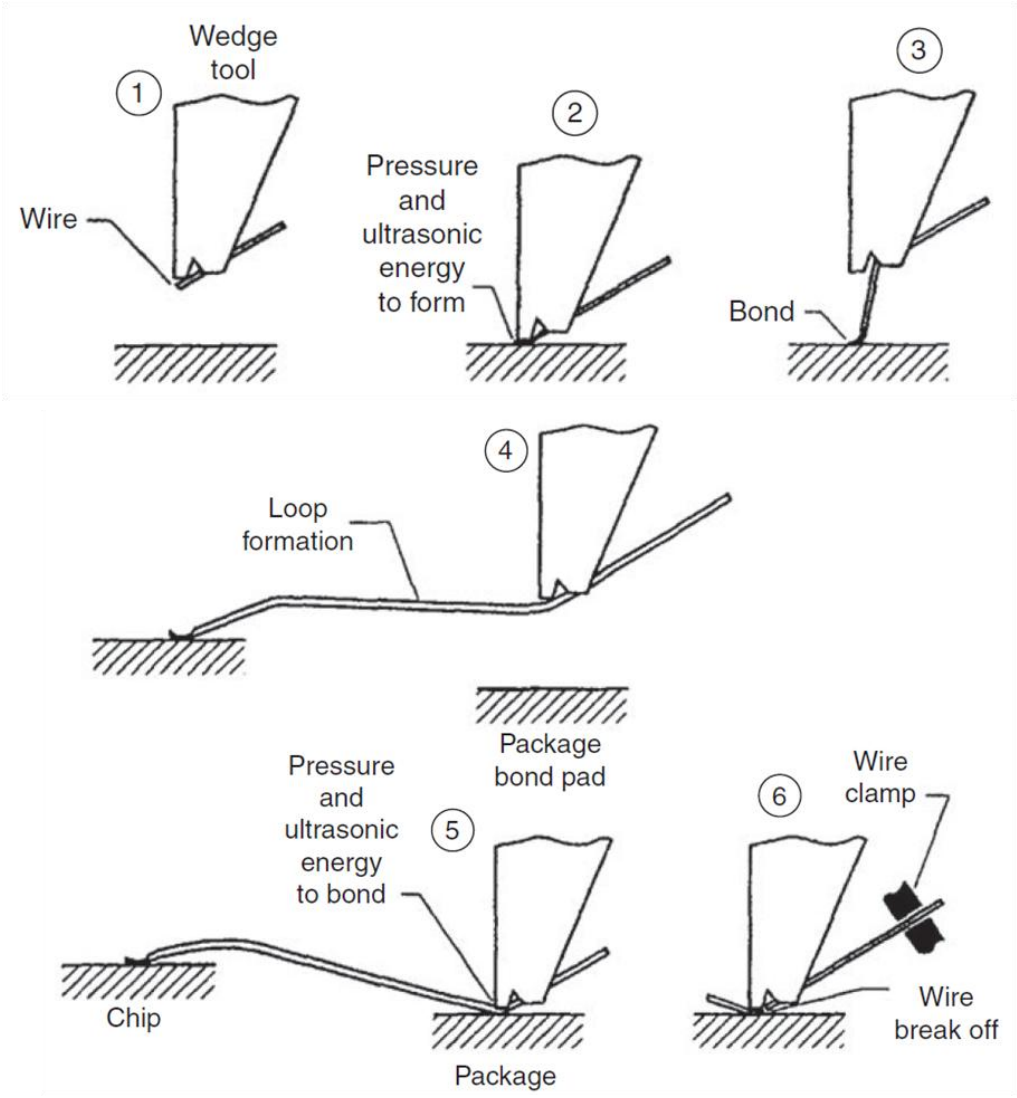

Figure 1.1 A typical wedge-wedge bonding process: step 1-3 illustrate the first wedge bond formation, step 4-5 illustrate the second wedge bond formation, step 6 shows the wire beak-off. [3] (copy with permission from McGraw-Hill Education)

A wire gripped by a wedge tool is lowered down to the first bonding site and pressed against the bond pad. Ultrasonic energy is applied to form the first bond. The wedge tool is raised and arrives at the second bonding site with a wire loop formed. The wedge tool is then lowered down with the wire and the second bond is formed using the same ultrasonic method. After the second bond has been formed, a wire clamp behind the wedge tool grips the wire tightly to beak it at the

heal of the second bond. A typical ball-wedge bonding process using the thermosonic bonding is described in Fig. 1.2 [3].

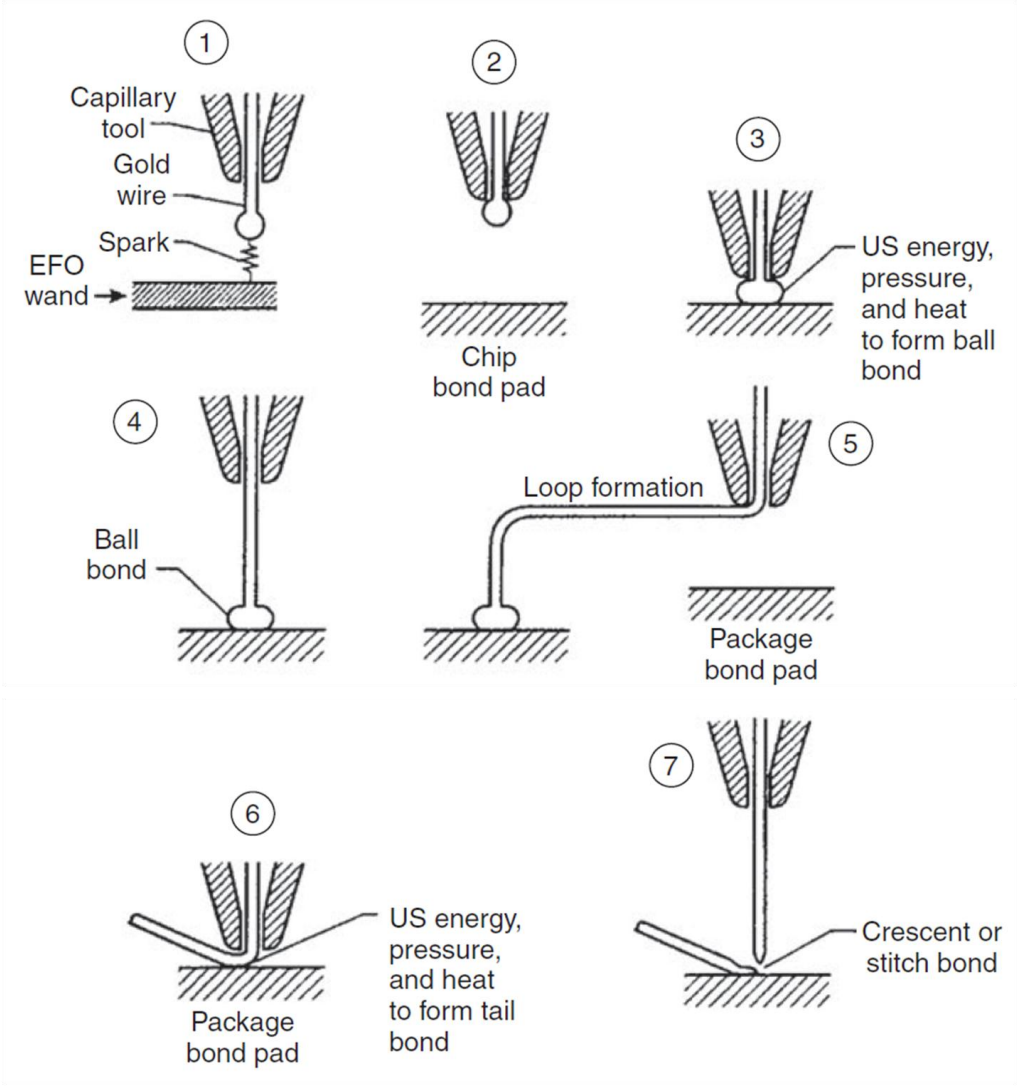

Figure 1.2 A typical ball-wedge bonding process: step 1-3 illustrate the ball bond formation, step 4-6 illustrate the wedge bond formation, step 7 shows the wire beak-off. [3] (copy with permission from McGraw-Hill Education)

A wire is fed through a capillary tool and an electrical flame-off (EFO) spark melts the wire tip. A free-air ball (FAB) forms. The wire is then retracted to position the FAB against the bottom of the capillary tool. The FAB is lowered with the capillary tool and pressed against a heated bond pad. Ultrasonic energy and pressure are applied to form the ball bond. The capillary

tool is raised and brings the wire to the second bonding site. The capillary tool is lowered and a wedge bond forms with the help of ultrasonic energy, heat, and pressure. After the wedge bond is made, the capillary tool is raised again and a wire clamp breaks the wire at the heel of the wedge bond. For the wedge-wedge bonding, the second bond needs to be mechanically aligned with the first bond to avoid bending or cracking the first bond [3]. For the ball-wedge bonding, the wire can be moved along all directions after the ball bonding. Thus, the wedge-ball bonding is much faster than the wedge-wedge bonding. Although the wedge-wedge bonds are preferred in fin-pitch and low-loop applications, such as microwaves and optoelectronics, the majority of wire bonds, especially gold (Au) or copper (Cu) wire bonds, are formed by ball-wedge bonding [2].

1.1.2 Flip Chip Bonding

Flip chip bonding is an interconnection technology that connects a chip to a substrate by an array of interconnect materials, such as solder bumps or metallic studs, using various methods, such as mass reflow or thermocompression bonding [4]. Unlike wire bonding that is performed on the peripheral area of a chip, flip-chip bonding can be performed on entire active surface of a chip, which significantly increases the number of the input/output (I/O) connection [5].

The mother technology of flip-chip bonding is wafer bumping [4]. The most common types of bumps are solder bumps, referred to as C4 bumps, and Cu pillars with solder caps, referred to as C2 bumps [4]. The C2 bumps are primarily used for fin-pitch applications since the Cu pillars can be made much thinner than the solder bumps [4]. C4 and C2 bumps are commonly formed by electroplating as shown in Fig. 1.3 [4].

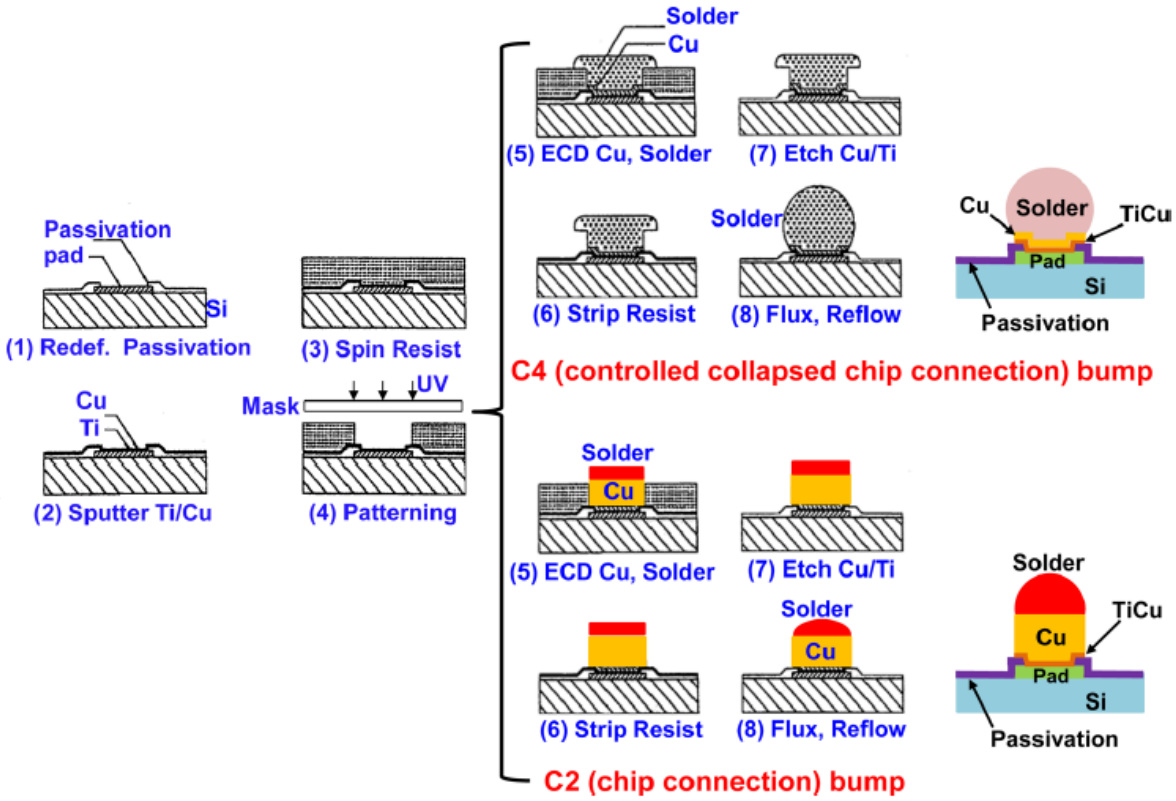

Figure 1.3 C4 and C2 bump formation by the electroplating method [4] (copy with permission from ASME Publications)

Before bumping, pad passivation and metallization are required. The pad metallization is prepared by depositing Ti or TiW (0.1 to 0.2 μm) and Cu (0.3 to 0.8 μm) via sputter deposition. This TiCu or TiWCu metallization is referred to as the "under bump metallurgy (UBM)". A thick layer of photoresist (40 μm) is overlaid to the UBM layer and exposed to ultraviolet light through a solder bump mask. The exposed photoresist is washed off to expose the UBM. For C4 bump formation, another Cu layer (5 μm) is deposited on the UBM using electroplating. The solder bumps are deposited on the Cu layer until they reach 15-20μm above the photoresist layer and form mushroom-like cross-sections. After bumping, the resist is stripped off and the exposed UBM layer outside the pad is etched off. The mushroom-shaped solder bumps undergo a mass reflow process and form 100μm truncated spherical bumps under the influence of the surface

tension. For C2 bump formation, after the photoresist patterning, the solder electroplating is replaced by the Cu electroplating. After the Cu pillars are formed, a small volume of solder is deposited on the top of the Cu pillar. The photoresist is stripped off and the solder is reflowed to form a solder cap.

A typical flip chip bonding process with C4 bumps is shown in Fig. 1.4 [6]. The substrate is patterned with bond pads in a matching footprint with the solder bump array on the chip. All the solder bumps and their matching pads are bonded simultaneously under heat and/or pressure. Flux cleaning is conducted before and after the bonding, respectively. The chip is positioned around 5mm apart from the substrate for the underfill to fill in.

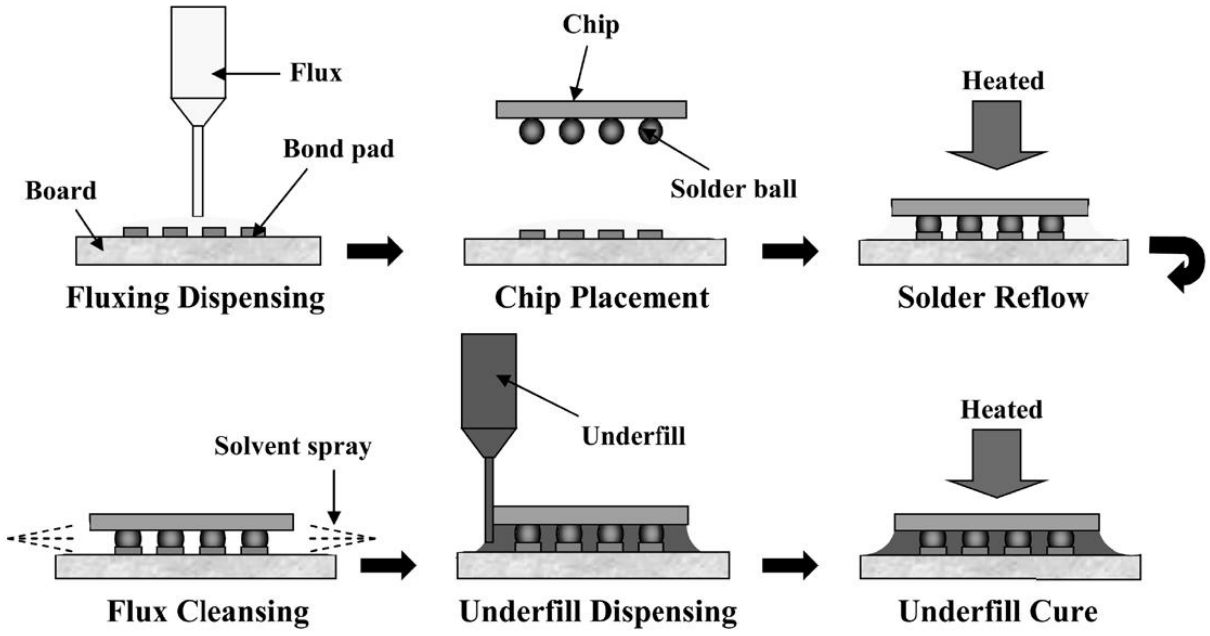

Figure 1.4 A typical bonding process with a C4 flip chip [6] (©2004 IEEE)

Applying underfill between the chip and the substrate is critical in maintaining the thermal mechanical stability of the solder bumps [6]. Due to the coefficient of thermal expansion (CTE) mismatch between the chip (2.5 ppm/°C) and the substrate (4-10 ppm/°C for ceramics and 18-24 ppm/°C for polymers), the bumps can undergo a large shear stress as the chip temperature rises

up during the in-use condition [6]. Underfill is commonly an epoxy-based resin filled with SiO_2 particles [6]. Cured underfill exhibits high modulus, low CTE, and good adhesion to the chip and the substrate, and thus effectively minimizes the shear force imposed at the bumps and improves their thermal mechanical reliability.

1.1.3 Tape Automated Bonding

Tape automated bonding (TAB) is an interconnection technology that connects the chip with an array of thin metallic leads, such as tin-plated Cu leads, taped on a polymeric film, such as polyimide. The layout of the tape is shown in Fig. 1.5 [7]. The metallic leads are held together by a polyimide ring. The inner ends of the leads are used to form interconnects on the chip and the outer ends of the leads are used to form interconnects on the substrate [8]. Therefore, each TAB process needs to go through two operations: inner lead bonding (ILB) and outer lead bonding (OLB) as illustrated in Fig 1.6a and 1.6b, respectively [8].

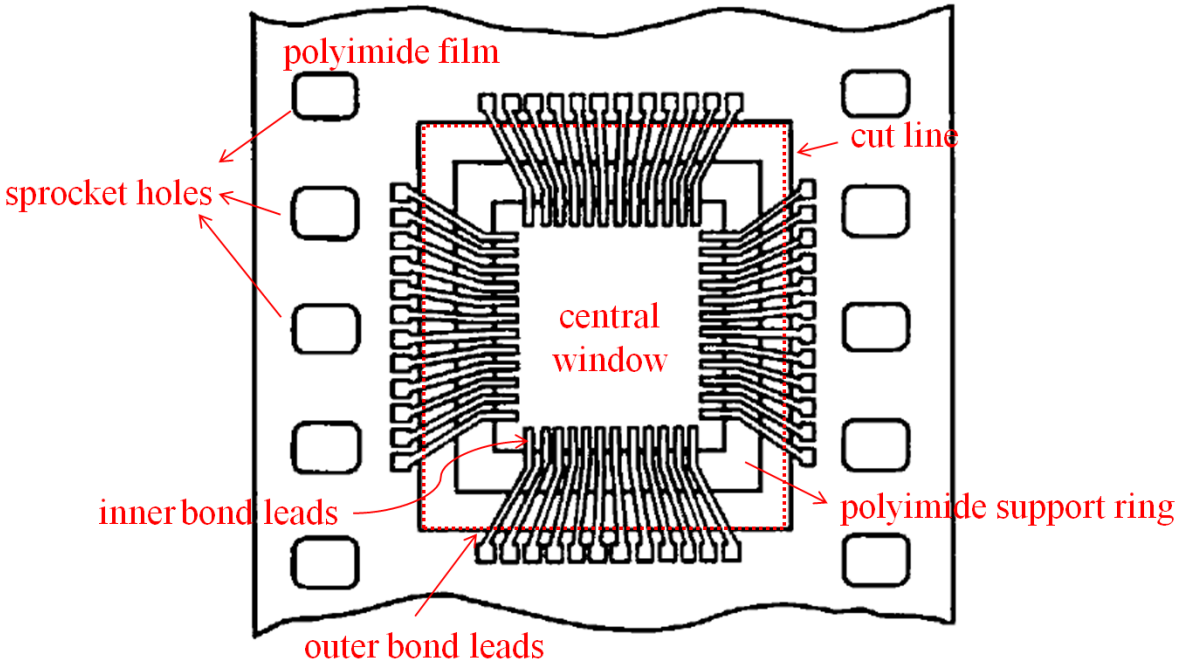

Figure 1.5 Typical layout of a TAB tape (updated from [7] ©1987 IEEE)

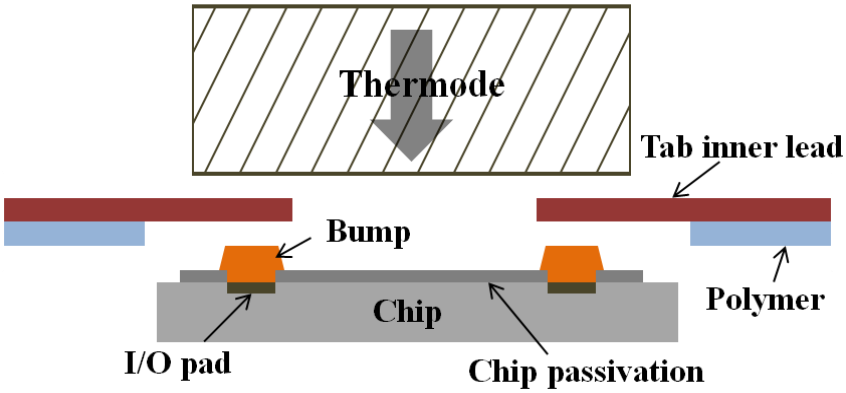

(a)

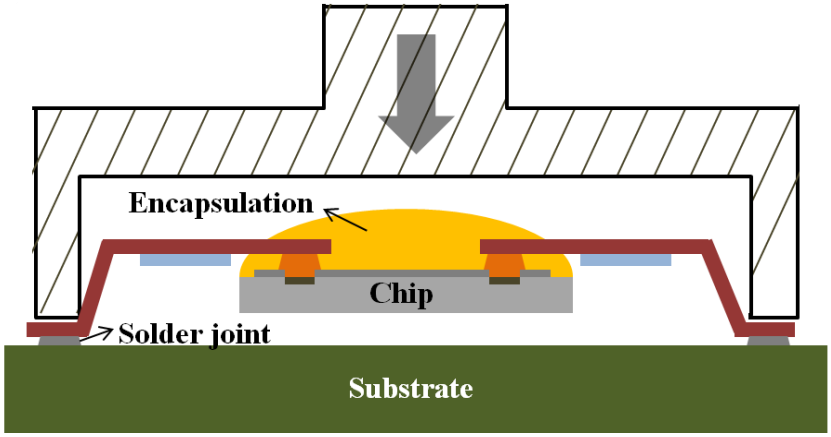

(b)

Figure 1.6 TAB bonding process (a) inner lead bonding (ILB) and (b) outer lead bonding (OLB) (redrawn from [8])

The chip is introduced to the inner lead cluster first. Thermocompression is applied from the back side to form interconnects. Similar to flip-chip bonding, all the interconnects are made in one operation, which is referred to as "gang bonding" [8]. After the ILB, the chip along with the as-formed interconnects is encapsulated and tested. If the chip passes the test, it will be cut from the tape along the cut line. Then, the outer leads are bonded with the substrate via a similar thermocompression method.

The TAB tape has three basic formats: one-layer, two-layer, and three-layer. The cross-sectional structures of these three types of tape are shown in Fig. 1.7 [9]. A typical one-layer tape

is a Cu foil (35-70 μm). A typical two-layer tape is made by sputtering a Cu layer (35 μm) onto a polyimide film (50-75 μm). A typical three-layer tape is made by sputtering a Cu layer (35 μm) or laminating a Cu foil onto a base polyimide film (75-125 μm) with an organic adhesive (13-25 μm).

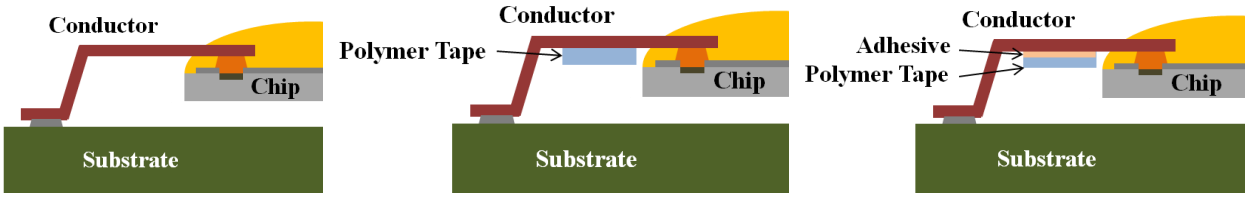

(a) (b) (c)

Figure 1.7 Three common types of TAB tapes: (a) one-layer, (b) two-layer, and (c) three-layer (redrawn from [9])

The one-layer tape is the least expensive among the three types. It is more suitable for low lead-count applications such as watches, blood pressure monitors, and car radios [9]. The two-layer tape offers better lead stability than the one-layer tape since all the leads are supported by a base film. This type of tape is commonly used in inject printers [9]. The three-layer tape has the highest lead stability since the supporting base film is much thicker than that in the two-layer tape. It can be used on large chips with wider and/or longer leads [9].

1.1.4 A Comparison of Wire Bonding, Flip Chip Bonding, and TAB

Wire bonding is the oldest and most mature technology for the chip-level interconnection. In recent years, demand for higher I/O density and better performance drives the development of flip chip bonding as an alternative to wire bonding [10]. Flip chip bonding utilizes the entire area of the chip, while wire bonding only operates in the peripheral area of the chip [5]. Thus, the I/O density can be much higher with the flip chip bonding. In addition, the conducting path of solder bumps or Cu pillars in flip chip bonding is much shorter than the wires in wire bonding [5]. This can reduce the inductance and switching noise, and improve performace [5]. Another advantage

of flip-chip bonding over wire bonding is the ability to achieve "gang bonding". In wire bonding, each wire needs to go through two operations: ball bonding and wedge bonding [3]. Additionally, all the wires need to be bonded individually. In flip-chip bonding, all the solder joints are formed in one operation. Due to the time-efficiency of "gang bonding", TAB emerged as an alternative to wire bonding as both the ILB and OLB are achieved via gang bonding [8]. However, TAB is not able to achieve a high I/O density like flip chip bonding since it can only utilize the peripheral area instead of the entire chip area [11].

Besides I/O counts and performance, cost is another important concern to the IC packaging industry. Wire bonding has a cost advantage over flip chip bonding and TAB when a moderate I/O count (<600) is sufficient [10]. Wire bonding does not require extra costly farbication steps, like wafer bumping for flip chip bonding and tape fabrication for TAB. In addition, wire bonding is much more flexible [5]. The autobonder can be easily reprogrammed to accommodate for any pad dimensional change or die downsizing. However, for both flip chip bonding and TAB, a dimensional change of the pad or die requires a infrastructure update for wafer bumping and tape fabrication, respectively [5].

1.2 A Comparison between Cu wire and Au wire

Wire bonding is commonly achieved by welding a gold (Au) wire on an aluminum (Al) pad. In recent years, Cu wire has gained more market share over Au wire especially due to its lower cost. In comparison with Au, Cu has higher mechanical strength, higher electrical conductivity and thermal conductivity as shown in Table 1.1 [12]. With the same performance, Cu wire can be much thinner than Au wire, which makes Cu wire suitable for applications requiring a relatively higher I/O count.

Table 1.1 Properties of Au and Cu [12] (©2012 IEEE)

Property	Au	Cu
Thermal conductivity (W/m·K)	320	400
Electrical resistivity (Ω·m)	2.20	1.72
Young's modulus (GPa)	60	130
Yield stress (MPa)	32.70	200
Vicker's hardness (MPa)	216	369

1.3 Processing Concerns of Cu Wire Bonding

As the IC packaging industry turns to Cu wire, some processing parameters that are suitable for Au wire bonding need to be adjusted to tackle two key challenges of Cu wire bonding: Cu oxidation and hardness [13].

1.3.1 Oxidation

Unlike Au, Cu is prone to oxidation during storage and the bonding process [13]. The oxide layer leads to the formation of a crooked Cu FAB during melting [14]. When lowered down to the pad, this crooked FAB has a smaller bonding area with the pad. In addition, this oxide layer hinders the diffusion of Cu and Al and the intermetallic growth [15]. Both factors can cause a severe deterioration in the bond strength. The Cu oxidization during storage can be prevented by applying a more noble, oxidation-resistant metal coating on Cu wire surface [13]. The oxidation-resistant metal should be able to form isomorphous phase with Cu. Potential candidates include Au, Ag, Pd, and Ni [16]. Pd-coated Cu wire has been widely adopted due to its lower cost than Au, Pt and lower hardness than Ni [16]. The Cu oxidation during bonding process can be minimized by conducting bonding process in a forming gas environment consisting of 5% H_2 and 95% N_2. The hydrogen acts as a reducing agent to help reduce the oxidized Cu back to pure metal [13].

1.3.2 Hardness

The Vickers hardness of Cu is 80% higher than that of Au as shown in Table 1.1. Thus, a higher bonding force, which is estimated 20-25% higher than that for Au wire, is required [17]. The bonding force is even higher when Pd-coated Cu wire is used since Pd addition increases the Cu hardness [18]. This high force can cause Al splash and damage the dielectric layer beneath the Al pad [13]. Processing parameters, such as the EFO current, firing time, force, temperature, and ultrasonic energy, can be optimized to achieve acceptable bonding characteristics [19].

1.4 Service Reliability Concerns of Cu Wire Ball Bonds

Although significant advances have been made to ensure excellent bonding characteristics, long-term service reliability of Cu wire bonding is still a concern to the IC packaging community [20-23]. Long-term service reliability of electronic packages has become increasingly important especially in automobile industry where electronic devices need to survive harsher environment for a much longer period of time as compared with consumer electronics [24]. Obviously, it is impractical to evaluate the bond failure rate and the failure mechanism under normal usage conditions. For laboratory reliability tests, common stress conditions, such as temperature and humidity, are accelerated to shorten the testing time [23,25,26]. High temperature storage (HTS) is commonly used to evaluate the bond thermal reliability, while pressure cooker testing (PCT) and highly accelerated temperature and humidity stress testing (HAST) are used to test the bond humidity reliability [23,25-28]. Standard conditions for HTS, PCT, and HAST are summarized in Table 1.2 [23,25-28]. After a certain period of time, the bond failure rate is determined by examining the pull strength if the wire bonds are not encapsulated or the electrical resistance if the wire bonds are encapsulated [21,23].

Table 1.2. Standard testing conditions for common thermal and humidity reliability tests

Tests	Common conditions
HTS	150~250 ℃
PCT	121 ℃, 100 % relative humidity (RH)
HAST	130 ℃, 85 % RH

1.4.1 Thermal Reliability

High temperature accelerates the inter-diffusion of Cu and Al at the bonding interface [29]. Due to different diffusion rate of Cu and Al, voids can form along the ball-pad interface, known as the Kirkendall voiding [29-31]. The accelerated inter-diffusion reaction between Cu and Al promotes the growth of the initial Al-rich intermetallic: $CuAl_2$ and its transformation to a Cu-rich intermetallic: Cu_9Al_4 [31]. The associated volumetric shrinkage can cause internal stress to build up around the voiding area. The stress buildup can accelerate the crack propagation along the voids and cause the bond to fail at the ball-pad interface [30,31].

Cu wire bonding interface consistently outperforms Au wire bonding interface in the HTS tests [28]. Cu diffuses much more slowly in Al than Au due to a larger atomic misfit and a lower electronegativity between Cu and Al [32]. The intermetallic growth rate at the Cu-Al interface is much slower than that at the Au-Al interface under the same HTS testing conditions [29]. In such case, the Kirkendall voiding and the internal stress buildup are less likely to occur, which leads to the better thermal reliability of Cu wire bonds than Au wire bonds.

1.4.2 Humidity Reliability

Humidity can cause corrosion, even for the encapsulated wire bonds [20,33]. Although the encapsulation prevents direct contact between the bond surface and the moisture in the air, bond corrosion is still observed after a certain period of time [22,23]. The molding compound itself can absorb moisture [20,33]. Also, the moisture can seep through the interface between the molding compound and lead frame [20]. The moisture can diffuse to the mold-bond interface and

cause corrosion-induced deterioration of the bond joint. Humidity has been proven to be a much more destructive stress condition than temperature as results consistently show that wire bonds failed much more quickly under the HAST condition than those under the HTS condition [33]. This is especially true for Cu wire bonds. Cu wire bonds perform much worse than Au wire bonds in HAST tests where humidity is involved [28]. Humidity reliability has become one of the primary obstacles for Cu wire to dominate the market.

At the Cu-Al ball bond interface, two thin layers of Cu-Al intermetallics: Cu_9Al_4 and $CuAl_2$ are sandwiched between Cu and Al [33]. The microstructure of a failed Cu wire bond interface after the HAST test showed that Cu_9Al_4 disappeared from the bond interface, while the other major entities: Cu, $CuAl_2$, and Al remained. Galvanic corrosion can happen in the presence of moisture at the mold-bond interface [34]. The Cu-Al ball bond interface can be simplified into a Cu-Cu_9Al_4-$CuAl_2$-Al four-metal galvanic system. Due to galvanic effect, metals with higher nobility are referred to as cathodes [34,35]. Their corrosion rates are reduced. Metals with lower nobility are referred to as anodes [34,35]. Their corrosion rates are accelerated. The nobility of the metals is ranked by comparing their open circuit potentials [35]. At the Cu-Al bonding interface, the nobility ranking was given as Cu > Cu_9Al_4 > $CuAl_2$ > Al [36]. Cu_9Al_4 and Cu should act as cathodes, and their corrosion rate should be reduced, while $CuAl_2$ and Al should act as anodes and their corrosion rate should be accelerated [35]. In most cases, the cathode corrodes slower than the anode in a galvanic system [34]. Obviously, this cannot explain the disappearance of Cu_9Al_4. The cathode can corrode faster than the anode if the anode passivates strongly [34,37]. Both $CuAl_2$ and Al can passivate [38,39]. The initially dissolved Al ions from $CuAl_2$ or Al can redeposit on the corroding surface in the form of alumina. This alumina can grow into a compact, protective layer and inhibit active dissolution of Al. Thus, although being

enhanced by the galvanic effect, the corrosion rates of $CuAl_2$ and Al can still be maintained at relatively low values. On the other hand, Cu_9Al_4 might not effectively passivate due to the poor passivating capacity of cuprous oxide [37]. Although being reduced by the galvanic effect, the corrosion rate of Cu_9Al_4 might still be higher than CuA_2 and Al [37]. Therefore, Cu_9Al_4 might end up corroding faster than the other entities. Based on this hypothesis, passivation not galvanic effect has been widely considered as the dominating factor to cause Cu_9Al_4 to disappear [37]. Unfortunately, no sufficient electrochemical study has been carried out to support this theory.

1.5 Current Corrosion-mitigating Strategies

Corrosion rate of the Cu-Al ball bond interface is determined by the electrochemical nature of the involved metallic entities and the aggressiveness of the electrolyte [34]. Electrochemical nature of the entities can be modified through wire or pad metallization, while the aggressiveness of the electrolyte can be mitigated by adjusting the molding compound chemistry.

1.5.1 Wire Metallization

Wire metallization refers to as coating a noble metal on Cu wire [13]. During the bonding and the subsequent annealing process, the noble metal can be incorporated in the metallic entities at the bond interface [13,40]. The alloying of this noble metal can change the electrochemical nature of the metallic entities, such as nobility and passivation and thus might mitigate the bond corrosion rate [41]. Pd is known for its high nobility and high oxidation resistance. Pd also forms a solid solution with Cu upon melting due to the same face-centered cubic crystal structure and similar lattice constants, which are 0.389 nm for Pd and 0.361 nm for Cu, respectively [40]. These factors make Pd a suitable coating material for Cu.

Before bonding, CuPd wire is melted by an EFO current to form the FAB [2]. EFO current plays a major role in Pd distribution in the FAB [42,43]. Clauberg et al. observed that when a

low EFO current of 30mA was applied on a 20μm CuPd wire, the Pd layer was thicker at the wire neck and thinned down towards the FAB tip [43]. The Pd concentration at the FAB tip was minimal. The melting point of Pd (1555℃) is much higher than that of Cu (1085℃). With a low EFO current, the temperature was sufficient to melt Cu, however, insufficient to melt Pd. The molten Cu expanded to form the FAB while pushing the unmelted Pd layer up towards the neck region. Clauberg et al. then increased the EFO current to 60mA and observed that Pd started to diffuse into the Cu FAB. The 60mA current might not be sufficient to generate more vigorous mixing of Cu and Pd during melting. Thus Pd seemed to be randomly distributed close to the outer surface of the FAB. Lastly, they increased the EFO current up to 120mA and found that Pd and Cu were mixed more homogeneously in the FAB. Similar study conduct by Xu et al. used a 60mA EFO current on a 18μm CuPd wire [40]. They found that Pd accumulated around the wire neck and no Pd was detected at the tip of the FAB. Another study conducted by Tang et al. found that a 90mA EFO current inhibited the Pd "thinning down" or "mixing" and led to the formation of a uniform Pd layer covering the entire FAB [44]. To sum up, a low EFO current (<30mA) causes the enrichment of Pd at the wire neck region. A high EFO current (>120mA) promotes the formation of a Cu-Pd solid solution. The Pd distribution under a medium current (60~90mA) might vary between the two scenarios.

Pd distribution at the bonding interface has also been studied [24,40,45]. Pd distribution at the ball-bond interface is significantly affected by the Pd distribution in the FAB [42,43]. Xu et al. investigated the Pd distribution in the FAB and bonding interface using a 18μm Cu wire coated with 0.08μm Pd [40]. They found that if there was no Pd at the FAB tip, there was no Pd at the as-formed ball-pad interface. However, they observed that Pd gradually diffused into Cu and Cu_9Al_4 with a prolonged aging process. The diffusion rates of Pd were dramatically different

at the central region and the peripheral region. At the central region, both the Cu ball and Cu_9Al_4 contained roughly 5 at.% Pd after 168 hours of aging at 175℃. At the peripheral region, Cu ball contained 12 at.% Pd and a thin layer of Cu_9Al_4 adjacent to the Cu ball enriched with 42 at.% Pd under the same aging conditions. At both regions, Pd was not able to penetrate into $CuAl_2$ and Al. T. Uno analyzed the Pd distribution across the bond interface after 400 hours of the PCT aging using a 25μm Cu wire coated with 0.2μm Pd [22]. He found that Pd promoted the formation of Cu_3Al_2 and CuAl, different from the original Cu_9Al_4 and $CuAl_2$ found in a Cu bonding interface. Pd diffused into the Cu ball and Cu_3Al_2 layer, however, not into the CuAl and Al layers. The Cu-Pd layer contained 3-5 at.% Pd and the $(Cu\text{-}Pd)_3Al_2$ layer contained 2-3 at.% Pd. Lin et al. studied the Pd diffusion in the IMC layers using a 20μm Cu wire coated with 0.1μm Pd [45]. They identified that the Pd-containing IMC as $(Cu\text{-}Pd)_9Al_4$ mixed with a small amount of $(Cu\text{-}Pd)_3Al_2$. The Pd-containing IMC layer contained 1.64-2.07 at.% Pd overall. Like many other studies, they also found that Pd was not able to penetrate into $CuAl_2$ and Al. To sum up, Pd can diffuse into the Cu and the Cu-rich IMC: Cu_9Al_4 or Cu_3Al_2, however, not into the Al-rich IMC: $CuAl_2$ or CuAl and Al. The Pd concentration in Cu and the Cu-rich IMC layer depends on the Pd distribution in the FAB, aging condition and time, and the region at the bond area.

CuPd wire bonds consistently showed better performance than Cu wire bonds in humidity reliability tests [21,22]. T. Uno compared the lifetime of bare Cu and CuPd wire bond in PCT tests [22]. The average lifetime of the CuPd wire bond (>800 hours) was at least two times higher than that of the Cu wire bond (<250 hours). CuPd wire bonds performed even better in the uHAST tests. The average lifetime of the CuPd wire bond (>1300 hours) was more than ten times higher than that of the Cu wire bond (<100 hours). This results showed a much higher corrosion resistance of the CuPd wire bond than a Cu wire bond. Additionally, Kim et al.

emphasized that the CuPd wire bond exhibited a reliability advantage when Pd enriched on the ball surface instead of diffusing into the ball [21]. Until now, the mitigating mechanism of Pd is not clear. Some authors have attributed the better performance of CuPd wire bonds to the higher corrosion resistance of the Pd-enriched layers [22, 40]. However, no mechanistic reason has been provided to explain that further.

1.5.2 Pad Metallization

Pad metallization refers to as applying one or multiple layers of noble metal finish, such as Ni, Pd, Au, to the Al pad [46]. These noble metal layers act as a barrier to prevent the inter-diffusion between Cu and Al and the formation of Cu-Al IMCs [45,47]. Since these Cu-Al IMCs were preferentially attacked by the humidity, eliminating them can effectively improve the bond humidity reliability. Liu et al. compared the performance of Cu wire bonds on a bare Al pad and an Al/Ni/Pd pad in the HAST tests [48]. The Ni and Pd layers of the Al/Ni/Pd pad were 5μm and 0.2μm, respectively. Through the bond pull test, they found that the bond force of the wire bonds on the bare Al pad decreased much faster than that on the Al/Ni/Pd pad during the HAST test. This indicated a better corrosion resistance of the Cu-Al/Ni/Pd ball-bond interface. Kawashiro et al. compared the performance of Cu wire bonds on an Al pad, Al/Pd pad, and Al/Ti/Pd pad in both HTS and HAST tests [49]. Both the Pd and Ti layers were 0.175 μm thick. The cumulative failure lifetimes of the Cu wire bonds on the Al/Ti/Pd and the Al/Pd pads were significantly higher than that on the bare Al pad in both tests. In both studies, the authors attributed the improved humidity reliability to a more noble electrochemical nature of the bonding interface. The bonding interface consisted of Cu-Pd solid solution instead of Cu-Al IMCs. The higher nobility of Cu-Pd solid solution should contribute to the better humidity reliability of the Cu wire bonds.

1.5.3 Molding Compound Chemistry

The bond failure rate has been found to be sensitive to the molding compound chemistry, which is determined by the chemical nature of the encapsulation materials [23,33]. Epoxy-based molding compound has been extensively used [50]. Various raw material ingredients need to be added in the epoxy resins to meet the required physical and chemical molding properties. Typical ingredients are hardener, inorganic filler, coupling agents, release agents, curing catalysts, and flame retardants [50]. Among these chemical species, chloride ions from resin synthesis and bromide, antimony ions from the flame retardants are primary corrosive species [50]. Due to the environmental concerns, bromide and antimony contents have been minimized. [22]. However, chloride contamination from the resin synthesis is much more difficult to avoid [22]. Chloride ion can still be found in many commercialized molding compounds. Chloride has been known to induce pitting corrosion of Al because it can aggressively attack its passive film [51]. Chloride can also accelerate the Cu dissolution since it can react with Cu to form CuCl [52].

Numerous studies showed that reducing the chloride concentration in the molding compound improved the bond performance in the humidity reliability tests [23,53,54]. Gan et al. observed that almost 60% of the wire bonds encapsulated in a conventional molding compound (>20ppm chloride) failed while no wire bonds encapsulated in a green molding compound (<20ppm chloride) failed after 96 hours of the unbiased-HAST tests [53]. Su et al. studied failure rates of CuPd wire bonds encapsulated in formulated epoxy molding compounds with different chloride concentrations [23]. The number of failed bonds after 360 hours of the biased-HAST test decreased by 75% as the chloride concentration in the molding compound was lowered from 100ppm to 25ppm. Chiu et al. studied failure rates of Cu wire bonds encapsulated in molding compounds with three different chloride concentrations: 24ppm, 7.6ppm, and 4.3ppm under the

biased HAST test [54]. For the bonds encapsulated in the molding compound containing 24ppm chloride, all of them failed after 192 hours. For the bonds encapsulated in the molding compound containing only 4.3ppm chloride, none of them failed after 1344 hours.

Besides chloride concentration, pH is another important factor since the surface passivation of Cu and Cu-Al IMCs is not stable in a highly acidic environment [55]. Su et al. found that the number of failed wire bonds decreased by 40% when the pH value of the molding compound decreased from 6.5 to 4.5 [23]. In summary, reducing chloride concentration and acidity of molding compounds are effective in improving the bond reliability.

1.5.4 IMC Coverage

Improving the IMC coverage has been found to improve the bond performance in humidity reliability tests [48,56,57]. Liu et al. found that a higher IMC coverage led to a lower bond failure ratio in the unbiased-HAST test [48]. Yap et al. observed that almost half of the wire bonds with less than 60% IMC coverage at the bonding area failed after 96 hours of the biased (5.5V)-HAST test, while no wire bond with more than 60% IMC coverage at the bonding area failed at all in the same test [56]. Goh et al. conducted a comparison study on the corrosion behavior of unencapsulated Cu and Au wire bonds soaked in a 500ppm NaCl solution [57]. All the Cu wire bonds failed after 25 minutes, while less than 10% Au wire bonds failed after 30 minutes. The Au-Al bonding interface showed higher resistance to galvanic corrosion attack than the Cu-Al bonding interface despite a much larger electromotive force, which is 3.2V for Au-Al as compared with 2V for Cu-Al. The author attributed this phenomenon to the larger IMC coverage of the Au-Al bonding interface than that of the Cu-Al bonding interface. With a larger IMC coverage, Cl^- ions were not able to seep in easily between the Au ball and the Al pad to set up a galvanic corrosion cell. Lee et al. conducted the ball shear tests on Au and Cu wire bonds

after the PCT test [58]. All the Cu wire bonds failed at the ball-bond interface while only 20% Au wire bonds failed at the ball-bond interface after 48 hours. These results indicate that the interfacial corrosion has a larger impact on the Cu wire bonds than the Au wire bonds. The authors attributed the lower corrosion resistance of the Cu wire bonds to the poor Cu-Al IMC coverage. They specified that the IMC coverage of a Cu-Al bonding interface was less than 50% after thermal aging for 300 h at 175℃, while the IMC coverage of an Au-Al bonding interface was higher than 70% under the same aging conditions.

1.6 Problem Statements and Research Strategies

In recent years, studies on humidity reliability of Cu wire bonds have been focusing on the standard stress acceleration tests, predominantly PCT and HAST and the subsequent chemical and microstructural inspections [23, 25-28]. A key finding that Cu_9Al_4 is preferentially attacked has not been fully understood due to a lack of understanding of the bond corrosion mechanism. As a result, the mitigating mechanisms of various strategies introduced above are not clear. This hinders optimizing the current strategies and developing more effective and economical solutions in the future. Thus, electrochemical characterizations are necessary to provide a fundamental understanding on these issues. Due to the size limitation, it is difficult to directly evaluate the electrochemical characteristics of the involved metallic entities using a ball-bonded joint. Bulk samples of these metallic entities can be used instead. Liam et al. studied the electrochemical behavior of Cu, Al and Cu-Al IMCs as influenced by Pd addition in a 25ppm NaCl solution of pH 6 [36]. However, the corrosion mechanism that leads to the disappearance of Cu_9Al_4 and the mitigating mechanism of Pd addition were not addressed. In addition, the synergic effect of Pd addition and various usage conditions were not studied.

In this study, ingots of metallic entities involved in the Cu wire bonding interface including Cu, Cu_9Al_4, $CuAl_2$, and Al were prepared. Pd-doped Cu and Cu-Al IMCs were also synthesized. Electrochemical studies on these undoped and Pd-doped metallic entities were carried out in electrolytes with various chloride concentrations and pH values to understand the synergic effect of Pd and molding compound chemistry on their corrosion behavior. Results of these studies are summarized in chapter 3.

The electrochemical behavior of the metallic entities is compared to propose a corrosion mechanism of the Cu(Pd)-Al ball bond interface in chapter 4. The proposed mechanism is used to explain the disappearance of Cu_9Al_4 observed in numerous humidity reliability tests.

Once the corrosion behavior of the ball bond interface has been introduced, the mitigating mechanisms of using CuPd wire and green molding compound are investigated in chapter 5.

CHAPTER 2 SAMPLE PREPARATION, EXPERIMENTAL TECHNIQUES, AND DATA ANALYSIS

Sample preparation, especially the synthesis of Cu(Pd)-Al IMCs, and electrolyte preparation are introduced first. Details of electrochemical and non-electrochemical experimental techniques applied in this study including the potentiodynamic polarization measurement, zero resistance ammetry, and the mass loss experiment are introduced later. The associated data analysis and interpretation are also presented.

2.1 Sample Preparation

The major metallic entities involved in the Cu-Al bond interface are Cu, Cu_9Al_4, $CuAl_2$, and Al [31]. The ingots of these four entities were prepared individually. When a CuPd wire is used, Pd can diffuse into these entities to various degrees upon melting and during the annealing process [13,40,42,43]. Based on the Cu-Pd phase diagram, Pd can easily form a solid solution with Cu during the FAB formation. Thus, Cu-Pd alloys were prepared. Pd has also been found to diffuse into the IMC phases during the subsequent annealing process [22,40,45]. Pd-doped Cu_9Al_4 and Pd-doped $CuAl_2$ were also prepared. During the bonding process, the CuPd wire is melted before being bonded to the Al pad [2]. Therefore, to emulate the real bonding process, Cu-Pd alloys were prepared first and subsequently melted with the appropriated amounts of Al to form the Pd-doped Cu_9Al_4 and Pd-doped $CuAl_2$.

With a 20μm wire diameter, the Pd concentration in the prepared Cu-Pd alloy is determined by the coating thickness and the EFO conditions such as the applied current and its duration [40,43,44]. In this study, the Pd coating is assumed to be 0.08 μm thick. If the EFO current and its duration are sufficient, Pd can be considered homogenously distributed in the FAB [44]. The Cu-Pd alloy should contain 2 wt.% Pd. Therefore, a 2 wt.% Cu-Pd alloy was prepared. If a lower

EFO current or a shorter duration is applied, Pd concentration is higher on the outer surface of the FAB as Pd has a higher melting temperature than Cu [43]. In this case, a 9 wt.% Cu-Pd alloy was prepared. The 2 wt.% and 9 wt.% Cu-Pd alloys are denoted as Cu-2Pd and Cu-9Pd, respectively. The as-prepared Cu-2Pd and Cu-9Pd were melted with the appropriate amounts of Al to prepare the Pd-doped Cu_9Al_4 and $CuAl_2$. For simplicity, the Cu_9Al_4 and $CuAl_2$ IMCs were referred to as γ and θ in general. The Cu_9A_4 and $CuAl_2$ IMC made with pure Cu were referred to as γ #1 and θ #1, respectively. The Cu_9A_4 and $CuAl_2$ IMC made with Cu-2Pd were referred to as γ #2 and θ #2, respectively. The Cu_9A_4 and $CuAl_2$ IMC made with Cu-9Pd were referred to as γ #3 and θ #3, respectively.

All samples were prepared through the arc-melting process using the as-received Cu, Pd, and Al of 99.99% purity from the Kurt J. Lesker Company. The arc-melting process was carried out in a model 5SA single arc furnace from Centorr Vacuum Industries, Inc.. Before melting, the furnace was purged with a mechanical pump for at least 5 minutes and then backfilled with argon until the pressure went back to the atmospheric pressure. This purge-backfill cycle was repeated at least three times. Then, a constant argon flow was maintained. A direct current was set at 80 amperes. The tungsten electrode was positioned right above the charge, and an arc between the tungsten electrode and the copper crucible melted the charge instantaneously. For the Cu_9Al_4 and $CuAl_2$ IMC preparation, the Cu or Cu-Pd alloys were placed on top of the Al. When the arc was generated, it struck and melted the Cu or Cu-Pd alloys first. The molten Cu or Cu-Pd alloys melted the Al subsequently and formed the IMCs. This setup was proven to reduce the aluminum evaporation and oxidation significantly. After the first melting, the ingots were turned over and melted again. This procedure was repeated at least three times to ensure the

homogeneity of all samples. The total weight loss for all samples used was about 0.2wt.% to 0.3wt.%. The weight fractions of Cu, Pd, and Al of all the samples are tabulated in Table 2.1.

Table 2.1 Nominal composition of the samples used

Sample	Cu (wt.%)	Pd (wt.%)	Al (wt.%)
Cu	100	0	0
Cu-2Pd	98.0	2.0	0
Cu-9Pd	91.0	9.0	0
γ #1: Cu_9Al_4	84.1	0	15.9
γ #2: $(Cu\text{-}2Pd)_9Al_4$	82.5	1.7	15.8
γ #3: $(Cu\text{-}9Pd)_9Al_4$	77.0	7.6	15.4
θ #1: $CuAl_2$	54.1	0	45.9
θ #2: $(Cu\text{-}2Pd)Al_2$	53.2	1.1	45.7
θ #3: $(Cu\text{-}9Pd)Al_2$	50.0	5.0	45.0

2.2 XRD Analysis on (Pd-doped) IMCs

The as-prepared IMCs were ground into fine powder using a set of quartz mortar and pestle. Crystal structures of these IMC powders were examined by powder X-ray diffraction with a Rigaku Miniflex II™ benchtop X-ray diffractometer. The diffraction patterns obtained were analyzed using a Jade® software package.

2.3 Electrochemical Characterization

Open circuit potential measurements, anodic and cathodic polarization measurements, and zero resistance ammetry measurements were used in this study. Open circuit potential and polarization measurements are used to characterize the self-corrosion behavior of a metallic entity, while the zero resistance ammetry measurement is used to evaluate the galvanic effect between two dissimilar metallic entities when they are electrically connected [34,59].

2.3.1 Working Electrode Preparation

The working electrode (WE) was prepared by encapsulating the sample ingot to be studied in an epoxy-based molding compound. Before the encapsulation, a metal (Cu) wire was soldered to the top surface of the ingot. Part of the Cu wire remained unencapsulated to connect with the WE

lead from the potentiostat. After the encapsulation, the unsoldered bottom was ground to expose the sample surface. The surface was polished using a series of SiC paper up to 2400 grit. Then. the polished surface was degreased by ultrasonic cleaning in soapy water followed by a thorough wash in deionized (DI) water. The prepared WE surface was dried in air and the area of the exposed surface was measured before every test. The measured surface area varied between 0.1 cm^2 and 0.2 cm^2. A schematic of the working electrode (WE) prepared by the above method is provided in Fig. 2.1.

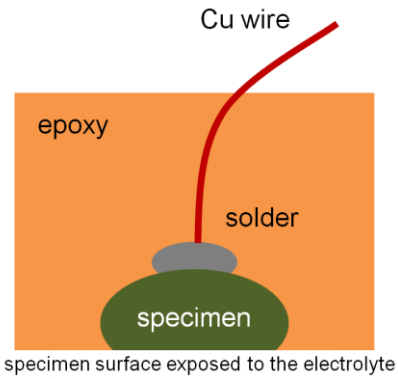

Figure 2.1 Working electrode with a known exposed surface area (color online). The sample was first soldered to a Cu wire for electrical connection and then encapsulated in an epoxy resin. A portion of specimen surface was exposed by the standard metallographic preparation.

2.3.2 Electrolyte Preparation

Chloride is the primary corrosive species in the molding compound [23]. Sodium chloride (NaCl) solutions were prepared by dissolving the appropriated amount of NaCl in DI water (≈18MΩ·cm) obtained from Barnstead Nanopure™. The water extract of commercialized epoxy-based molding compounds has a conductivity equivalent to a pH 6, 20ppm NaCl solution. Therefore, a 20ppm NaCl solution of pH 6 was prepared first. In addition, two other NaCl concentrations: 100ppm and 1ppm and two other pH values: 4 and 9 were used. The acidic electrolyte was prepared by adding dilute sulfuric acid (H_2SO_4) solution. The alkaline electrolyte

was prepared by adding dilute sodium hydroxide (NaOH) solution. The temperature was also varied for the measurements conducted in a pH 6, 20ppm NaCl solution. Besides the room temperature (25℃), two higher temperatures: 45℃ and 65℃ were used. A model 282 water bath from the Precision Scientific was used to maintain the temperature of the testing cell. All measurements at higher temperatures were started after the testing cell temperature was stabilized at the set value.

2.3.3 Open Circuit Potential Measurement

A VSP model potentiostat from BioLogic Science Instruments was used to carry out all the electrochemical measurements. Open circuit potential (E_{oc}) is the potential difference between the WE and the RE. It indicates the nobility of a metal [60]. A metal with a higher value of E_{oc} is less likely to corrode [60]. A two-electrode configuration was used for the E_{oc} measurement as shown in Fig. 2.2. The Ag/AgCl (saturated with KCl) was used as the reference electrode (RE). To obtain a stabilized value of E_{oc}, the WE was immersed in the electrolyte for an extended period of time. The length of the immersion varied depending on the type of the WE [60]. A passivating metal, such as Al, requires a longer time for its E_{oc} value to stabilize as compared with a non-passivating metal like Cu. The E_{oc} measurement is sensitive to the surface condition of the sample [60]. A long immersion time for a passivating metal is due to the slow passivation process on its surface [61]. For instance, when the Al sample is immersed in a 1ppm NaCl electrolyte, the $E_{oc,Al}$ value fluctuates as the Al surface is being passivated. The passivation process is extremely slow due to a low Al dissolution rate in a 1ppm NaCl solution. The E_{oc} value will not stabilize until a mature passive film forms on the Al surface. In this study, the immersion time was 2 hours for Cu and Cu-Pd alloys, 48 hours for γ and θ IMCs, and 72 hours for pure Al. This held true for all the electrolytes since the salt concentrations used were all very

low. After the immersion, E_{oc} was monitored for at least one additional hour, and the stabilized E_{oc} values were reported.

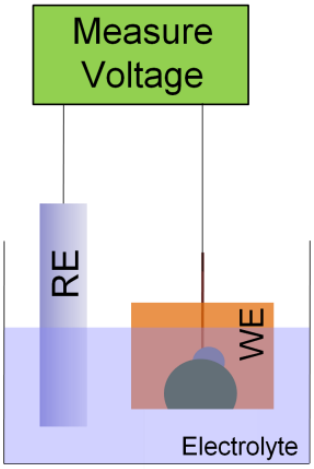

Figure 2.2 Two-electrode setup for the open circuit potential measurement.

2.3.4 Potentiodynamic Polarization Measurement

Potentiodynamic polarization measurements were carried out after a stable E_{oc} was obtained as suggested in the ASTM G5-14 Standard [62]. A three-electrode configuration was used as shown in Fig. 2.3. A Platinum foil was used as the counter electrode (CE). The potentiostat measures the potential between the RE and the WE, denoted as $E_{measured}$, while applying a current between the CE and the WE, denoted as I.

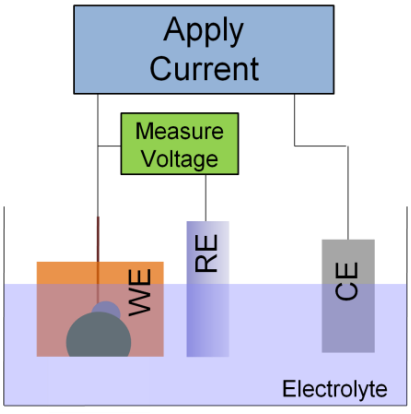

Figure 2.3 Three-electrode configuration for the potentiodynamic polarization measurements.

The $E_{measured}$ is the sum of the applied potential on the WE, E_{WE}, and the ohmic potential drop between the WE and the RE due to the electrolyte resistance, IR_{soln}, as shown in equation (1) [63]:

$$E_{WE} = E_{measured} - IR_{soln} \qquad (1)$$

The distance between the RE and the WE was minimized. However, the electrolytes used in this study have low salt concentrations and therefore high resistivity. Therefore, the R_{soln} value needs to be measured to obtain the accurate E_{WE} values. The current interrupt technique was used to determine the R_{soln} values [64]. A pulse of 5μA current was applied between the WE and the CE and last for about 0.04 second. An instantaneous potential increase (ΔE) after the current was turned on and an equal value of instantaneous potential decrease (ΔE') after the current was turned off were observed as illustrated in the schematic in Fig 2.4. The R_{soln} value can be obtained by dividing either ΔE or ΔE' with the applied current, 5μA. The current value needed to be small enough to not cause a large perturbation to the WE. Also, the current value needed to be high enough to obtain well-defined instantaneous potential changes. A total of ten current pulses were applied. The associated ten ΔE and then ΔE' values were all used to obtain an average R_{soln} value.

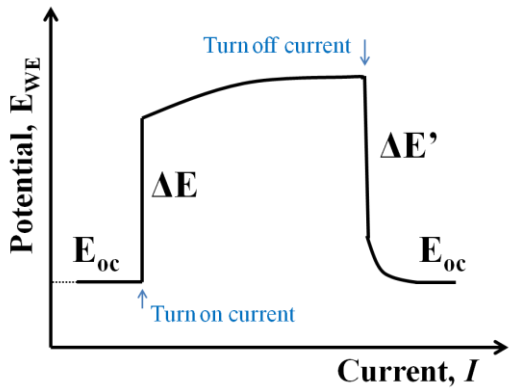

Figure 2.4 The instantaneous potential increase, *ΔE*, and decrease, *ΔE'* in one current pulse in the current interrupt method. Either *ΔE* and *ΔE'* can be divided by the applied current, 5μA to obtain the R_{soln} value.

Two types of potentiodynamic polarization were applied: anodic polarization and cathodic polarization, in which the applied potential was below and above E_{oc}, respectively. Two different ways of polarization, which can be conveniently referred to as the one-way potential sweep and two-way potential sweep, were practiced. For the one-way potential sweep, the potential of the WE was immediately polarized to the lower limit of the cathodic polarization and then linearly increased all the way to the upper limit of the anodic polarization. In such case, both the cathodic and anodic polarization curves were obtained in one sweep. For the two-way potential sweep, the potential of the WE was linearly polarized down to the lower limit of the cathodic polarization from its E_{oc} to obtain the cathodic polarization curve first. Then, the WE rested under the open circuit condition for an extended period of time. After the E_{oc} of the WE was stabilized again, the potential of the WE was linearly increased to the upper limit of the anodic polarization from its E_{oc} to obtain the anodic polarization curve. Therefore the cathodic and anodic polarization curves were obtained in two separate sweeps.

In this study, the two-way sweep is preferred over e one-way sweep. At the same scan rate, the cathodic polarization curve measured using the two-way sweep is closer to the equilibrium condition than that measured using the one-way sweep. In the two-way sweep, the cathodic polarization imposed on the WE increased gradually. This provided more time for the cathodic reactions to reach equilibrium. In the one-way sweep, a large cathodic polarization was immediately imposed on the WE. There was not enough time for the cathodic reactions to equilibrate. Additionally, the high cathodic polarization caused the cathodic reaction rate to increase dramatically in a short period of time. This changed the pH, conductivity, and composition of the electrolyte layer adjacent to the WE surface [65]. This change in the electrolyte then affected the measurement of the cathodic current density in return [65,66]. As a

result of both factors, the cathodic polarization curve obtained in the one-way sweep showed poor reproducibility and cause a large difference between E_{oc} and corrosion potential, E_{corr}. For instance, the cathodic polarization curves of Cu obtained from the one-way sweep and the two-way sweep in a pH 6, 20ppm NaCl electrolyte are shown together in Fig. 2.5a. Similarly, the anodic polarization curves of Cu obtained from both methods are shown in Fig 2.5b. The polarization curves were plotted using the logarithm of the current density as the *x*-axis and E_{WE} as the *y*-axis. Results of five repeated runs from the one-way sweep and the two-way sweep were plotted for comparison. Both the cathodic and the cathodic polarization curves obtained from the two-way sweep showed a better reproducibility. More importantly, the E_{corr} value obtained from the one-way sweep was much more positive than the E_{oc} value. The high E_{corr} value "buried" a significant portion of the anodic polarization curve as seen in Fig. 2.5b and resulted in the disappearance of the linear regime, which is critical for obtaining the corrosion current density i_{corr}.

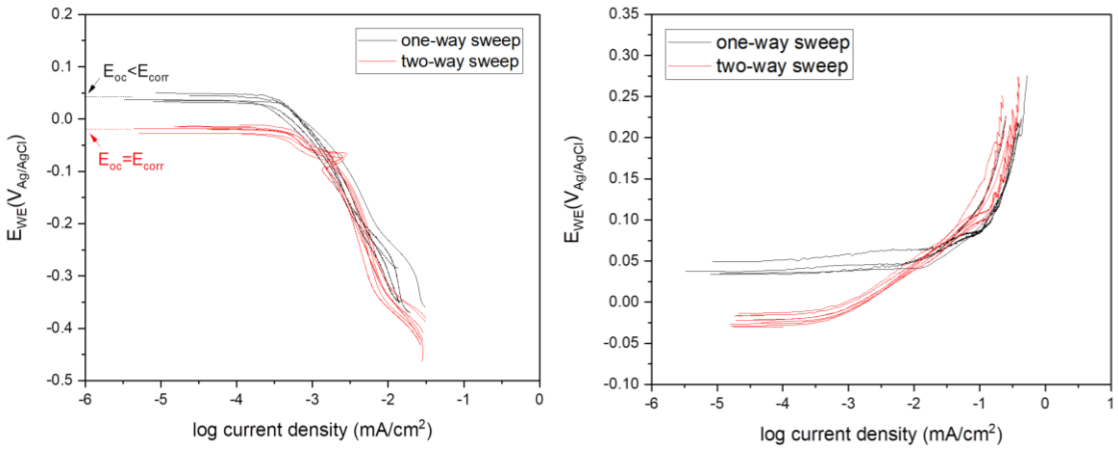

(a)(b)

Figure 2.5 (a) cathodic polarization curves of Cu obtained from one-way sweep (black) and two-way sweep (red); (b) anodic polarization curves of Cu obtained from one-way sweep (black) and two-way sweep (red). The electrolyte was 20 ppm NaCl with a pH level of 6.

In addition, the two-way sweep can achieve more accurate IR_{soln} compensation than the one-way sweep. The electrolytes used in this study were dilute solutions of NaCl, the R_{soln} value was very high initially and reduced rapidly during the potential sweep. Overcompensation might happen if this drop in the R_{soln} value is not considered. To avoid this issue, the R_{soln} value used in equation (1) should be measured after the polarization measurement is finished. If the cathodic polarization and the anodic polarization measurements can be split up like the case in the two-way sweep, the R_{soln} can be measured right after the cathodic sweep and used to correct the applied potential without overcompensation. Therefore, the two-way sweep was also preferred due to a more accurate R_{soln} correction.

The overall procedures for the two-way sweep are described as follows. The WE rested under open circuit condition and its E_{oc} was monitored for an hour. Then, the potential of the WE was swept down to 500 mV below E_{oc} at a scan rate of 20 mV/min. The scan rate being too slow is not recommended since the surface condition might change and the E_{oc} might drift during the long duration of the test [62,67]. The scan rate being too fast is also not recommended since the charging current to the electrode-electrolyte capacitance might account for a significant portion of the measured current [62,67]. Right after the cathodic sweep was finished, the solution resistance, denoted as $R_{soln,1}$, was measured using the current interrupt method. Afterwards, the WE rested under the open circuit condition until the E_{oc} was stabilized again. The potential of the WE was then swept up to 600 mV above E_{oc} at the same scan rate of 20 mV/min. The solution resistance, referred to as $R_{soln,2}$, was measured once the anodic potential sweep was complete. For the cathodic branch, the $R_{soln,1}$ value was used to obtain the E_{WE} value, while for the anodic branch, the $R_{soln,2}$ value was used to obtain the E_{WE} value. The current density was obtained by dividing the measured I by the surface area of the WE. The polarization curves were plotted

using the logarithm of the current density as the *x*-axis and E_{WE} as the *y*-axis. This semi-logarithm plot is more suitable to include a wider range of the current density data [68]. Furthermore, it is more convenient to carry out the Tafel extrapolation to obtain the i_{corr}.

The i_{corr} values were obtained through Tafel extrapolation on the linear regimes of either the anodic or cathodic polarization curves [68]. In this study, anodic Tafel extrapolation was preferred over cathodic Tafel extrapolation. Cathodic reactions are more sensitive to the surface condition of the WE [69]. Corrosion product can cover the WE surface during the immersion period and change its cathodic activity [69]. The dominant cathodic reaction, oxygen reduction reaction (ORR) often suffers from diffusion limitation of oxygen in the electrolyte during the cathodic polarization [52]. The diffusion limitation might distort the cathodic polarization curve and the i_{corr} value obtained from the cathodic extrapolation can be overestimated. Additionally, other cathodic reactions such as the hydrogen evolution reaction (HER) and the reduction of the corrosion product can happen [52,65,66]. These reactions might disrupt the linear regime of the cathodic polarization curve and make the Tafel extrapolation impossible. Hence, the i_{corr} values were obtained primarily from the anodic polarization curves.

2.3.5 Zero Resistance Ammetry

The same potentiostat was used to measure the galvanic currents between Cu and γ, γ and θ, θ and Al using the embedded zero resistance ammetry (ZRA) technique [70]. The ZRA technique measures the galvanic current between two dissimilar metals: metal #1 and metal #2 when they are connected to the CE lead and WE lead, respectively as shown in Fig. 2.6. For the Cu-γ couple, Cu was connected to the CE as metal #1 and γ was connected to the WE as metal #2. For the γ-θ couple, γ was connected to the CE as metal #1 and θ was connected to the WE as metal #2. For the θ-Al couple, θ was connected to the CE as metal #1 and Al was connected to

the WE as metal #2. Both metals had the same area of around 0.15 cm^2. The galvanic current was measured immediately after the two metals were immersed in the electrolyte. Three electrolytes of 100ppm, 20ppm, and 1ppm NaCl solution with a pH level of 6 were used. The measurement last for 12 hours. The measured current was then divided by the average area of metal #1 and metal #2 to provide the galvanic current density, denoted as i_g(metal #1:metal #2). A positive value of i_g(metal #1:metal #2) indicates metal #1 is the cathode and metal #2 is the anode. For the Pd-doped galvanic couples, Pd was assumed to be equally dissolved into Cu and γ. Therefore, i_g(Cu-2Pd:γ #2) and i_g(Cu-9Pd:γ #3) were measured.

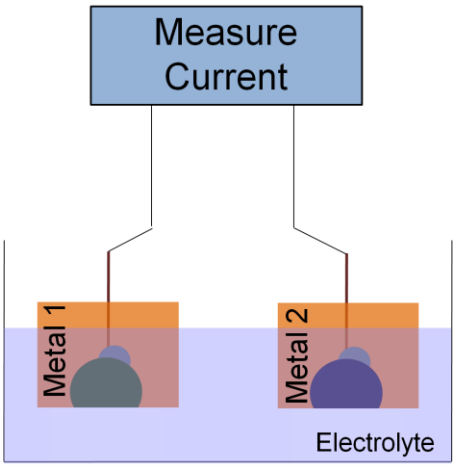

Figure 2.6 Experimental setup for the ZRA measurement

2.4 Mass Loss Experiment

To emulate the bond interface, the as-prepared Cu, γ, θ, and Al ingots of similar mass were brought into contact, as shown in Fig. 2.7. The average starting mass of the Cu, γ, θ, and Al ingots were 540 mg, 370 mg, 280 mg, and 210 mg, respectively. For better contact, the ingot was polished to create flat and smooth surfaces on both sides. After polishing, the ingot was cleaned in soapy water and ultrasonically rinsed in DI water. The cleaned ingot was dried in air and weighed. Afterward, the four ingots were brought to contact using two plastic sheet holders. To

avoid sliding, a dip was made in the center of each holder in such that the end Cu or Al ingot can sit in. The γ and θ ingots were inserted between the Cu and Al ingots. A pressure was applied to the four-ingot joint by tightening up the screws inserted in both ends of the holders. The four ingots in contact were then fully immersed in a 20 ppm NaCl solution with a pH level of 6. After two weeks, the ingots were ultrasonically cleaned individually in DI water until no corrosion products were visible on its surface. The clean ingots were dried and weighed. Mass loss experiments on three two-metal couples: Cu-γ, γ-θ, and θ-Al, were also carried out using the same procedure.

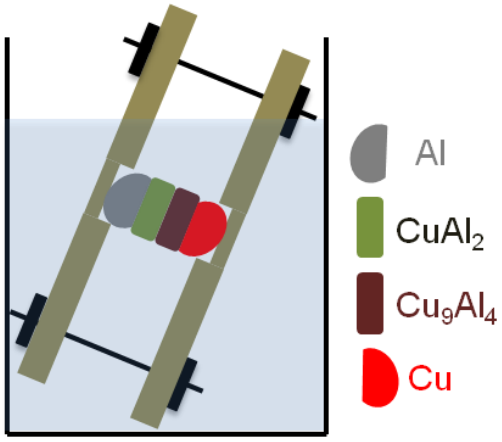

Figure 2.7 Four-metal mass loss experimental setup. The electrolyte used was 20ppm NaCl solution of pH 6.

CHAPTER 3 ELECTROCHEMICAL STUDIES OF THE METALLIC ENTITIES AT THE BALL-BOND INTERFACE

3.1 Introduction

Four metallic entities, Cu, γ, θ, and Al, are involved at the Cu-Al ball bond interface [31]. Electrochemical corrosion behavior, such as the cathodic and anodic reaction kinetics, E_{oc}, and i_{corr}, of these four entities were characterized first.

The bond interface formed with Pd-coated wire has shown an improved time-to-failure in high accelerated stress tests [21,22]. This improved time-to-failure has been attributed to a higher Pd concentration at the outer surface of the FAB formed during the arc-melting process [21]. Therefore, Pd effect on the electrochemical behavior of the affected metallic entities needs to be characterized.

Additionally, temperature and molding compound chemistry are critical factors that affect the bonding failure mechanism and failure rate [23]. The chloride concentration and pH of the electrolyte and the temperature of the testing cell were also varied. The following electrolyte and environmental conditions were studied: 100ppm, 20ppm and 1ppm NaCl, pH 6, 25℃; pH 9, pH 6, and pH 4, 20ppm NaCl, 25℃; 65℃, 45℃, and 25℃, pH 6, 20ppm NaCl.

3.2 Results and Discussion

3.2.1 XRD Pattern Analysis

XRD spectra of γ #1, γ #2, and γ #3 are provided in Fig. 3.1a. The diffraction peaks of the as-prepared γ #1 matched the known standard. The Pd addition didn't affect the diffraction spectrum. This suggests that Pd was fully incorporated into Cu and formed homogenous $(Cu_{1-x}Pd_x)_9Al_4$. In addition, all peaks of γ #2 and γ #3 showed a systematic shift to a lower angle as the atomic size of Pd is known to be slightly larger than Cu.

XRD spectra of θ #1, θ #2 and θ #3 IMCs are provided in Fig. 3.2b. In the close-up box at the top right of this figure, a small peak associated with the γ phase was observed for all three samples. It was known that as-synthesized $CuAl_2$ could contain a small amount of Cu_9Al_4 [61]. It was also observed that the peak height ratio of γ to θ increased as the amount of Pd addition increased, indicating that Pd preferred to be in the γ phase. Such preferred Pd segregation in γ IMCs has been widely observed at the CuPd wire bonding interface [22,40,44].

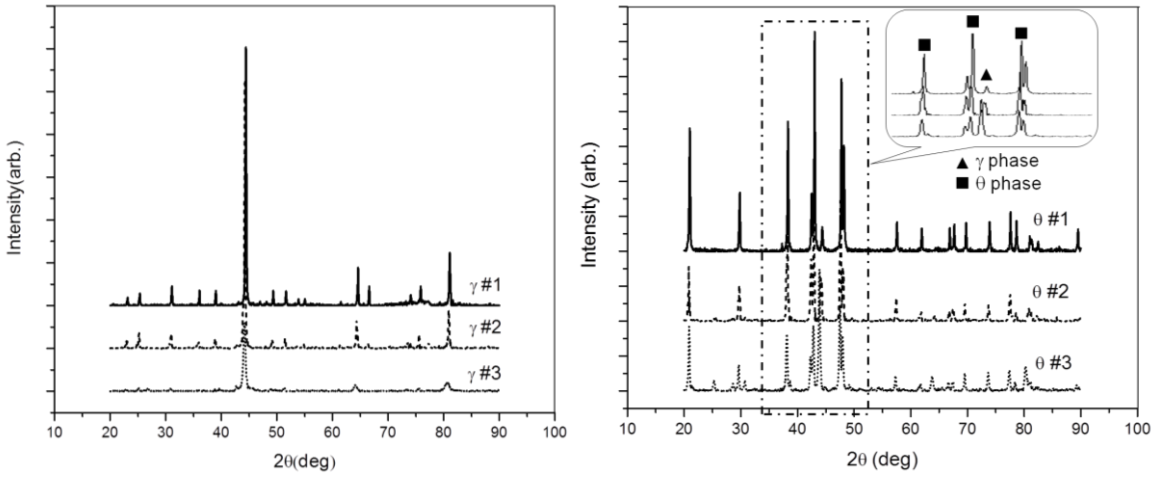

(a) (b)

Figure 3.1 XRD spectra of powdered (a) γ IMCs and (b) θ IMCs; the powder was made from the as-produced samples via arc melting. γ #1 and θ #1 were made with pure Cu. γ #2 and θ #2 were made with Cu-2Pd alloy. γ #3 and θ #3 were made with Cu-9Pd alloy. Orientation effect was observed for γ #3 because its high ductility made powder preparation more difficult.

3.2.2 Corrosion Behavior of Cu, γ, θ, and Al

The cathodic polarization curves of Cu, γ, θ, and Al are shown in Fig. 3.2. For the cathodic reactions, two possible reactions are oxygen reduction reaction (ORR) and hydrogen reduction reaction (HER) as shown in reaction (1) and (2).

$$O_2 + 2H_2O + 4e^- \rightarrow 4OH^- \qquad (1)$$

$$2H^+ + 2e^- \rightarrow H_2 \qquad (2)$$

ORR is the dominant cathodic reaction on Cu and γ surface, while both ORR and HER are involved on θ and Al surface [52,72,73]. The cathodic reaction currents of Cu and γ were much higher than those of θ and Al at a given applied potential. This should be due to the higher catalytic activity of Cu than Al [74].

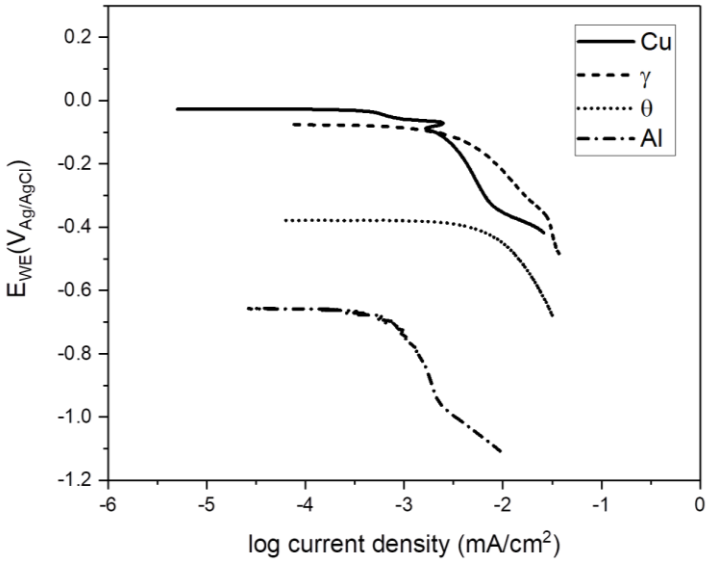

Figure 3.2 Cathodic polarization curves of Cu, γ, θ, and Al. All the polarization curves were measured in a 20 ppm NaCl electrolyte with a nearly neutral pH.

The anodic polarization curve of Cu is shown in Fig. 3.3a. A well-defined linear regime is observed as the applied potential increases. The slope of this linear regime is referred to as the anodic Tafel slope and is estimated to be 60 mV per decade of current. This anodic Tafel slope is consistent with the value provided by G. Kear et al. in their review on electrochemical corrosion of Cu in chloride media [52]. This result indicates the anodic dissolution rate of Cu was under the mixed control of the charge transfer in reaction (1) and the mass transfer of $CuCl_2^-$ in reaction (2), as pointed out in [52].

$$Cu + Cl^- \leftrightarrow CuCl_{ads} + e^- \qquad (1)$$

$$CuCl_{ads} + Cl^- \leftrightarrow CuCl_2^- \qquad (2)$$

where the subscript "ads" refers to as adsorbed on the Cu surface. As the applied potential further increases, the anodic current density becomes less dependent on the applied potential. G. Kear et al. attributed this behavior to the diffusion control of $CuCl_2^-$ from the electrode surface to the bulk electrolyte [52].

Anodic polarization curve of Al shown in Fig. 3.3a also exhibits a well-defined linear regime. The anodic Tafel slope is measured to be 292 mV per decade of current, which is significantly higher than the anodic Tafel slope of Cu. This high value of anodic Tafel slope is also shown in [75] and attributed to the presence of an alumina passive film on Al surface. The alumina passivation was explained with reactions (3), (4), and (5), as provided in [76].

$$Al - 3e^- \rightarrow Al^{3+} \qquad (3)$$

$$Al^{3+} + 3OH^- \rightarrow Al(OH)_3 \qquad (4)$$

$$2Al(OH)_3 \rightarrow Al_2O_3 + 3H_2O \qquad (5)$$

As the applied potential further increases, one expects a breakdown of this passive film to occur. The "breakdown" point is commonly defined as a turning point where the anodic current density increases rapidly as the applied potential increases at a constant rate [38]. In a review paper on pitting corrosion of Al [51], Z. S. Smialowska attributed the passivation breakdown to an increasing amount of chloride ions adsorbed to potential pitting sites of the passivated surface with an increasing anodic potential. For Al in a 20 ppm NaCl solution, the "breakdown" point at around 300 mV above E_{oc} was observed and indicated in Fig. 2a. After the complete breakdown of the passive film, the anodic dissolution of Al was under mass transfer control as the anodic current density becomes independent of the applied potential at even higher applied potential, which was also observed for the anodic polarization curves as shown in [51].

The anodic dissolution reactions of γ and θ start with a dealloying step with the formation of Al^{3+}. The reaction mechanisms are represented in reaction (6) and (7), respectively, as provided by B. Mazurkiewicz et al. [38], N. Birbilis et al. [77], and J. Osenbach et al. [78].

$$Cu_9Al_4 - 12e^- \rightarrow 4Al^{3+} + 9Cu \quad (6)$$

$$CuAl_2 - 6e^- \rightarrow 2Al^{3+} + Cu \quad (7)$$

The formation of Al^{3+} led to surface passivation similar to Al. Hence, the observed Tafel slopes are 216 mV per decade of current for γ and 209 mV per decade of current for θ. Presence of the "breakdown" points are also observed on the anodic polarization curves of γ and θ as shown in Fig. 3.3b. This anodic breakdown behavior of γ and θ was also observed by B. Mazurkiewicz et al. [38] and N. Birbilis et al. [77].

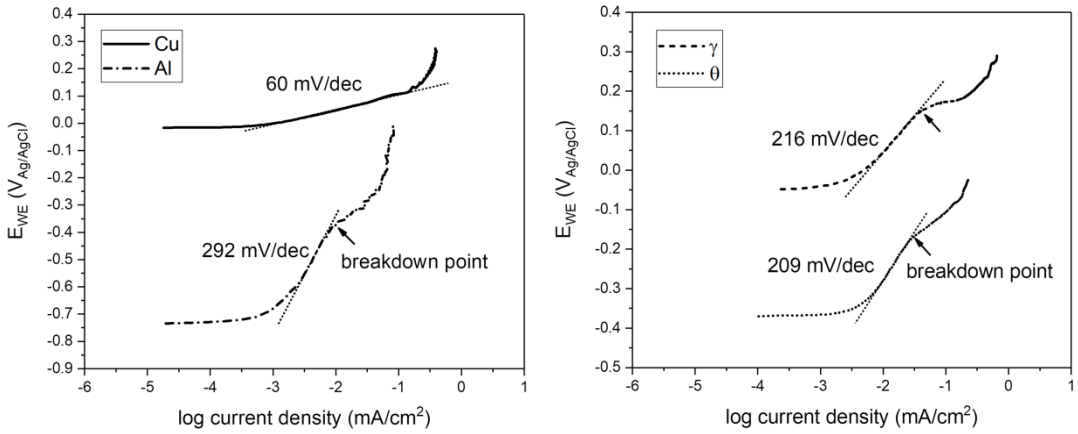

(a) (b)

Figure 3.3 (a) Anodic polarization curves of Cu and Al. (b) Anodic polarization curves of γ and θ. "Breakdown" points and values of the Tafel slopes are marked in the figure.

In summary, the difference in the anodic Tafel slope indicates different anodic dissolution behavior for Cu, Al and Cu-Al IMCs. For Cu, the low anodic Tafel slope indicates the anodic dissolution was controlled by both the charge transfer rate of Cu and the mass transfer rate of $CuCl_2^-$. For Al, the high anodic Tafel slope indicates that the anodic dissolution was inhibited by

an alumina surface passive layer. For both γ and θ, their high anodic Tafel slopes indicate similar anodic dissolution behavior to Al in terms of the active dissolution of Al and the formation of alumina passivation on the surface.

When Pd-coated Cu wire is used, Pd can only be incorporated in Cu and γ [22,40,45]. The incorporation of Pd in Cu and γ can change their electrochemical behavior in terms of passivation behavior and cathodic activity [79]. These changes are reflected by the shift of the anodic and cathodic polarization curves. The shifts of the polarization curves lead to changes in the E_{oc} and i_{corr} values [80]. Environmental factors such as pH, chloride concentration of the electrolyte and temperature also affect the anodic and cathodic polarization behavior and thus the E_{oc} and i_{corr} values. Synergic effects of Pd and environmental factors on the electrochemical behavior of Cu and γ are to be discussed.

3.2.3 Synergic Effect of Pd and Chloride

The polarization curves of Cu, Cu-2Pd, and Cu-9Pd measured in 100ppm, 20ppm, and 1ppm NaCl solutions with pH 6 are provided in Fig. 3.4a, 3.4b, and 3.4c, respectively. Since there were no well-defined linear regions on most of the anodic branches, the Tafel extrapolation was performed using the cathodic branches to obtain the i_{corr}, at E_{oc}, as indicated in Fig. 3.4.

The logarithm of i_{corr} was plotted versus E_{oc} for each sample in electrolytes with different NaCl concentrations, as provided in Fig. 3.5. The addition of Pd in Cu caused E_{oc} to increase and i_{corr} to decrease. For a given amount of Pd in Cu, the decrease in the NaCl concentration had a similar effect on E_{oc} and i_{corr}, although for Cu-9Pd, E_{oc} and i_{corr} became less sensitive to all NaCl concentrations investigated.

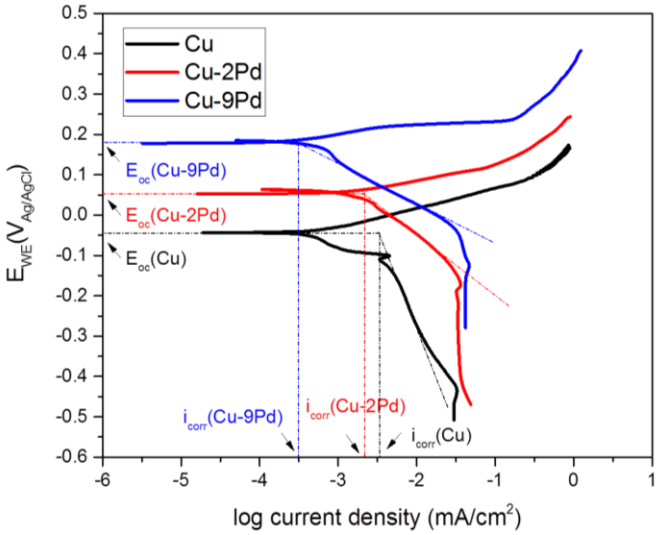

(a)

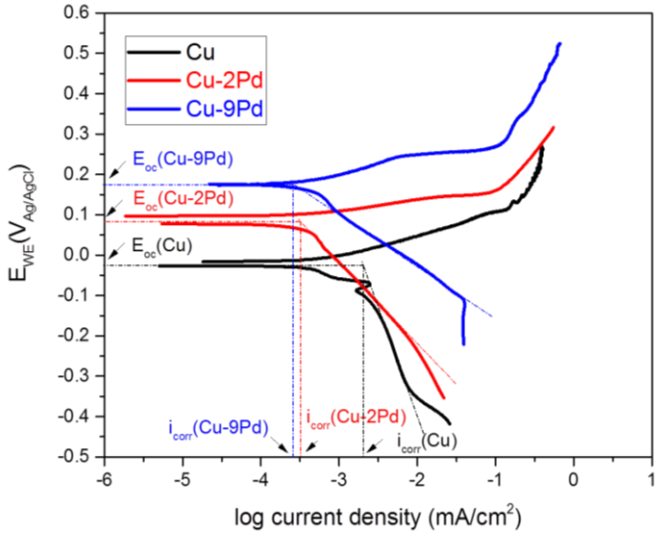

(b)

Figure 3.4 Polarization curves of Cu, Cu-2Pd, and Cu-9Pd in near neutral electrolyte solution containing (a) 100ppm NaCl, (b) 20ppm NaCl, (c) 1ppm NaCl. The values of potential were corrected by $R_{soln,}$ and the linear regime of the cathodic branch was extrapolated back to E_{oc} to obtain i_{corr}.

Figure 3.4 (cont'd)

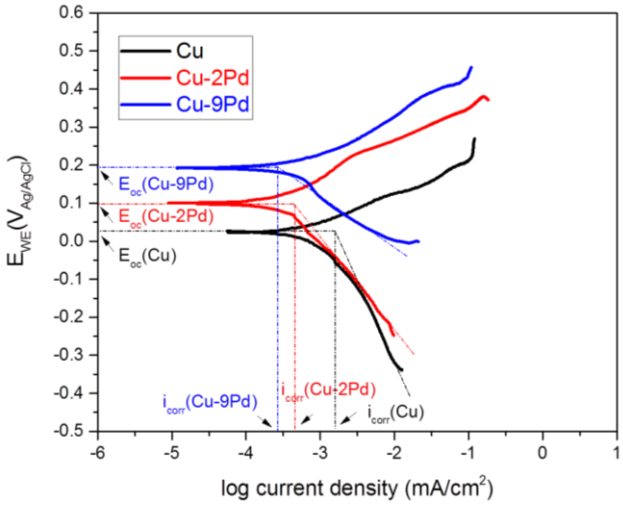

(c)

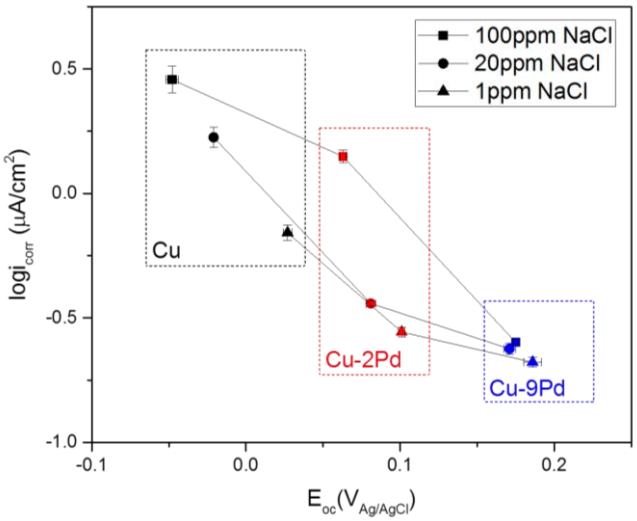

Figure 3.5 E_{corr} and *log* i_{corr} of Cu, Cu-2Pd, and Cu-9Pd in a nearly neutral electrolyte solution of different NaCl concentrations (■: 100ppm; ●: 20ppm; ▲: 1ppm)

These observations can be explained based on the influence of Pd addition and/or NaCl concentration variations on the rate of cathodic and anodic reactions. Pd, a platinum-group metal, is known to catalyze the O_2 reduction [74,81]. The catalytic activity of Pd for ORR caused the cathodic current density to systematically increase with the increasing Pd addition, as observed in Fig. 3.4a, 3.4b, and 3.4c. The surface of a Cu-Pd alloy corrodes in the form of selective

leaching of Cu, which enriches the more noble Pd on the surface [79,82,83]. The formation of a Pd-enriched layer was found to passivate the surface [82,83]. The passivation significantly inhibited the Cu leaching and therefore lower the anodic current density. This passivation was clearly visible for Cu-9Pd by the appearance of "breakdown" points, as seen in Fig. 3.4a and 3.4b. This rapid anodic current density increase after the breakdown point was due to the breakdown of the Pd-enriched film at high positive overpotential and the associated active dissolution of Cu from the unprotected surface [83]. The breakdown point, however, was not observed for undoped Cu. On the other hand, Fig. 3.4a, 3.4b, and 3.4c also showed that the anodic current density consistently decreased with the increasing Pd addition. These two observations can both be attributed to the surface Pd enrichment.

Based on the discussion above, increasing Pd concentration simultaneously increased the cathodic current density and decreased the anodic current density. As seen in Fig. 3.4, for a given potential, the current density shifted to lower values for the anodic branch, and to higher values for the cathodic branch. This resulted in an increase in E_{oc} with the Pd addition. The shift for the anodic branch was greater than the shift for the cathodic branch, which resulted in the lowering of the i_{corr} value.

The anodic dissolution rate of Cu was accelerated by the presence of chloride due to its direct involvement in the anodic dissolution reactions of Cu as shown in reaction (3) and (4). On the other hand, the cathodic reaction rate of Cu was not significantly changed by the presence of chloride since chloride was not directly involved in the ORR. For a given potential, an increase in the chloride concentration caused the current density to shift to a higher value for the anodic branch, while did not change the current density for the cathodic branch. Thus, E_{oc} decreased and i_{corr} increased with the increasing NaCl concentration. This was observed for both Cu and Cu-

2Pd alloys, as shown in Fig. 3.5. With a more significant amount of Pd addition to Cu (i.e., Cu-9Pd), the Pd-enriched layer inhibited the diffusion of Cu to the surface, which reduced the rate of CuCl formation and thus resulted in a low sensitivity of the anodic current density to the chloride concentration. Therefore, E_{oc} and i_{corr} of Cu-9Pd became less sensitive to the NaCl concentration.

The polarization curves of γ #1, γ #2, and γ #3 measured in 100ppm, 20ppm, and 1ppm NaCl solutions with pH 6 are provided in Fig. 3.6a, 3.6b, and 3.6c, respectively. Unlike Cu and Cu-Pd alloys, well-defined linear regions on both the cathodic and anodic braches were observed for γ and Pd-containing γ IMCs. Anodic Tafel extrapolation was used to obtain i_{corr} values at E_{oc} as indicated in Fig. 3.6.

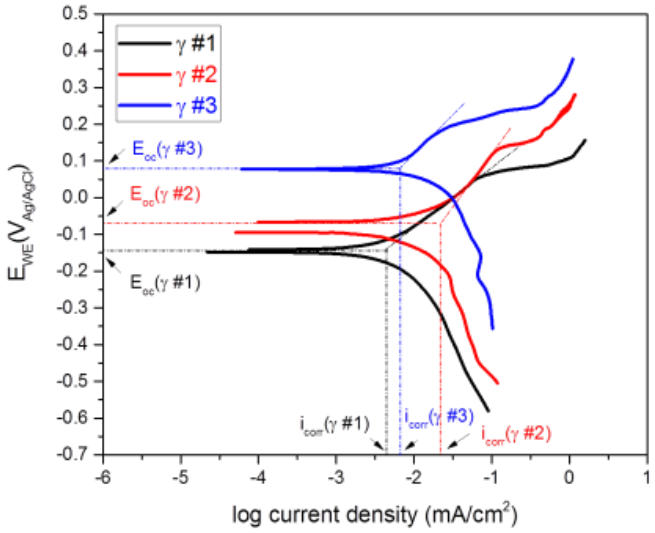

(a)

Figure 3.6 Polarization curves of γ #1, γ #2, and γ #3 in near neutral electrolyte containing (a) 100ppm NaCl, (b) 20ppm NaCl solution, (c) 1ppm NaCl. The values of potential were corrected by $R_{soln,}$ and the linear regime of the anodic branch was extrapolated back to E_{oc} to obtain i_{corr}.

Figure 3.6 (cont'd)

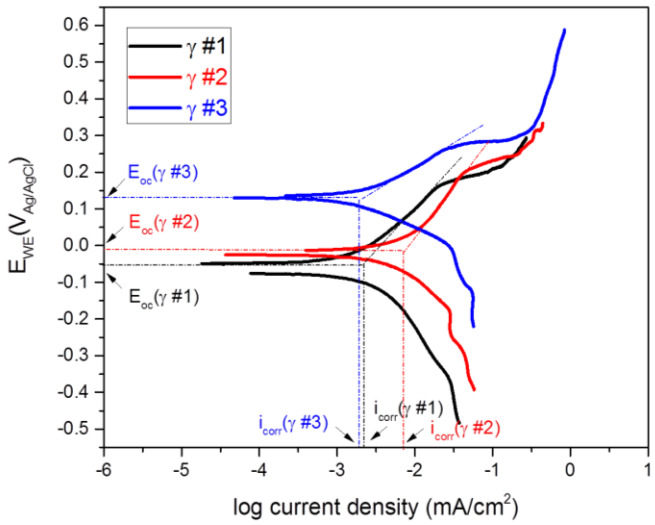

(b)

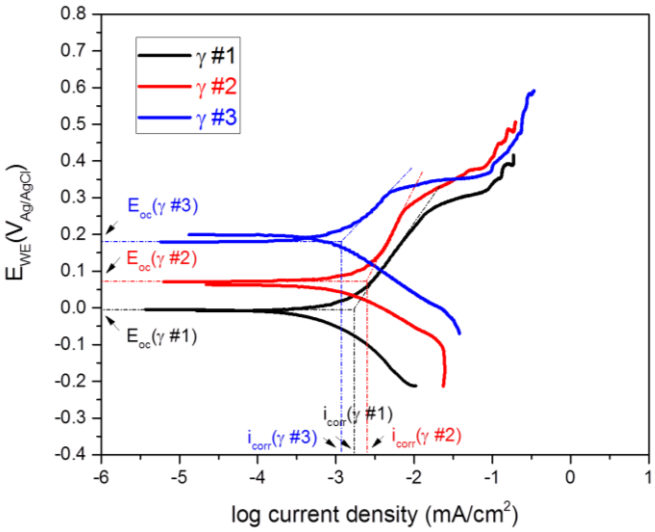

(c)

The logarithm of i_{corr} was plotted versus E_{oc} for all γ IMCs in solutions with different NaCl concentrations as presented in Fig. 3.7. For a given NaCl concentration, the addition of Pd in γ caused the value of E_{oc} to increase systemically. It was also observed that of all three different NaCl concentrations investigated, γ #2 (γ made with Cu-2Pd) had the highest value of i_{corr}. For a given amount of Pd in the γ IMC, decreases in the NaCl concentration caused E_{oc} to increase and

i_{corr} to decrease systemically. In addition, unlike the case of Cu-9Pd, E_{oc} and i_{corr} of γ #3 were sensitive to the NaCl concentrations investigated.

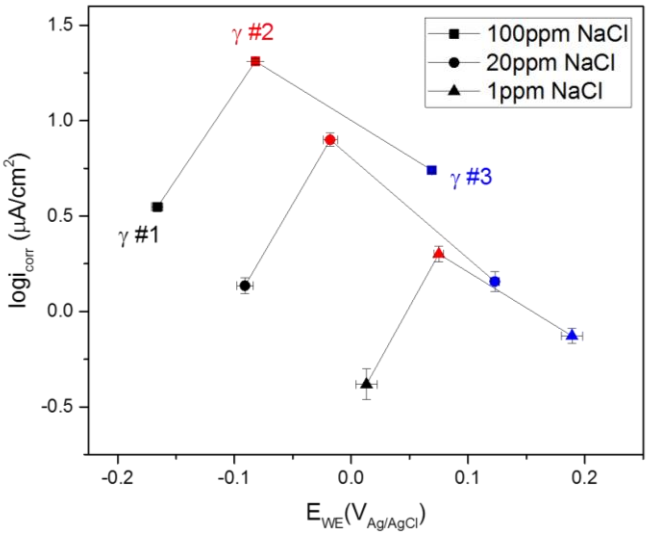

Figure 3.7 E_{corr} and $logi_{corr}$ of γ #1, γ #2 and γ #3 in near neutral electrolyte of different NaCl concentrations (■: 100ppm; ●: 20ppm; ▲: 1ppm)

As with Cu-Pd alloys, the high catalytic activity of Pd to ORR caused the cathodic current density of γ IMCs to increase systemically with increasing amounts of Pd addition as seen in Fig 3.6. The anodic current density was not significantly reduced when a small amount of Pd was used in γ #2. As seen from Fig 3.6, for a given potential, the current density shifted to higher values for the cathodic branch but remained almost unchanged for the anodic branch. This might be attributed to the presence of Al in γ. The passivation of Al hydroxide from reaction (6) and Al oxide from reaction (7) might be more dominant than the Pd surface enrichment observed in the Cu-Pd alloy. This indicates that a small amount of Pd addition in γ is insufficient to reduce the value of i_{corr}.

The presence of chloride accelerates the anodic dissolution rate of γ IMCs by weakening the passive film [51]. Therefore, E_{oc} was decreased and i_{corr} was increased with an increasing NaCl concentration. This was observed for all the γ IMCs, as shown in Fig. 3.7. E_{oc} and i_{corr} of γ #3

remained sensitive to chloride concentration since chloride can preferentially attack Al oxide, inhibit the formation of the passivation film, and thus cause the anodic current density to increase [51]. The fact that Pd concentration in γ #3 was lower than that of Cu-9Pd might also have contributed to the observed sensitivity to NaCl concentration.

Although XRD analysis indicates that Pd was not able to be homogeneously incorporated in θ, the same electrochemical study was also conducted for θ #1, θ #2, and θ #3 as verification. The cathodic and anodic polarization curves of θ #1, θ #2, and θ #3 in a 100ppm NaCl solution are provided in Fig. 3.8. Pd addition did not show any significant effect on either anodic or cathodic polarization behavior. Therefore, both E_{oc} and i_{corr} values were independent of Pd addition. There are two possible reasons for this lack of influence of Pd addition on the polarization behavior of θ: First, the atomic fraction of Pd was diluted by a large amount of Al in θ, and second, the spatial distribution of Pd in θ was inhomogeneous. The latter should be the dominant reason since the XRD analysis also showed the existence of multiple phases (undoped θ, Pd-doped γ, and pure Al) in the Pd-doped θ samples.

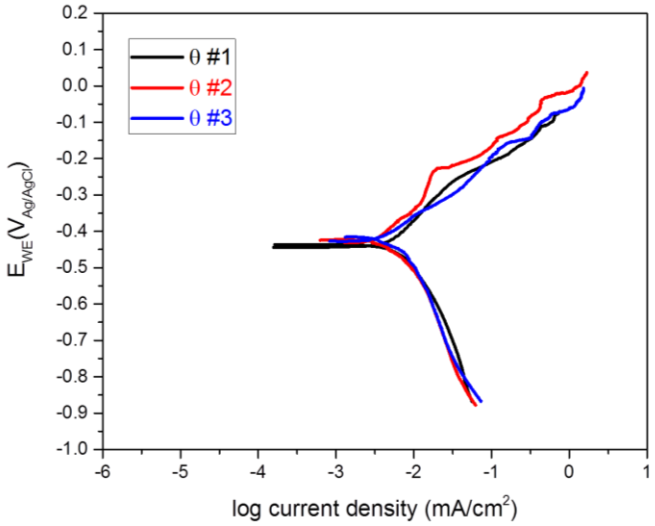

Figure 3.8 Polarization curves of θ #1, θ #2, and θ #3 in near neutral electrolyte containing 100ppm NaCl.

3.2.4 Synergic Effect of pH and Pd

The polarization curves of Cu, Cu-2Pd, and Cu-9Pd measured in 20ppm NaCl solutions with three pH values: 4, 6, and 9 are provided in Fig. 3.9a, 3.9b, and 3.9c, respectively. Due to the lack of well-defined linear regions on the anodic branches, the cathodic Tafel extrapolation was performed to obtain the i_{corr}, at E_{oc}.

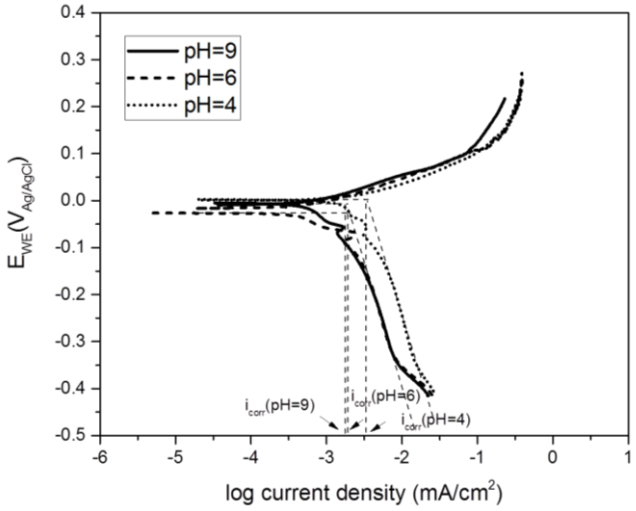

(a)

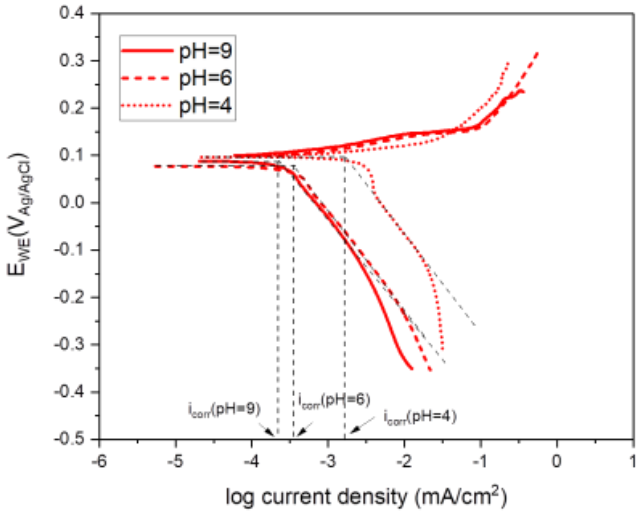

(b)

Figure 3.9 Effect of pH on the polarization curves of (a) Cu, (b) Cu-2Pd, (c) Cu-9Pd in a 20ppm NaCl solution. The i_{corr} values were obtained by extrapolating the linear regimes of the cathodic polarization curves back to E_{oc}.
Figure 3.6 (cont'd)

Figure 3.9 (cont'd)

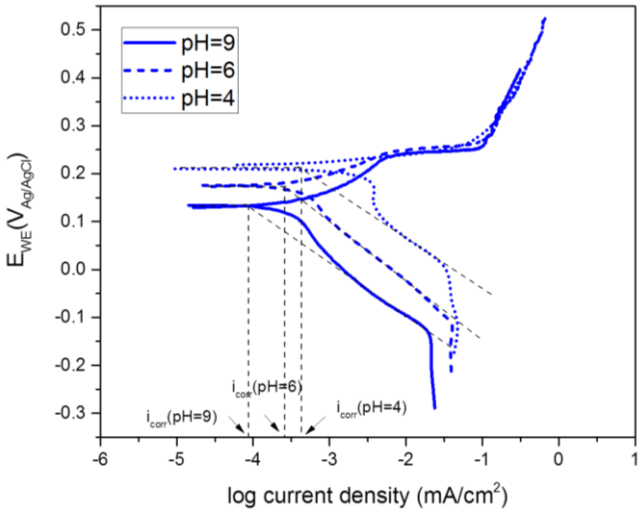

(c)

The logarithm of i_{corr} was plotted versus E_{oc} for each sample in electrolytes with different pH values, as provided in Fig. 3.10. The decrease in pH value caused both the E_{oc} value and the i_{corr} value to increase for all Cu and Cu-Pd alloys. Notably, the Cu-Pd alloys showed a significantly higher sensitivity to pH than Cu.

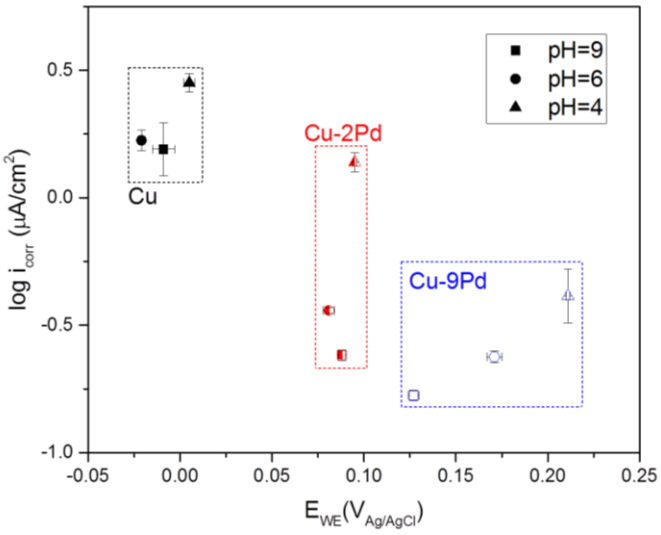

Figure 3.10 E_{corr} and *log* i_{corr} of Cu and Cu-Pd alloys in a 20ppm NaCl solution (■: pH=9; ●: pH=6; ▲: pH=4)

The anodic reaction mechanism of Cu doesn't involve proton as indicated in equation (3) and (4). Thus the anodic current density was insensitive to pH. The dominant cathodic reaction of Cu is ORR given in equation (1) [84,85]. Based on the Nernst equation, the equilibrium potential of ORR can be expressed in equation (10) assuming 25°C and unit H_2 and O_2 partial pressure:

$$E_{O_2/H_2O} = 1.032 - 0.059pH \qquad (10)$$

During the cathodic polarization measurement, the cathodic polarization imposed on ORR, which is the difference between E_{O_2/H_2O} and E_{WE}, determines the cathodic current density. A higher cathodic polarization normally leads to a higher cathodic current density. According to the equation (10), E_{O_2/H_2O} increases with a decreasing pH. At a given E_{WE}, the cathodic polarization is higher at a lower pH value. This explains why the cathodic current density of Cu increased slightly as the pH decreased from 6 to 4. However, the increase was not significant since ORR was limited by oxygen diffusion during the cathodic polarization measurement [84]. Therefore, the E_{oc} and i_{corr} values of Cu were not sensitive to pH as indicated in Fig. 3.10.

The cathodic reactions of Cu-Pd alloys should involve HER due to the high catalytic activity of Pd to HER [74]. For Cu-9Pd, the involvement of HER became more obvious. As shown in Fig. 3.9c, the cathodic current density of Cu-9Pd reached a maximum value and became independent of the E_{WE} value as the cathodic sweep continued. The occurrence of a maximum current density commonly referred to as the limiting current density is due to the diffusion limitation of oxygen from the bulk electrolyte to sample surface [84]. The increase in the limiting current density should be due to the enhanced kinetics of HER on the Cu-Pd surface. Hence, the cathodic current density of Cu-Pd alloys increased much faster than Cu with decreasing pH value. The anodic current density of Cu-Pd alloys was not significantly changed by pH since the surface passivation caused by the Pd enrichment had high resistance to pH [79,82,83].

Based on the discussion above, the cathodic current density of Cu and Cu-Pd alloys increased with a decreasing pH, while the anodic current density remained unchanged. This resulted in an increase in both the E_{oc} and i_{corr} values. Due to the enhanced HER rate, the cathodic current density of Cu-Pd alloys increased much faster than Cu with a decreasing pH. This caused the E_{oc} and i_{corr} values of Cu-Pd alloys to increase faster than those of Cu as well.

Notably, as shown in Fig. 3.10, for both Cu and Cu-2Pd alloy, the increase in E_{oc} was not as significant as the increase in i_{corr}. On the contrary, for the Cu-9Pd alloy, the increase in E_{oc} was more significant than the increase in i_{corr}. This can be understood from the morphological characteristics of their anodic polarization curves. The Tafel slopes of the anodic polarization curves of Cu and Cu-2Pd alloy were low, which was around 60 mV/dec. Although the cathodic branch shifted to the left with a decreasing pH, the crossover moved much further along the current axis than the potential axis. Therefore, the i_{corr} value appeared to be more sensitive to pH than the E_{oc} value. On the other hand, the Tafel slope of the anodic polarization curve of Cu-9Pd was much higher. Due to the passivation caused by the Pd surface enrichment, the anodic current density increased slower than Cu and Cu-2Pd alloy as the applied potential increased. Therefore, as the cathodic branch shifted to the left with a decreasing pH value, the crossover moved further along the potential axis than the current axis. Thus, the E_{oc} value seemed to be more sensitive to pH than the i_{corr} value.

The polarization curves of γ #1, γ #2, and γ #3 measured in 20ppm NaCl solutions with three various pH values: 4, 6, and 9 are provided in Fig. 3.11a, 3.11b, and 3.11c, respectively. The anodic Tafel extrapolation was performed to obtain the i_{corr} values at E_{oc}.

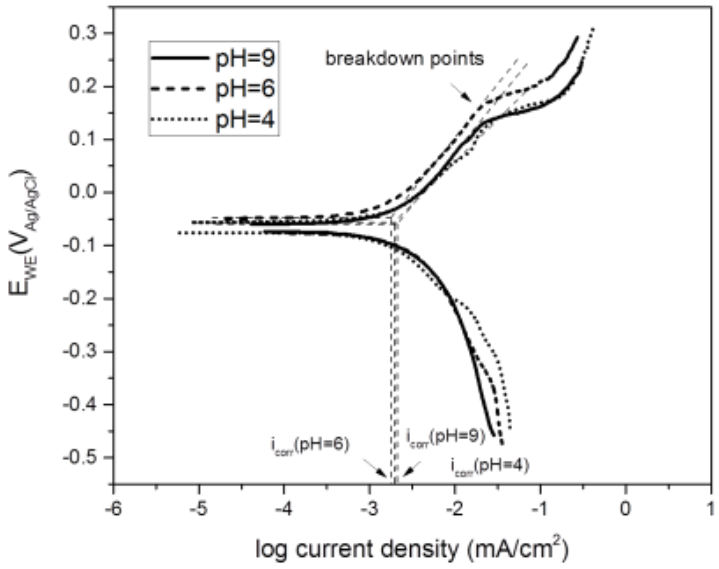

(a)

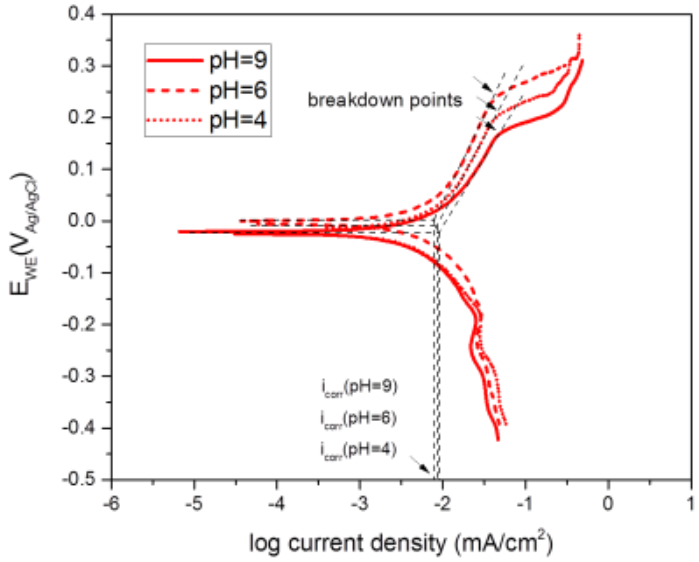

(b)

Figure 3.11 Effect of pH on the polarization curves of (a) γ #1, (b) γ #2, (c) γ #3 in the 20ppm NaCl. The values of i_{corr} were obtained by extrapolating the linear regimes of the anodic polarization curves back to E_{oc}.

Figure 3.11 (cont'd)

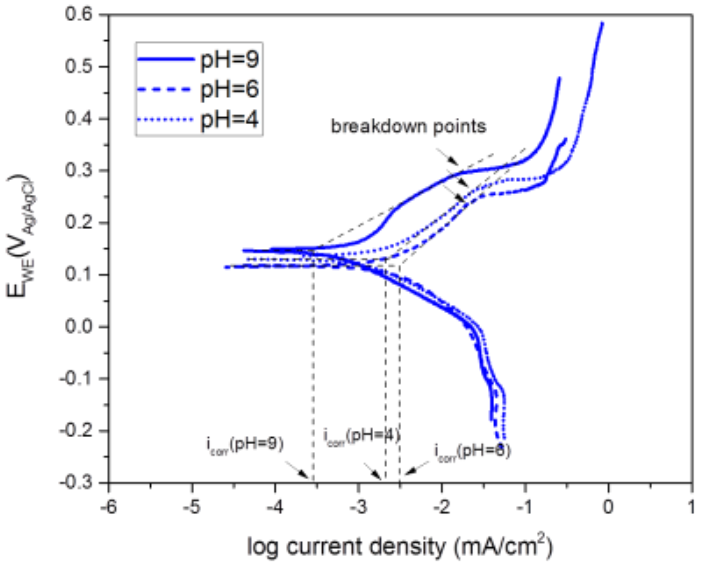

(c)

The logarithm of i_{corr} was plotted versus E_{oc} for each sample in electrolytes with different pH values as provided in Fig. 3.12a, 3.12b, and 3.12c. For γ #1 and γ #2, both the E_{oc} and i_{corr} values were insensitive to pH. For γ #3, the E_{oc} value was not significantly changed by pH either, while its i_{corr} value increased with decreasing pH value.

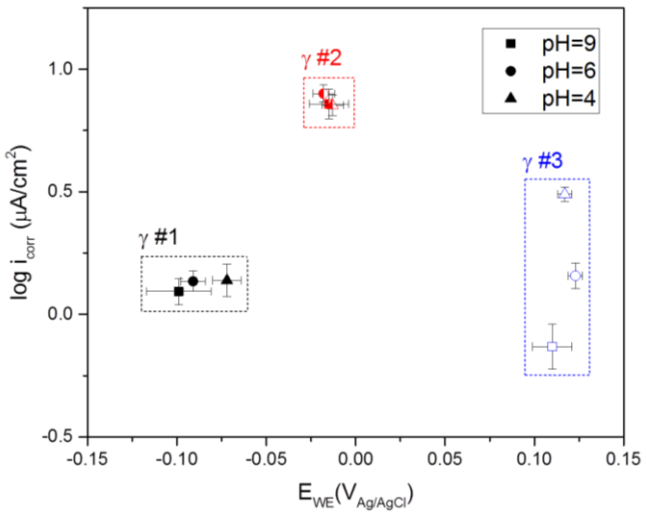

Figure 3.12 E_{corr} and *log* i_{corr} of γ #1, γ #2 and γ #3 in a 20ppm NaCl solution (■: pH=9; ●: pH=6; ▲: pH=4)

As discussed before, γ #1 surface was passivated by alumina. The alumina layer has low solubility and low electronic conductivity in a solution with pH ranging between 4 and 9 [51]. Therefore, the anodic current density was insensitive to pH due to the high stability of the passive film. Due to its electrically-insulating nature, the alumina layer is not catalytic to the cathodic reactions [51]. This explains the insensitivity of the cathodic current density to pH. Therefore, the E_{oc} and i_{corr} values of γ #1 were not significantly affected by pH. The polarization behavior of γ #2 was similar to that of γ #1 in terms of stable passivation and low catalytic activity to the cathodic reactions. Therefore, both E_{oc} and i_{corr} of γ #2 were not significantly affected by pH as well.

Due to a higher amount of Pd addition, Pd enrichment on the surface was likely to happen as γ #3 corroded. Both this Pd-enriched layer and alumina contributed to the observed passivation in the anodic polarization measurement. Since alumina is stable in the solutions of all pH values, the lower anodic current density in the solution of pH 9 might be due to the higher stability of the Pd-enriched layer in an alkaline environment. The cathodic current density was insensitive to pH due to the presence of the passive alumina layer as introduced before. Therefore, the i_{corr} value of γ #3 increased with a decreasing pH.

3.2.5 Synergic Effect of Temperature and Pd

The polarization curves of Cu, Cu-2Pd, and Cu-9Pd measured in 20ppm NaCl solutions of pH 6 under three temperatures: 25°C, 45°C and 65°C are provided in Fig. 3.13a, 3.13b, and 3.13c. No well-defined linear regimes can be seen on the anodic branches. Thus the Tafel extrapolation on the cathodic branches was performed to obtain i_{corr} at E_{oc}.

The logarithm of i_{corr} was plotted versus E_{oc} as provided in Fig. 3.14. The E_{oc} values of Cu and Cu-2Pd was not significantly affected by temperature. The E_{oc} value of Cu-9Pd increased

with the increasing temperature, especially when the temperature increased from 45°C to 65°C. The i_{corr} value of Cu and Cu-2Pd increased with the increasing temperature systemically. The i_{corr} value of Cu-9Pd increased when the temperature increased from 25°C to 45°C and decreased when the temperature further increased from 45°C to 65°C.

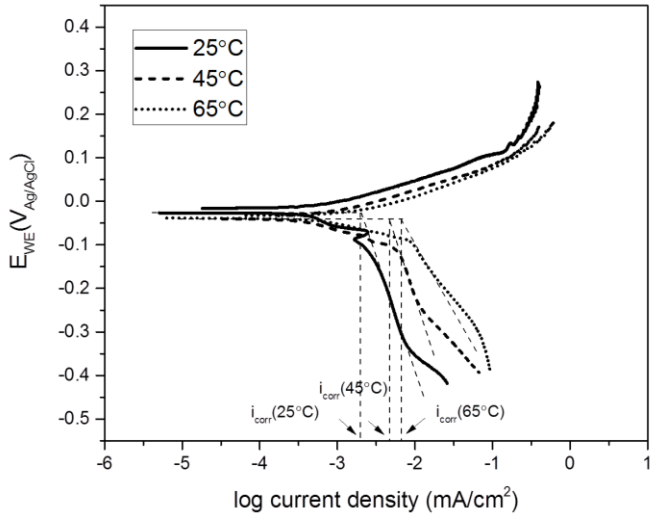

(a)

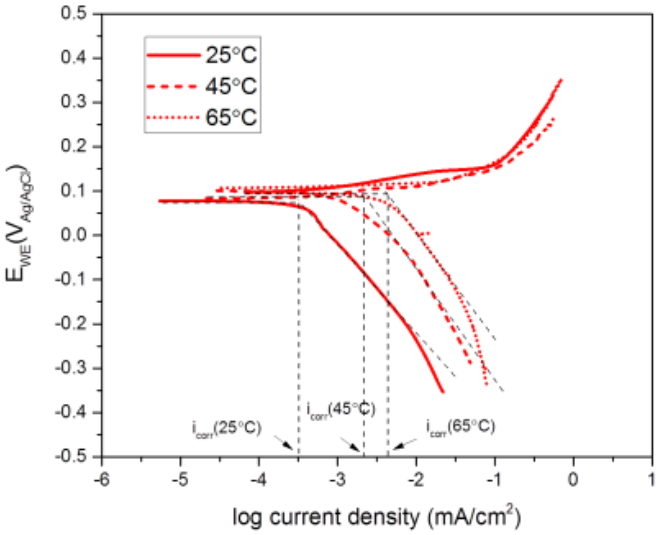

(b)

Figure 3.13 Effect of temperature on the polarization curves of (a) Cu, (b) Cu-2Pd, (c) Cu-9Pd in a 20ppm NaCl solution. The values of i_{corr} were obtained by extrapolating the linear regimes of the cathodic polarization curves back to E_{oc}.

Figure 3.13 (cont'd)

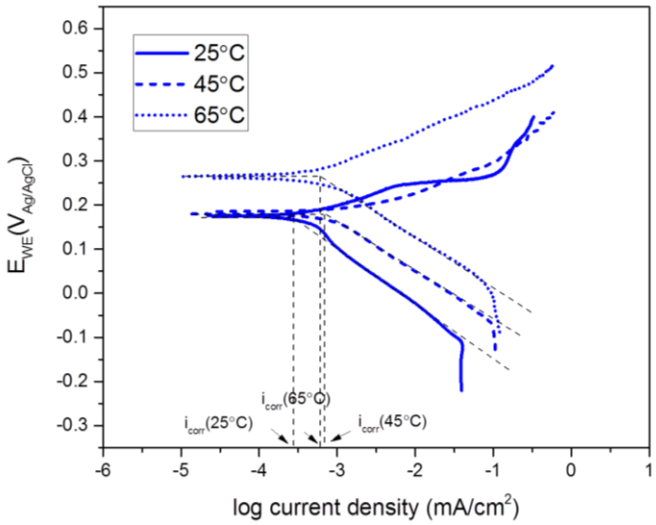

(c)

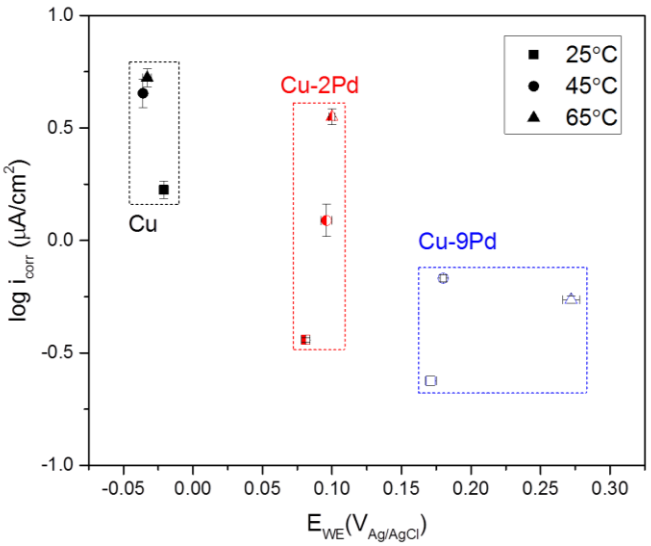

Figure 3.14 E_{corr} and *log* i_{corr} of Cu and Cu-Pd alloys in the 20ppm NaCl solution (■: 25°C; ●:45°C; ▲:65°C)

For Cu, the anodic polarization curves measured under the three temperatures exhibited almost the same anodic Tafel slope of 60mV/dec. This indicates that the anodic reaction mechanism, which was a mixed-control of the charge transfer process of Cu and mass transfer process of $CuCl_2^-$, didn't change within the temperature range investigated [52]. Despite showing a subtle increase, the anodic current density of Cu was not sensitive to temperature. The cathodic

reaction was controlled by the ORR charge transfer and the oxygen diffusion as discussed before. The oxygen diffusion rate in the bulk electrolyte increases with increasing temperature due to an increasing oxygen diffusion coefficient [86]. With a more swift oxygen supply, the cathodic reaction became more controlled by the charge transfer process. This explains a decrease in the cathodic Tafel slope and an increase in the cathodic current density as the temperature increased. With the anodic current density unchanged, the increase of the cathodic current density with the increasing temperature led to an increase in i_{corr} as seen in Fig 3.14. Due to the low Tafel slope of the anodic polarization curve, the increase of E_{oc} was not as visible. Like Cu, the anodic current density of Cu-2Pd was not sensitive to temperature while its cathodic current density increased with the increasing temperature as seen in Fig. 3.13b. Therefore, i_{corr} of Cu-2Pd increased with increasing temperature. Due to the low Tafel slope of the anodic branch, E_{oc} of Cu-2Pd was not significantly increased with the increase in the cathodic current density.

The anodic current density of Cu-9Pd was not significantly changed when the temperature increased from 25°C to 45°C. However, it exhibited a dramatic decrease when the temperature increased from 45°C to 65°C. This implies the formation of a passive surface layer caused by the rapid Cu dissolution and Pd enrichment. The Pd-enriched layer was stable and protective enough such that the rapid dissolution of Cu was effectively inhibited despite the high temperature. The cathodic current density of Cu-9Pd increased consistently with the increasing temperature. Therefore, as the temperature increased from 25°C to 45°C, the more dominant increase in the cathodic current density caused E_{oc} and i_{corr} to increase. However, as the temperature further increased from 45°C to 65°C, the cathodic current density kept increasing, while the anodic current density showed a significant decrease. This resulted in an increase of E_{oc}, however, a

decrease of i_{corr} because the anodic current density was more significant than the increase of the cathodic current density.

The polarization curves of γ #1, γ #2, and γ #3 measured in a pH 6, 20ppm NaCl solution under three different temperatures: 25°C, 45°C and 65°C are provided in Fig 3.15a, 3.15b, and 3.15c. Anodic Tafel extrapolation was performed to obtain i_{corr} at E_{oc}. The logarithm of i_{corr} was plotted versus E_{oc} as provided in Fig. 3.16. For all γ IMCs, E_{oc} decreased and i_{corr} increased with the increasing temperature systemically.

The anodic current density of γ #1 increased systemically with the increasing temperature as seen in Fig. 3.15a. The breakdown potential was lower and the corresponding anodic dissolution current density was higher under a higher temperature. This indicates that the surface passivation became weaker as the temperature increased. The oxygen solubility in water decreases with an increasing temperature [87]. According to equations (5)-(7), the formation of an alumina passive layer requires a sufficient amount of oxygen in the solution. Therefore, the increase in the anodic current density can be attributed to the low oxygen content in the solution. The cathodic current density increased with the increasing temperature due to the increase in the HER rate. The simultaneous increase of the cathodic and anodic current densities caused i_{corr} to increase. The higher increase of the anodic current density than the increase of the cathodic current density caused E_{oc} to decrease. Similarity, the anodic current density of γ #2 and γ #3 increased systemically with the increasing temperature due to the weakening of the surface passive film, which was indicated by a lower breakdown potential and a higher corresponding anodic current density as well. Notably, the anodic current density of γ #3 did not experience a decrease like Cu-9Pd did as the temperature increased from 45°C to 65°C. This might be due to the insufficient Pd enrichment in γ #3. The cathodic current density of γ #2 and γ #3 also increased

with the increasing temperature, although not as significantly as the anodic current density did. Thus, due to a more significant decrease in the anodic current density as compared with the increase in the cathodic current density, E_{oc} decreased and i_{corr} increased with the increase of temperature for γ #2 and γ #3.

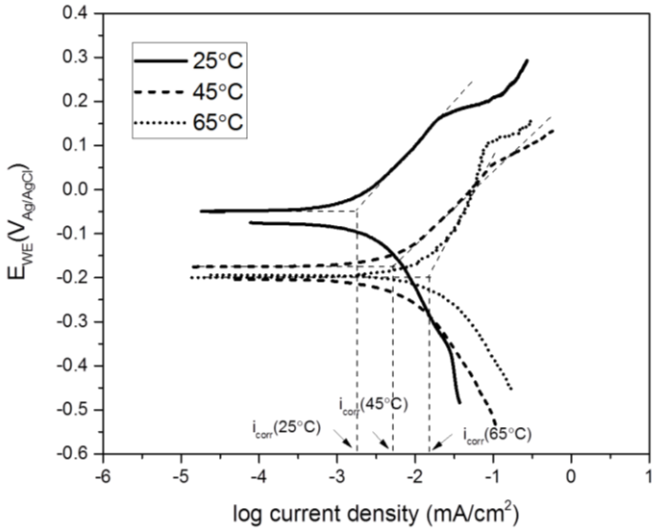

(a)

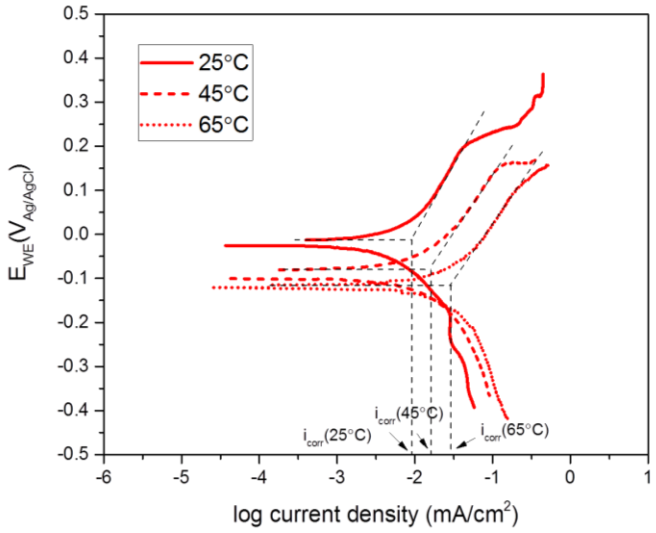

(b)

Figure 3.15 Effect of temperature on the polarization curves of (a) γ #1, (b) γ #2, (c) γ #3 in the 20ppm NaCl. The values of i_{corr} were obtained by extrapolating the linear regimes of the anodic polarization curves back to E_{oc}.

Figure 3.15 (cont'd)

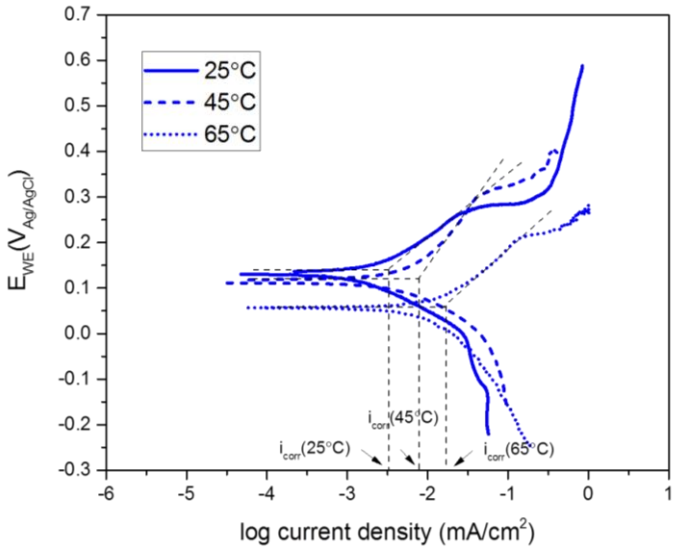

(c)

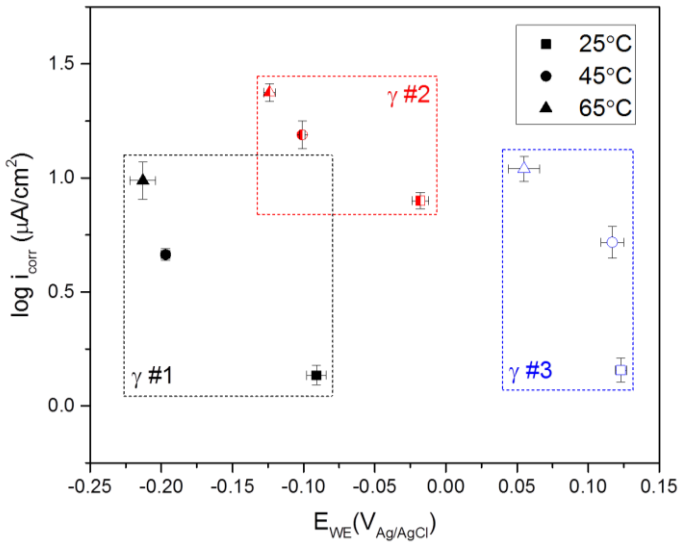

Figure 3.16 E_{corr} and *log* i_{corr} of γ #1, γ #2 and γ #3 in the 20ppm NaCl solution (■: 25°C; ●:45°C; ▲:65°C)

3.3 Conclusions

3.3.1 Pd and Chloride Effect

From XRD analysis, Pd can be homogeneously incorporated into γ IMC but not into θ IMC. Electrochemical behavior of undoped and Pd-doped Cu and γ in a near neutral electrolyte with

various NaCl concentrations were investigated using bulk samples. Effects of Pd addition and chloride concentration on the cathodic and anodic polarization behavior of these entities were evaluated. Key corrosion parameters including E_{oc} and i_{corr} as influenced by the Pd addition and chloride concentration were reported. Some significant conclusions are as follows:

Cu-Pd is an isomorphous solid solution. The addition of Pd decreased the anodic current density of Cu due to the high nobility of Pd and its enrichment on the surface during the anodic dissolution. The Pd addition increased the cathodic current density due to the high catalytic activity of Pd to cathodic reactions. The decrease in the anodic current density and the increase in the cathodic current density caused E_{oc} to increase. The decrease in the anodic current density was found to be more significant than the increase in the cathodic current density. This caused i_{corr} to decrease.

For Cu and Cu-Pd alloys, a decrease in the NaCl concentration decreased the anodic current density due to less formation of CuCl. The cathodic current density, however, was not changed by the NaCl concentration since chloride was not directly involved in the cathodic reactions. A decrease in NaCl concentration caused the E_{oc} to increase and i_{corr} to decrease. Notably, with a higher Pd addition like Cu-9Pd, E_{oc} and i_{corr} became less sensitive to the NaCl concentration due to the passivation of the Pd-enriched layer on its surface.

The anodic dissolution of γ was dominated by Al as indicated by the reaction: $Cu_9Al_4\text{-}12e^- \rightarrow 4Al^{3+} + 9Cu$; A small amount of Pd present in γ, like γ #2, was insufficient to reduce the anodic current density. However, the amount of Pd in γ #2 was sufficient to increase the cathodic current density due to the high catalytic activity of Pd to cathodic reactions. Therefore, both E_{oc} and i_{corr} values of γ #2 were higher than those of γ #1. As more Pd was added (as in γ #3), the anodic current density decreased due to the Pd surface enrichment. The increase in the cathodic

current density due to the presence of Pd remained. This resulted in a continuous increase in the E_{oc} value with an increasing amount of Pd addition. However, the decrease in the anodic current density offset the increase in the cathodic current density. This led to a lowering of i_{corr}. Thus, the i_{corr} of γ #3 became lower than the i_{corr} of γ #2.

For γ IMCs, a decrease in the NaCl concentration decreased the anodic current density due to more protective surface passivation. The cathodic current density, however, was not changed. Therefore, the decrease in the anodic current density caused E_{oc} to increase and i_{corr} to decrease. Notably, unlike Cu-9Pd, the E_{oc} and i_{corr} of γ #3 were still sensitive to all NaCl concentrations investigated, due to the anodic dissolution of Al by chloride.

The presence of Pd is always beneficial for Cu by increasing the nobility and decreasing its self-corrosion rate. However, a critical amount of Pd is needed to inhibit the self-corrosion behavior of γ IMCs. Reducing the chloride concentration is always efficient in reducing self-corrosion of all metallic entities found in the Pd-coated Cu wire-bonding package.

3.3.2 Pd and pH Effect

Electrochemical behavior of undoped and Pd-doped Cu and γ in 20ppm NaCl solutions with various pH values: 4, 6 and 9 were investigated. Effect of Pd and pH on the polarization behavior and the resulting E_{oc} and i_{corr} of Cu and γ were evaluated. Some significant conclusions from this study are given below:

For Cu, regardless of Pd addition, the anodic current density was not significantly influenced by pH because proton was not involved in the anodic reaction. The cathodic current density increased with a decreasing pH due to a positive shift of the equilibrium potential of ORR and the resulting increase in the cathodic polarization imposed on the cathodic reaction. Due to the high catalytic activityof Pd for HER, the increase became more significant with an increasing Pd

addition. i_{corr} of Cu and Cu-Pd alloys increased with the decreasing pH because of the increase in the cathodic current density. E_{oc} of Cu and Cu-2Pd didn't increase as significantly due to a small anodic Tafel slope value. E_{oc} of Cu-9Pd increased with a decreasing pH more significantly because of a higher anodic Tafel slope caused by surface passivation of a Pd-enriched layer.

For γ #1 and γ #2, the anodic current density was not significantly influenced by pH due to the high stability of passive alumina layer. The cathodic current density was not significantly influenced by pH either due to the covering of the poorly catalytic alumina. Therefore, E_{oc} and i_{corr} were not sensitive to pH. For γ #3, the cathodic current density remained insensitive to pH, while the anodic current density was found to increase with a decreasing pH, which might be due to the more stable Pd-enriched layer in the alkaline solution. This resulted in an increase in i_{corr}.

Chloride concentration and pH are two common characteristics of the molding compound for IC packaging. As discussed before, regardless of the Pd addition. corrosion behavior of Cu and γ are always sensitive to chloride concentration. However, the corrosion behavior of Cu and γ are not sensitive to pH until a high amount of Pd is added. Generally speaking, increasing the pH value of the molding compound is always beneficial, especially with a higher amount of Pd addition.

3.3.3 Pd and Temperature Effect

Electrochemical behavior of undoped and Pd-doped Cu and γ in a pH 6, 20ppm NaCl solution under various temperatures: 25°C, 45°C, and 65°C were investigated. Some significant conclusions from this study are given below:

For Cu and Cu-2Pd, the cathodic current density increased with the increasing temperature due to the higher reaction rate of ORR and the higher diffusion rate of oxygen in the solution. The anodic current density, on the other hand, was not sensitive to the temperature. This

polarization behavior led to an increase in i_{corr}. E_{oc} was insensitive to temperature due to the low anodic Tafel slope of the anodic polarization curves. For Cu-9Pd, the cathodic current density increased with the increasing temperature consistently. The anodic current density was not significantly changed when the temperature increased from 25°C to 45°C. However, it was dramatically reduced when the temperature further increased from 45°C to 65°C. This decrease can be attributed to the passivation caused by Pd surface enrichment. Therefore, i_{corr} of Cu-9Pd increased when the temperature increased from 25°C to 45°C due to the increase of the cathodic current density. i_{corr} of Cu-9Pd decreased when the temperature further increased from 45°C to 65°C because the decrease of the anodic current density was more dominant than the increase of the cathodic current density. E_{oc} of Cu-9Pd increased with an increasing temperature consistently.

For γ IMCs, regardless of Pd addition, the anodic current density was significantly increased with the increasing temperature, due to the lower protectiveness of the surface passive film. The cathodic current density was less sensitive to the temperature. This polarization behavior led to an increase in i_{corr} and a decrease in E_{oc}.

CHAPTER 4 FAILURE MECHANISM OF THE Cu-Al BALL-BOND INTERFACE

4.1 Introduction

The Cu-Al ball bond interface is a layered structure with γ and θ sandwiched between the Cu ball and the Al pad. Corrosion-induced failure of this sandwich structure was usually studied using the pressure cooker test (PCT) and the highly accelerated stress test (HAST) [88]. Both PCT and HAST accelerated the bond failure due to the high temperature and high humidity condition [88]. Post-failure microstructure inspection of the Cu-Al bonding interface consistently showed that γ disappeared while Cu, θ, and Al remained [23,37]. However, no systematic and convincing arguments were made to explain the disappearance of Cu_9Al_4. Consequently, the corrosion-induced failure mechanism of the Cu-Al ball bond interface remains unclear. In this chapter, a series of electrochemical techniques such as the ZRA and polarization measurements and non-electrochemical techniques such as mass loss experiments were used to provide an explanation for the disappearance of γ and propose the corrosion mechanism of the ball bond interface under encapsulation condition.

In this study, ingots of Cu, γ, θ, and Al were brought into contact and immersed in a 20ppm NaCl electrolyte to emulate the corrosion process of the ball-bond interface. After the immersion, the mass loss of individual ingots was measured and compared. Polarization curves measured under the same conditions were used to explore the fundamental reasons for the disappearance of γ [89]. Under an encapsulated condition, the electrolyte is a thin layer solution surrounding the outer surface of these metallic entities. The high ohmic resistance of this thin-layer electrolyte may constrain the galvanic corrosion only within the adjacent entities. Therefore, mass loss experiments were also performed for the three two-metal galvanic couples consisting of two

adjacent entities at the ball bond interface: Cu and γ, γ and θ, and θ and Al. The galvanic current densities of these three galvanic couples were also measured using a zero-resistance ammeter.

4.2 Results and Discussion

4.2.1 Mass Loss Experimental of the Cu-γ-θ-Al Galvanic System

Mass loss experiment of Cu, γ, θ, and Al under contact emulating the ball-bond interface was performed to study the galvanic corrosion behavior. The exposed surface of these ingots was also compared before and after two weeks of immersion as shown in Fig. 4.1. After two weeks of immersion in a 20 ppm NaCl solution, the outer surface of θ and Al was covered with the corrosion product, while the surface of Cu and γ looked fairly clean.

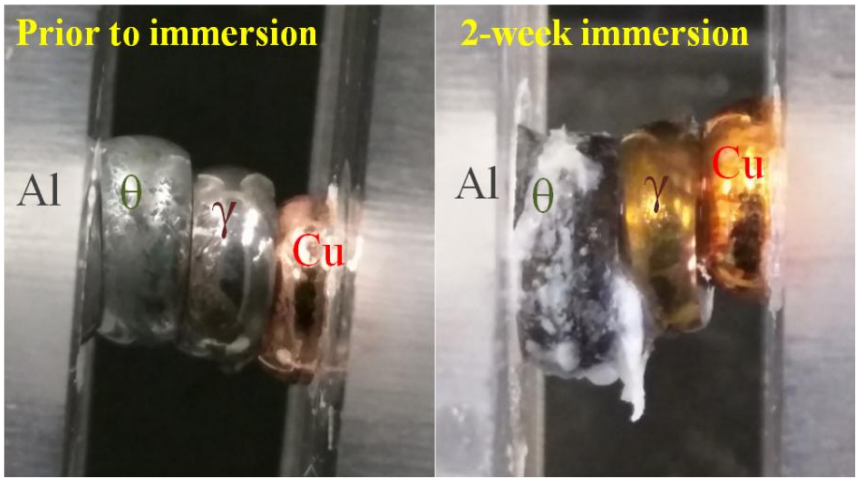

Figure 4.1 The outer surface of Cu, γ, θ, and Al ingots before and after two weeks of immersion in a near neutral 20 ppm NaCl solution.

After two weeks of immersion, the mass of each individual ingot was obtained. The mass loss results are summarized in Table 4.1. Only θ and Al showed a mass loss. This observation was compared with the E_{oc} and i_{corr} rankings for the four entities as shown in Fig. 4.2. The E_{oc} values are ranked as $E_{oc,Cu} > E_{oc,\gamma} > E_{oc,\theta} > E_{oc,Al}$, which is consistent with the E_{oc} ranking provided by A. B. Y. Lim et al. in [36]. Under the guidance of the E_{oc} data interpretation in ASTM G82-98 [35], the E_{oc} ranking implies γ has a lower tendency to corrode than θ and Al.

The i_{corr} values are ranked as $i_{corr,\theta} > i_{corr,Al} > i_{corr,\gamma} > i_{corr,Cu}$, while the $i_{corr,\theta}$ value was found to be slightly lower than the $i_{corr,\gamma}$ value by A. B. Y. Lim et al. in [36]. The discrepancy might result from different immersion times before the polarization measurement: 24 h in this study as compared to 1 h in A. B. Y. Lim et al.'s study [36]. In this study, a longer immersion time was used to ensure the sufficient surface passivation of Cu-Al IMCs and a higher reproducibility of the E_{oc} and i_{corr} measurements. Since the i_{corr} value linearly corresponds to the actual corrosion rate as pointed out in ASTM G102-89 [90], the i_{corr} ranking implies γ corrodes slower than θ and Al once it starts to corrode. Results of the mass loss and the electrochemical tests were consistent. However, they were contrary to the reported humidity reliability test of the encapsulated ball-bond interface where γ was corroded preferentially [23,37].

Table 4.1. Fractional mass loss of Cu, γ, θ, and Al ingots after two-week immersion under galvanic coupling

run No.	entity	mass before immersion (mg)*	mass after immersion (mg)*	mass loss (mg)	fractional mass loss[1] (%)
1	Cu	550.87	550.82	0.05	0.01
	γ	362.53	362.49	0.04	0.01
	θ	274.46	274.83	-0.37[2]	-0.13
	Al	213.66	212.78	0.88	0.41
2	Cu	537.71	537.70	0.01	0.00
	γ	378.59	378.45	0.14	0.04
	θ	279.43	278.91	0.52	0.19
	Al	215.41	214.25	1.16	0.54
3	Cu	531.29	531.10	0.19	0.04
	γ	372.46	372.46	0.00	0.00
	θ	282.29	282.86	-0.57[2]	-0.20
	Al	214.33	212.64	1.69	0.79

The three groups were measured during the same period of time under the same experimental conditions.
*: measured with a Model 135-S METTLER TOLEDO analytical balance with a repeatability of 0.03 mg
[1]. Fractional mass loss = 100*[(mass before - mass after immersion) / mass before]
[2]. The negative mass loss might be attributed to the redeposition of Al^{3+} in the electrolyte in the form of aluminim on the surface.

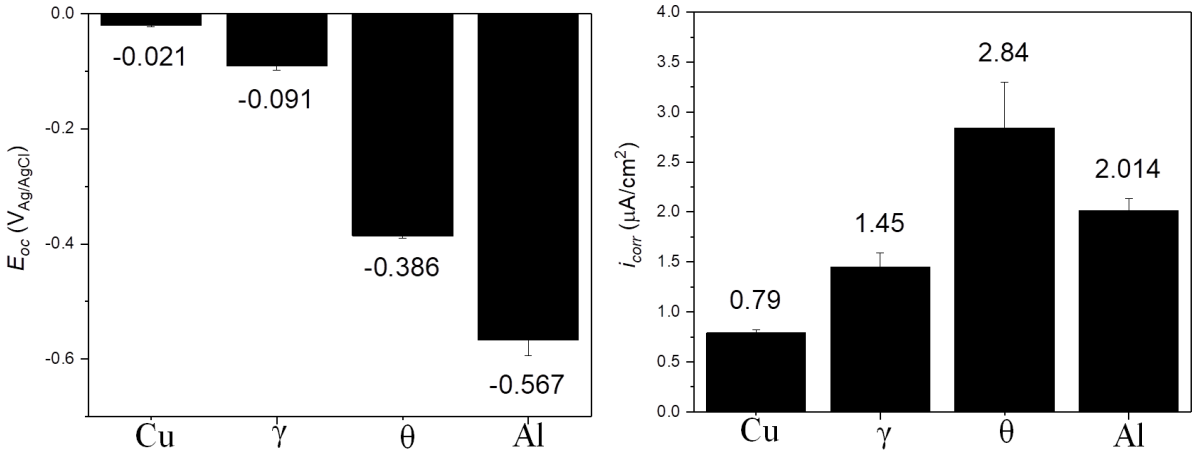

Figure 4.2 (a) E_{oc} and (b) i_{corr} values of Cu, γ, θ, and Al.

4.2.2 Polarization Analysis of the Cu-γ-θ-Al Galvanic System

The Cu-Al bond interface can be treated as a four-metal sandwich structure Cu-γ-θ-Al. This four-metal structure can be seen as a four-metal galvanic system. The corrosion behavior of each entity in this galvanic system is governed by the mixed potential theory [34]. The mixed potential theory implies no potential gradient exists on an electrically conducting surface. Therefore, Cu, γ, θ, and Al should corrode at the same potential. This common potential is denoted as E^*. The mixed potential theory also implies the net current of an isolated corroding system is zero. For the Cu-γ-θ-Al galvanic system to have a zero net current, the sum of the anodic current densities of all the entities should be equal to the sum of their cathodic current densities, as expressed in equation (1):

$$\sum_k i_{a,k} A_k = \sum_k i_{c,k} A_k \qquad (1)$$

where k represents one of the four entities: Cu, γ, θ, or Al, $i_{a,k}$, $i_{c,k}$, and A_k represents the anodic dissolution current density, the cathodic reaction current density, and the surface area of the entity k. Given that $E_{oc,Cu} > E_{oc,\gamma} > E_{oc,\theta} > E_{oc,Al}$, the E^* value should range between $E_{oc,Al}$ and $E_{oc,Cu}$. If $E^* > E_{oc,Cu}$, all the entities undergo anodic polarization, $i_{a,k}$ is always larger than $i_{c,k}$. The

equation cannot be balanced. If $E^* < E_{oc,Al}$, all the entities undergo cathodic polarization, $i_{a,k}$ is always smaller than $i_{c,k}$. The equation cannot be balanced either. The E^* value depends on the area ratio among the four entities. In a Cu-Al bond joint, Cu has a much higher surface area than the other entities. Therefore, $i_{a,Cu}A_{Cu}$ is significantly larger than the other items on the left side of the equation. Similarly, $i_{c,Cu}A_{Cu}$ is significantly larger than the values of the other items on the right side of the equation. Equation (1) can be simplified into the following form:

$$i_{a,Cu}A_{Cu} \approx i_{c,Cu}A_{Cu} \qquad (2)$$

Therefore,

$$i_{a,Cu} \approx i_{c,Cu} \qquad (3)$$

This implies that Cu doesn't undergo significant galvanic polarization. Instead, it corrodes nearly under open circuit condition. Since γ, θ, and Al all corrode at the same potential with Cu, the E^* value should be close to $E_{oc,Cu}$. Assuming $E^* = E_{oc,Cu}$, $i_{a,k}$ at $E_{oc,\,Cu}$ should represent the actual corrosion rate of the entity k in this Cu-γ-θ-Al four-metal galvanic system. The $i_{a,Cu}$ and $i_{a,\gamma}$ values were obtained by extrapolating the linear regimes of their anodic polarization curves back to $E_{oc,Cu}$ as shown in Fig. 4.3 [91]. The $i_{a,\theta}$ and $i_{a,Al}$ values were obtained directly from their anodic polarization curves [91]. Since $E_{oc,Cu}$ was much higher than $E_{oc,\theta}$ and $E_{oc,Al}$, the current densities at $E_{oc,Cu}$ were purely from the anodic dissolution reactions for both θ and Al. Obviously, the $i_{a,Al}$ and $i_{a,\theta}$ values are much higher than the $i_{a,Cu}$ and $i_{a,\gamma}$ values. The bond failure should be caused by the dissolution of θ and Al, instead of γ.

In fact, the extrapolated linear regimes of Cu and γ are always far to the left of the entire anodic polarization curves of θ and Al in Fig 4.3. This means the $i_{a,Al}$ and $i_{a,\theta}$ values are higher than the $i_{a,Cu}$ and $i_{a,\gamma}$ values at any E^* value varying between $E_{oc,Al}$ and $E_{oc,Cu}$. Therefore, Al and

θ should always corrode faster than γ in a Cu-γ-θ-Al four-metal galvanic system regardless of the area ratio among them. This also fundamentally explains the mass loss experiment results.

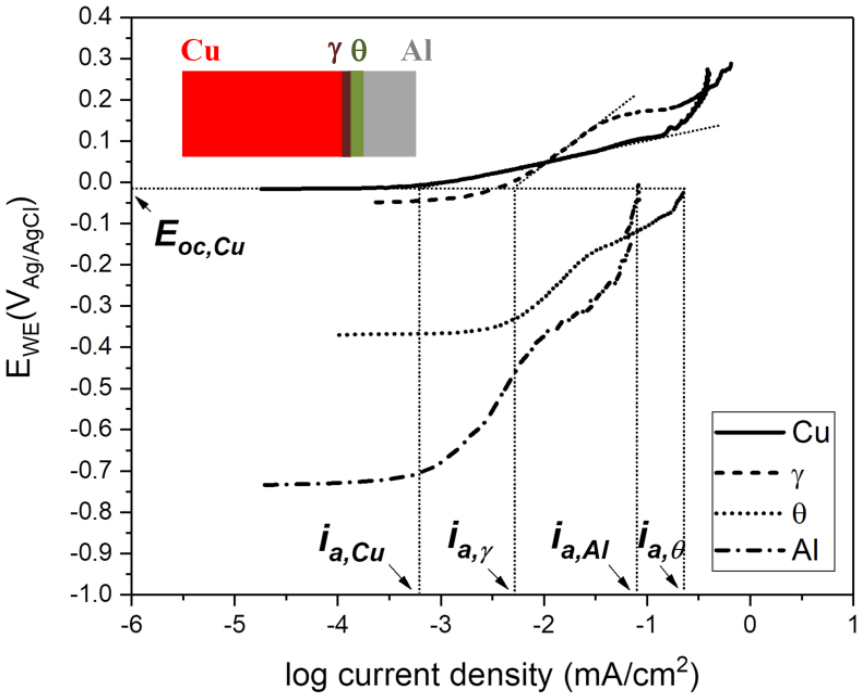

Figure 4.3 Evaluate the anodic dissolution current density i_a of Cu, γ, θ, and Al when they form a four-metal galvanic system. It was assumed that all the entities corroded at $E_{oc,Cu}$. Values of $i_{a,Cu}$ and $i_{a,\gamma}$ were obtained by the linear extrapolation, while values of $i_{a,\theta}$ and $i_{a,Al}$ were obtained directly from their anodic polarization curves

Due to the presence of potential defects, crack propagation along the interfaces between two adjacent entities might lead to the bond failure before θ and Al are completely consumed in this four-metal galvanic system. There are three different scenarios depending on the failed interface.

If the bond fails at the Cu-γ interface first, the Cu ball is detached from the Al pad and corrodes under the open circuit condition. γ, θ, and Al form a three-metal galvanic system. For the isolated Cu, the $i_{a,Cu}$ value was obtained by extrapolating the linear regime of its anodic polarization curve to $E_{oc,Cu}$. For the γ-θ-Al galvanic system, $E^*_{\gamma\text{-}\theta\text{-}Al} = E_{oc,Al}$ was assumed due to the much larger area of Al than those of γ and θ. The values of $i_{a,\gamma}$, $i_{a,\theta}$, and $i_{a,Al}$ were obtained by extrapolating the linear regimes of their anodic polarization curves to $E_{oc,Al}$. All the i_a values

were marked in Fig. 4.4. $i_{a,Al}$ turns out to be the highest. Therefore, if the bond fails at the Cu-γ interface first, Al pad should corrode faster than the other three entities.

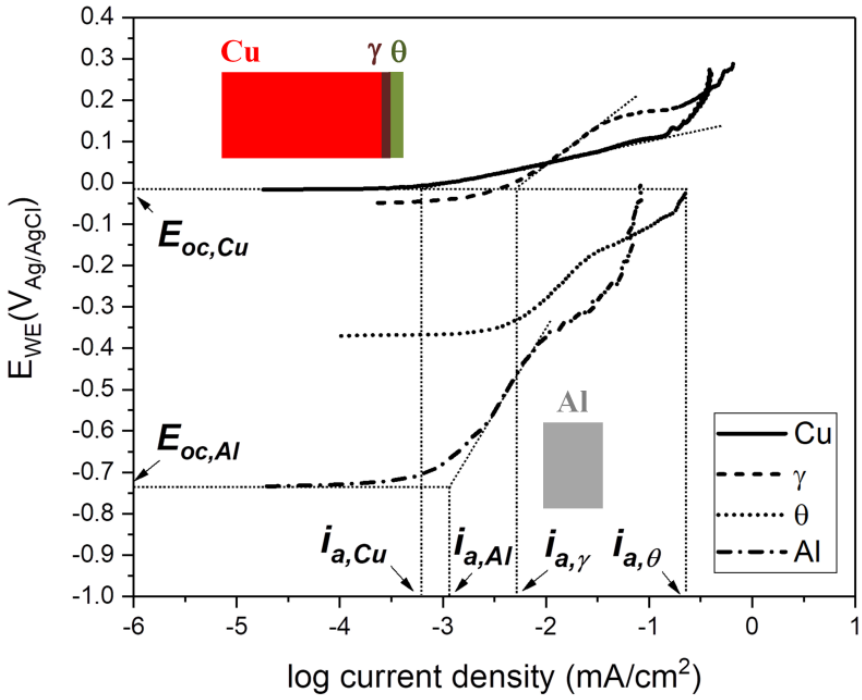

Figure 4.4 Anodic dissolution current density i_a of each entity after the crack at the Cu-γ interface separating Al from the other entities. $i_{a,Cu}$ was obtained by extrapolating the linear regime of its anodic polarization curve to $E_{oc,Cu}$. $i_{a,\gamma}$, $i_{a,\theta}$, and $i_{a,Al}$ was obtained by extrapolating linear regimes of their anodic polarization curves to $E_{oc,Al}$. $i_{a,Al}$ turns out to be the highest among all the entities.

If the bond fails at the γ-θ interface first, the Cu-γ-θ-Al galvanic system is then divided into two disconnected galvanic couples, Cu-γ and θ-Al. The i_a values for each entity under this scenario were evaluated using the similar extrapolation method as shown in Fig. 4.5. For the Cu-γ couple, $E^*_{Cu\text{-}\gamma} = E_{oc,Cu}$ was assumed due to a much larger surface area of Cu than γ, the $i_{a,Cu}$ and $i_{a,\gamma}$ values were obtained by extrapolating the linear regimes of their anodic polarization curves to $E_{oc,Cu}$. Similarity, for the θ-Al couple, $E^*_{\theta\text{-}Al} = E_{oc,Al}$ was assumed due to a much larger surface area of Al than θ, the values of $i_{a,\theta}$ and $i_{a,Al}$ were obtained by extrapolating the linear regimes of their anodic polarization curves to $E_{oc,Al}$. The $i_{a,\gamma}$ value was the highest among all the entities. Therefore, if the γ-θ interface is cracked open before θ and Al are completely consumed,

γ will corrode faster than θ and Al. This is consistent with the observed disappearance of γ in the humidity reliability tests.

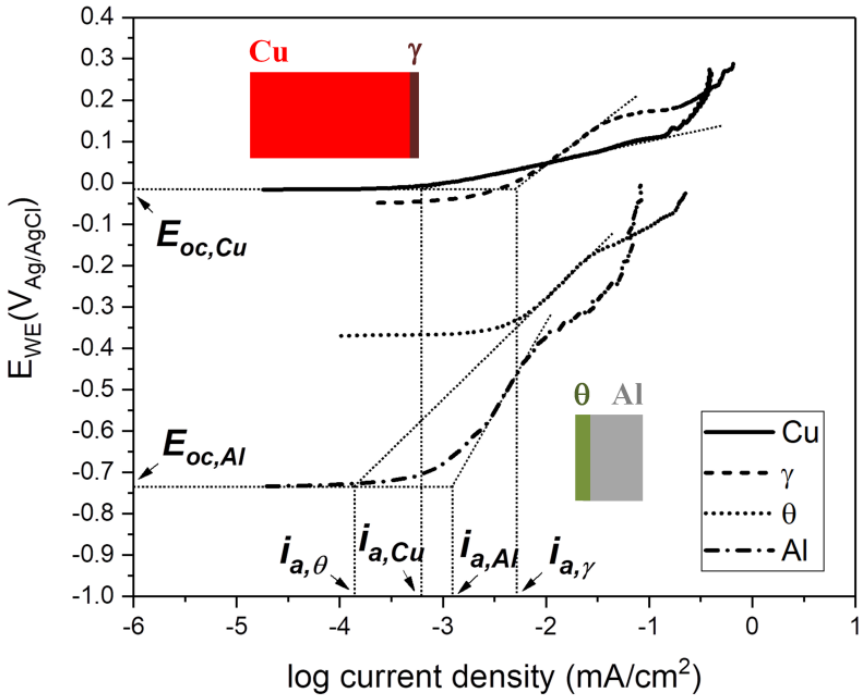

Figure 4.5 Anodic current density i_a of each entity after the crack propagates across the interface between γ and θ. $i_{a,Cu}$ and $i_{a,\gamma}$ were obtained by extrapolating the linear regimes of their anodic polarization curves to $E_{oc,Cu}$. $i_{a,\theta}$ and $i_{a,Al}$ was obtained by extrapolating the linear regimes of their anodic polarization curves to $E_{oc,Al}$. $i_{a,\gamma}$ turns out to be the highest among all the entities, which is consistent with the observed disappearance of γ.

If the bond fails at the θ-Al interface first, the Cu ball along with the two thin layers of IMCs are lifted off from the Al pad. Al pad corrodes under the self-corrosion condition, while Cu, γ, and θ form a separate three-metal galvanic system. For the isolated Al pad, the $i_{a,Al}$ value was obtained by extrapolating the linear regime of its anodic polarization curve to $E_{oc,Al}$. For the Cu-γ-θ galvanic system, $E^*_{Cu\text{-}\gamma\text{-}\theta} = E_{oc,Cu}$ was assumed due to a much larger area of Cu than those of γ and θ. The values of $i_{a,Cu}$, $i_{a,\gamma}$, and $i_{a,\theta}$ were obtained by extrapolating the linear regimes of their anodic polarization curves to $E_{oc,Cu}$ as seen in Fig 4.6. $i_{a,\theta}$ turns out to be the highest. Therefore, if the bond fails between θ and Al, θ corrodes faster than the other three entities.

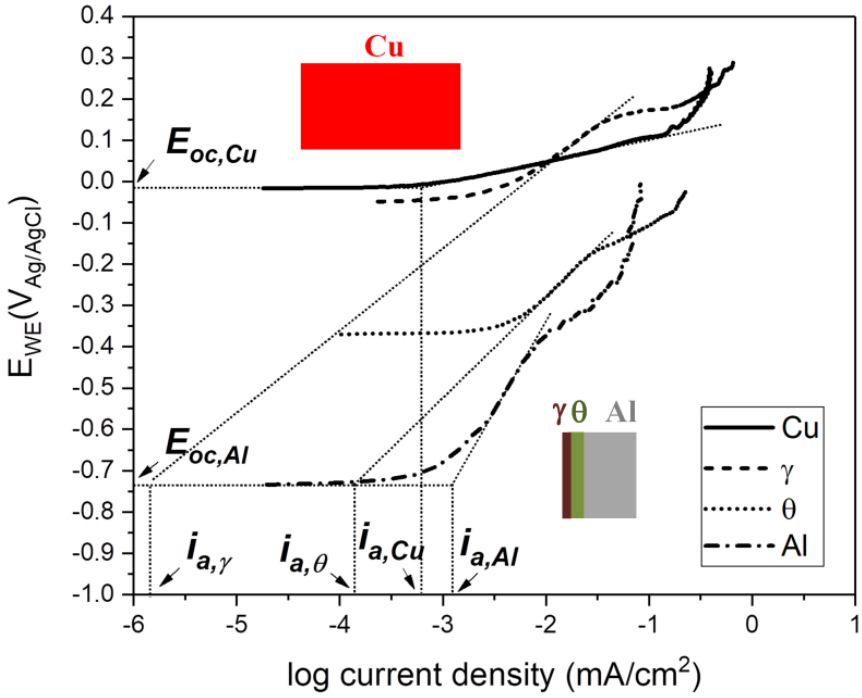

Figure 4.6 Anodic current density i_a of each entity after the crack propagates across the interface between θ and Al. $i_{a,Cu}$ and $i_{a,\gamma}$ were obtained by extrapolating the linear regimes of their anodic polarization curves to $E_{oc,Cu}$. $i_{a,\theta}$ was directly obtained from its anodic polarization curve. $i_{a,Al}$ was obtained by extrapolating the linear regime of its anodic polarization curve to $E_{oc,Al}$. $i_{a,\theta}$ turns out to be the highest among all the entities.

In summary, only scenario 2 aligns with the experimental observation that γ disappears from the bonding interface first. The crack should propagate through the γ-θ interface and lead to the bond failure before the θ and Al layers are completely consumed. After Cu and γ are electrically isolated from θ and Al, γ the anode corrodes in the Cu-γ couple with a significantly large cathode-to-anode ratio. Al the anode corrodes in the θ-Al couple with a much smaller cathode-to-anode ratio. γ undergoes a much higher anodic polarization than Al due to a more significant galvanic effect. Therefore, γ appears to corrode faster from the bond interface. The high crack propagation rate at the γ-θ interface can be attributed to both metallurgical and electrochemical factors.

4.2.3 Crack Propagation between γ and θ: Galvanic Corrosion under Ohmic Control

Unlike full immersion, galvanic corrosion for the encapsulated ball-bond interface proceeds in a thin layer of liquid electrolyte at the mold-bond interface. This thin electrolyte layer comes from the moisture absorption and diffusion in the molding compound as described in [20,33]. The electrolyte resistance, also referred to as the ohmic resistance, plays a significant role in the galvanic corrosion behavior between dissimilar entities [34]. G. L. Song [92] studied the potential distribution of a multi-metal galvanic system in a thin-layer electrolyte. The numerical analysis shows if the galvanic corrosion between two adjacent metals was under ohmic control, the two metals experienced galvanic polarization at the interface, however, remained unpolarized away from the interface. Namely, the galvanic effect is constrained only at the interface between two adjacent entities. Hence, the four-metal sandwich structure of the bond interface should be treated as three independent two-metal galvanic couples: Cu-γ, γ-θ, and θ-Al. The corrosion rates of these three interfaces were evaluated by measuring the galvanic current, i_g, of the three galvanic couples using ZRA as described in the ASTM G71-81 standard [70]. Values of $i_{g,Cu\text{-}\gamma}$, $i_{g,\gamma\text{-}\theta}$, and $i_{g,\theta\text{-}Al}$ were plotted versus the immersion time in Fig. 4.7.

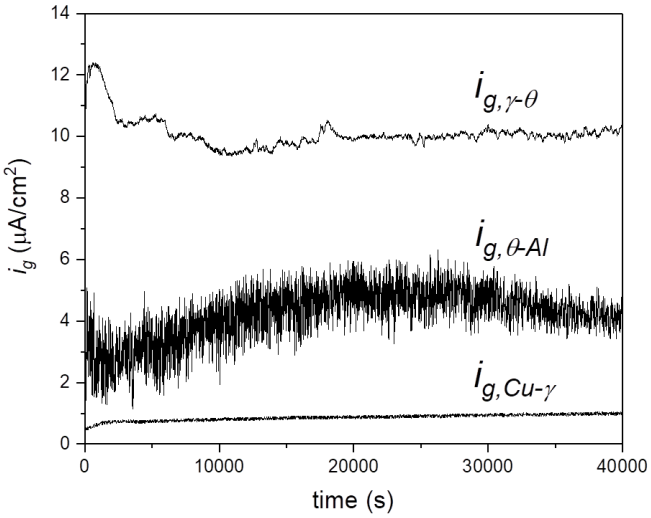

Figure 4.7 Values of $i_{g,Cu\text{-}\gamma}$, $i_{g,\gamma\text{-}\theta}$, and $i_{g,\theta\text{-}Al}$ as a function of the immersion time in a near neutral 20ppm NaCl solution

The i_g values were found to be stabilized after around 12 hours. Values of $i_{g,Cu\text{-}\gamma}$, $i_{g,\gamma\text{-}\theta}$, and $i_{g,\theta\text{-}Al}$ are all positive, which indicates γ was the anode for the Cu-γ couple, θ was the anode for the γ-θ couple, and Al was the anode for the θ-Al couple. The stabilized $i_{g,\gamma\text{-}\theta}$ value, ~10.4 μA/cm^2, is higher than the stabilized $i_{g,\theta\text{-}Al}$ value, ~3.8 μA/cm^2 and the stabilized $i_{g,Cu\text{-}\gamma}$ value, ~1.1 μA/cm^2. Results of the mass loss experiment after five weeks of immersion in a 20ppm NaCl solution for these three two-metal couples were tabulated and shown in Table 4.2.

Table 4.2. Fractional mass loss of each entity after five weeks of immersion in a pH 6, 20ppm NaCl solution

galvanic couple	run No.	entity	mass before immersion (mg)*	mass after immersion (mg)*	mass loss (mg)	fractional mass loss[1] (%)
Cu-γ	1	Cu	572.17	572.69	-0.52	
		γ	497.49	493.44	4.05	0.81
	2	Cu	530.24	530.31	-0.07	
		γ	494.06	490.02	4.04	0.82
	3	Cu	517.65	517.60	0.05	
		γ	495.63	491.59	4.04	0.82
γ-θ	1	γ	495.72	494.87	0.85	
		θ	387.22	372.25	14.97	3.9
	2	γ	496.69	496.94	-0.25	
		θ	386.75	366.92	19.83	5.1
	3	γ	496.69	495.96	0.73	
		θ	386.75	362.72	24.03	6.2
θ-Al	1	θ	385.44	386.87	-1.43[2]	
		Al	426.73	419.35	7.38	1.7
	2	θ	386.69	388.53	-1.84[2]	
		Al	404.30	397.13	7.17	1.8
	3	θ	384.67	386.10	-1.43[2]	
		Al	447.05	437.49	9.56	2.1

The three groups for each couple were measured during the same period of time under the same experimental conditions.
*: measured with a Model 135-S METTLER TOLEDO analytical balance with a repeatability of 0.03 mg
[1]. Fractional mass loss = 100*[(mass before - mass after immersion) / mass before]
[2]. The negative mass loss might be attributed to the redeposition of Al^{3+} in the electrolyte in the form of aluminim on the surface.

In galvanic corrosion, the cathode is protected, and mass loss is expected to occur faster for the anode. From Table 2, mass loss was observed for the anode as predicated from the ZRA

experiment. Interestingly, mass loss ranking corresponds linearly to the values of the stabilized i_g, where a higher i_g value corresponds to a higher mass loss. This finding suggests the corrosion-induced crack should propagate the fastest at the γ-θ interface in an encapsulated package.

4.2.4 Crack Propagation between γ and θ: Residual Alumina and Stress Buildup

In addition to galvanic corrosion, a large area of alumina layer exists between γ and θ. This alumina layer, roughly 5-10 nm thick, originates from the aluminum pad before bonding [31]. Although being fragmented by the ultrasonic vibration, fragmented alumina patches remained at the bond interface with the θ IMC forming between them. Both Xu et al. [31] and Kim et al. [93] observed that this alumina layer further migrated to the interface between γ and θ as a γ layer started to grow out of the θ layer after thermal annealing at a high temperature (175 ℃) for an extended period of time (>25 h). Lee et al. [58] estimated that more than 50% of the bond area was covered by the alumina based on the microscopic images of the ball bond interface after 300 h of annealing at 175℃. The weak bonding between the alumina and the IMCs makes it easier for the electrolyte to seep in and accelerate the crack propagation between γ and θ. This was also used by Lee et al. [58] to explain the observed higher number of detached Cu wire bonds than that of Au wire bonds after 30 mins of full immersion in a dilute NaCl electrolyte. The alumina coverage of Au wire bonds was found to be less than 30%, which was smaller than the 50% alumina coverage observed in the Cu wire bonds. Although the electromotive force difference between Cu and Al is much smaller than that between Au and Al, the larger area of alumina in the Cu wire bonds made the bond interface more susceptible to the electrolyte attack and resulted in a higher failure rate in the immersion test [58]. In addition, multiple voids, which were tens of nanometers in diameter between γ and θ, were observed by Xu et al. [31] and Kim et al. [93] after annealing at 250 ℃ for 25 h and 175 ℃ for 500 h, respectively. As θ transitions to γ during

the annealing, a significant amount of internal stress starts to build up at the γ-θ interface due to a volumetric shrinkage of ~4.3% as reported in [31]. Near the area occupied by alumina, the bond between γ and θ is weak. The internal stress build-up causes voids to form near this area [31]. These voids between γ and θ, although sparsely-distributed and small-sized, might also play a role in accelerating the corrosion-induced crack propagation between the two IMCs.

4.2.5 Corrosion Mechanism of an Encapsulated Cu Ball Bond Interface

Based on the previous discussion, the corrosion mechanism of an encapsulated Cu-Al ball bond is shown in Fig. 4.8. Initially, cracks propagate along three interfaces between Cu and γ, γ and θ, θ and Al independently due to the ohmic control condition (Step 1). The crack grows much faster along the γ-θ interface due to the highest i_g value (Step 2). The weak bonding due to the presence of residual alumina and the accumulated internal stress might further facilitate the crack growth between γ and θ. The crack eventually penetrates through the entire bond area and results in the ball-pad detachment (Step 3). The bond failure leads to the formation of two separate galvanic couples: Cu-γ and θ-Al. The γ loses the galvanic protection provided by the less noble θ and Al. Moreover, it suffers significant anodic dissolution due to the galvanic effect imposed from an infinitely large area of Cu. The overall result is that γ ends up corroding faster than all other entities present and disappears from the encapsulated bond interface (Step 4).

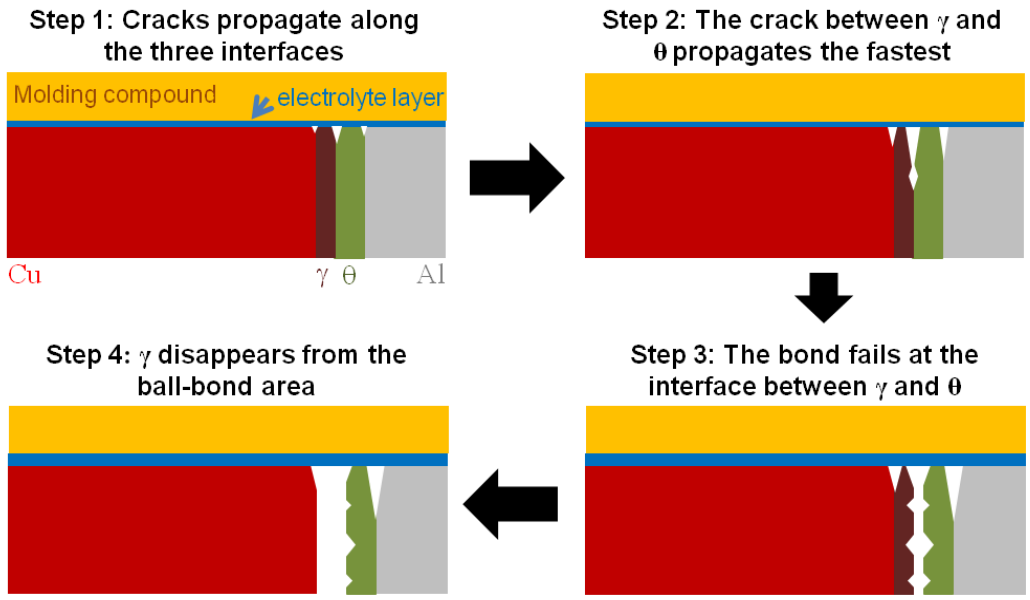

Figure 4.8 Corrosion behavior of an encapsulated Cu-Al ball bond interface. Step 1: cracks preferentially propagate along the interface between two adjacent entities due to the ohmic control. Step 2: the crack propagates much faster along the interface between γ and θ due to a higher i_g value. Step 3: As the metal erodes away and dissolves in the electrolyte, the ohmic effect is weakened. However, the crack continues propagating fast between γ and θ until bond failure due to the high anodic polarization imposed on θ and interfacial defects between them. Step 4: γ disappears due to the galvanic effect imposed by a large area of the cathode Cu.

4.3 Conclusions

Galvanic corrosion of an encapsulated ball bond interface occurs in a thin layer of electrolyte at the mold-bond interface. The ohmic resistance of this electrolyte is high due to a narrow ion conducting path. Thus, it is reasonable to assume that the galvanic corrosion is constrained only between adjacent entities. The corrosion rate between γ and θ was found to be the highest as compared to the galvanic corrosion rate between Cu and γ and the galvanic corrosion rate between θ and Al. Additionally, the residual alumina between γ and θ and the stress buildup associated with the θ-to-γ transformation accelerate the crack propagation rate between them. Hence, the bond failure happens at the γ-θ interface first. This failure results in the formation of two separate galvanic couples: Cu-γ and θ-Al. For the Cu-γ couple, the corrosion rate of γ is significantly accelerated by the strong galvanic effect imposed by a large area of Cu. For the θ-

Al couple, the corrosion rate of Al is not greatly accelerated due to a small area of θ. Both Cu and θ are cathodically protected in their respective galvanic couples. Hence, the γ appears to be preferentially attacked. If the Cu-Al bonding interface is fully annealed to consist of only Cu and γ, the galvanic corrosion rate should be lower based on a lower i_g value and mass loss between the two entities.

CHAPTER 5 PALLADIUM AND CHLORIDE EFFECT ON THE BOND FAILURE MECHANISM AND RATE

5.1 Introduction

Currently, using Pd-coated Cu wire and green molding compound are two most common corrosion-mitigating strategies [23]. However, the mitigating mechanisms of Pd addition and low chloride concentration have not been fully understood. Based on the discussion in Chapter 4, the bond failure is due to the crack penetration along the interface between γ and θ. The crack propagation between γ and θ can be attributed to various electrochemical and mechanical reasons such as the high localized galvanic corrosion, the presence of a large area of fragmented alumina, and the stress buildup up during the IMC transformation at the γ-θ interface. Effect of Pd and chloride concentration on the bond corrosion mechanism and corrosion rate can be understood based on how they affect the occurrence of these events that lead to the bond failure.

5.2 Results and Discussions

5.2.1 Chloride Effect on the i_g Values

Based on the discussion from chapter 4, the galvanic corrosion of an encapsulated ball-bond interface should be under ohmic control. Galvanic corrosion proceeds independently along the three interfaces between Cu and γ, γ and θ, and θ and Al. Therefore, to evaluate the chloride concentration effect on the bond corrosion behavior, the values of i_g(Cu:γ), i_g(γ:θ), and i_g(θ:Al) were measured in solutions with various chloride concentrations and plotted versus the immersion time as shown in Fig. 5.1a, 5.1b, and 5.1c, respectively. The i_g values remained positive throughout the measurement. This indicates that γ was the anode in the Cu-γ couple, θ was the anode in the γ-θ couple, and Al was the anode in the θ-Al couple regardless of the chloride concentration. The i_g values were stabilized after around 12 hours. The stabilized i_g

values were tabulated and shown in Table 5.1. The i_g(Cu:γ), i_g(γ:θ), and i_g(θ:Al) values all decreased systemically with a decreasing chloride concentration. The i_g(γ:θ) value was the highest in the 100ppm and 20ppm NaCl solutions. However, since the i_g(γ:θ) value decreased much faster than the i_g(θ:Al) value, the i_g(γ:θ) value became slightly lower than the i_g(θ:Al) value when the chloride concentration was lowered down to 1ppm.

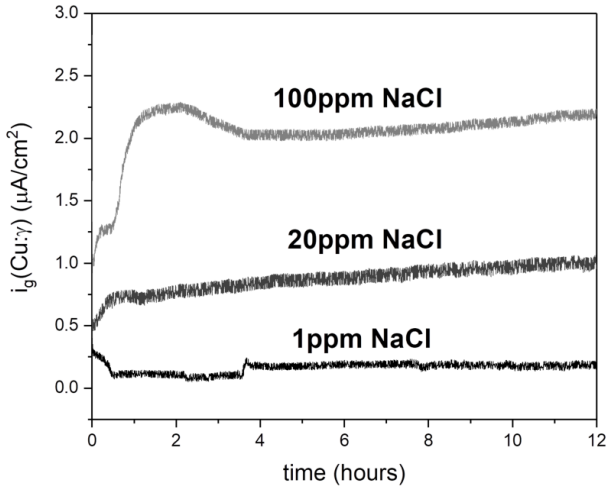

(a)

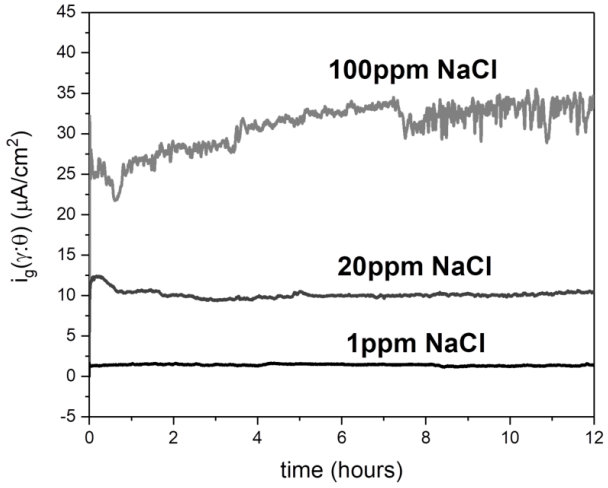

(b)

Figure 5.1 (a) values of i_g(Cu:γ), (b) values of i_g(γ:θ), (c) values of i_g(θ:Al) with the immersion time measured in solutions containing 100ppm, 20ppm, and 1ppm NaCl

Figure 5.1 (cont'd)

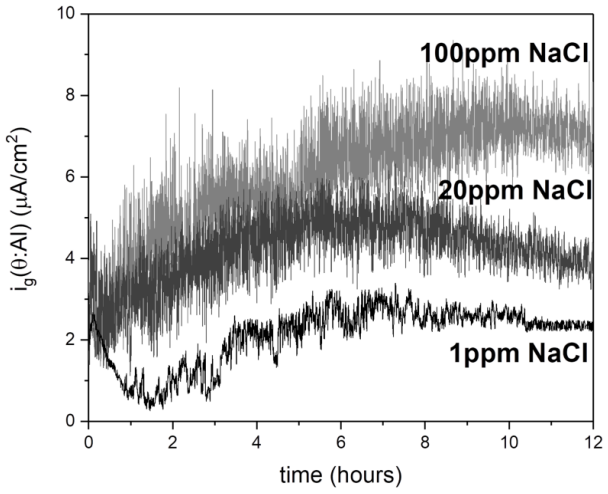

(c)

Table 5.1 The stabilized values of i_g at 12 hour-point in solutions containing different chloride concentrations

[Cl] (ppm)	i_g(Cu:γ) (μA/cm^2)	i_g(γ:θ) (μA/cm^2)	i_g(θ:Al) (μA/cm^2)
100	1.786±0.123	31.14±1.041	6.317±0.790
20	1.062±0.153	10.41±1.124	3.776±0.332
1	0.201±0.030	1.373±0.228	2.290±0.513

The chloride concentration effect on the i_g value can be understood using the mixed potential plot, which is commonly constructed by plotting the anodic polarization curve of the anode and the cathodic polarization curves of the cathode together [34]. Since varying the chloride concentration affected the i_g(γ:θ) value to a much higher degree, the mixed potential plot for the γ-θ couple was constructed and presented in Fig. 5.2 as an example.

The mixed potential theory treats the γ-θ couple as an isolating corroding system [34]. Based on this theory, there is no potential gradient along the electrically conductive γ-θ surface. Therefore, both γ and θ corrode at the same potential, denoted as E_{couple}. Additionally, there is no net charge accumulation for the γ-θ couple. Therefore, the net current of γ and the net current of θ are equal in value and both equal to the galvanic current measured via ZRA. Since γ and θ have

the same surface area, the current density of γ and θ are equal and denoted as i_{couple}. Thus, the following equation is always valid:

$$i_g = i_{couple} \qquad (1)$$

The i_{couple} value can be obtained from the crossover of the anodic polarization curve of θ and the cathodic polarization curve of γ as marked in Fig. 5.2 [34]. Based on the equation (1), chloride effect on i_g(γ:θ) can be explained from how the chloride affects the anodic polarization behavior of θ and the cathodic polarization behavior of γ.

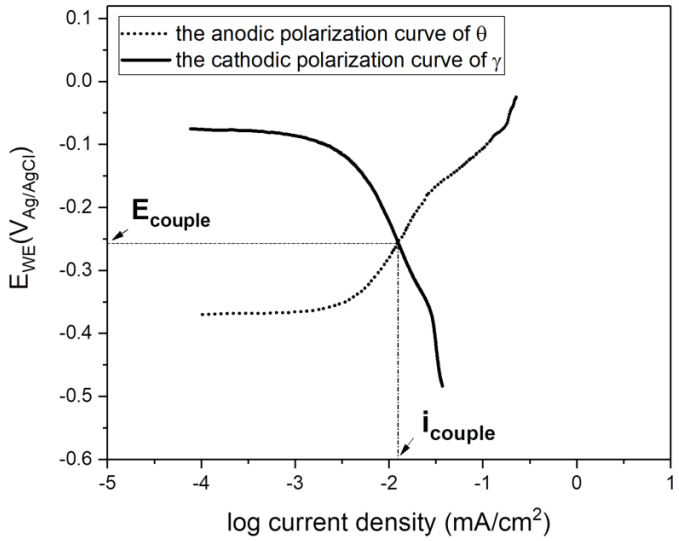

Figure 5.2 The mixed potential plot for the γ-θ galvanic couple in a near neutral 20 ppm NaCl solution. The current density at the crossover, i_{couple} equals the galvanic current density, i_g(γ:θ) measured via ZRA based on the mixed potential theory.

The anodic polarization curves of θ and the cathodic polarization curves of γ measured in 100ppm, 20ppm, and 1ppm NaCl solutions are plotted together in Fig. 5.3. The cathodic current density of γ was not affected by the chloride concentration since chloride was not involved in the cathodic reaction mechanism. Meanwhile, the anodic current density of θ decreased systemically with a decreasing chloride concentration due to a more protective surface passive film on its surface under a lower chloride concentration. As shown in Fig. 5.3, the decrease in the anodic

current density of θ led to a decrease in the i_{couple} value. Therefore, the decrease in the i_g(γ:θ) value from the ZRA measurement was due to the decrease in the anodic current density of θ with a decreasing chloride concentration. A similar rationale can also be used to explain the chloride effect on the i_g(Cu:γ) and i_g(θ:Al) values.

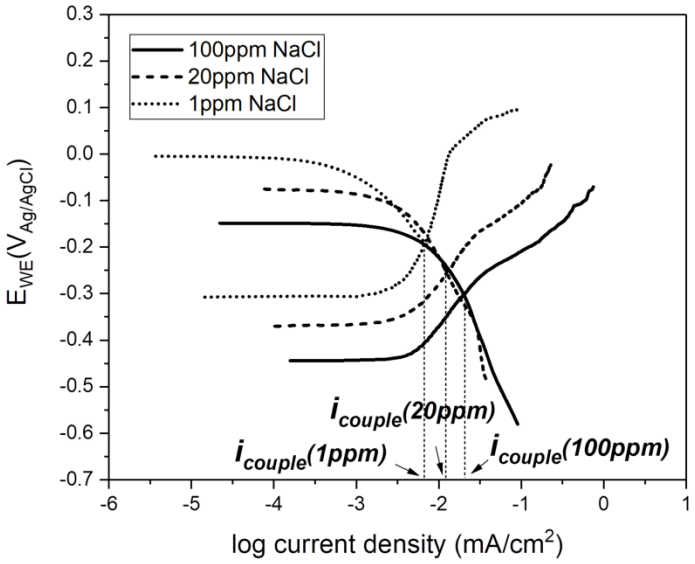

Figure 5.3 Values of i_{couple} obtained from the crossovers of the anodic polarization curves of θ and the cathodic polarization curves of γ measured in 100ppm, 20ppm, and 1ppm NaCl solutions of pH 6. The i_{couple} value decreased with a decreasing chloride concentration due to the decrease in the anodic current density of θ. This explains why i_g(γ:θ) decreased with a decreasing chloride concentration in the ZRA measurement.

5.2.2 Chloride Effect on the Bond Failure Mechanism and Failure Rate

As the chloride concentration decreased, the i_g(γ:θ) value decreased. This should reduce the crack growth rate at the γ-θ interface. Notably, as the chloride concentration decreased from 20ppm to 1ppm, the i_g(θ:Al) value became higher than the i_g(γ:θ) value. However, this does not necessarily mean that the bond failure should happen at the θ-Al interface. In a 1ppm NaCl solution, all the i_g values were much lower than those in 100ppm and 20ppm NaCl solutions. In such case, galvanic corrosion might not be a critical driving force of the crack propagation. Metallurgical factors such as the presence of the residual alumina and the internal stress buildup

associated with the IMC growth might dominate the crack propagation rate instead [20]. Overall, the bond failure rate can be reduced effectively by reducing the chloride level in the molding compound.

The bond failure behavior under different chloride concentrations can be examined using the similar polarization analysis introduced in chapter 4. The anodic polarization curves of Cu, γ, θ, and Al measured in a 100ppm NaCl solution are plotted in Fig. 5.4.

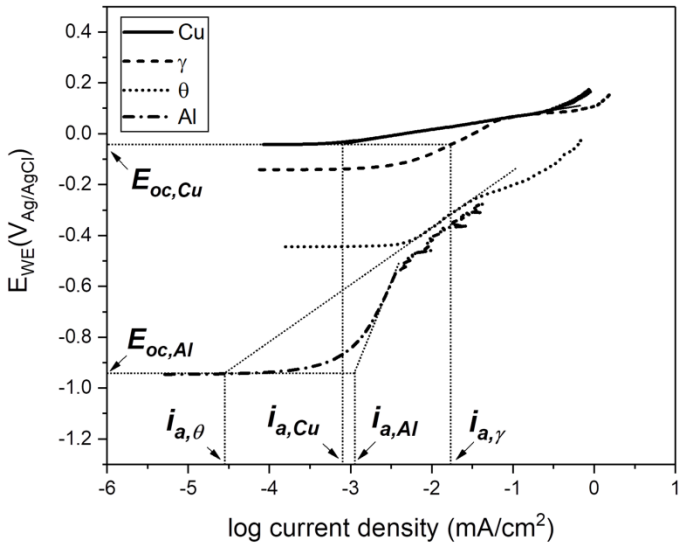

Figure 5.4 Anodic polarization curves of Cu, γ, θ, and Al measured in a 100ppm NaCl solution. The i_a values of all entities were obtained by linear extrapolation methods and marked in the figure.

The anodic dissolution rates of all the entities after the bond failure were evaluated using the linear extrapolation method on their anodic polarization curves. The bond failure at the γ-θ interface leads to the formation of two separate galvanic couples: Cu-γ and θ-Al. For the Cu-γ couple, both Cu and γ corrode at $E_{oc,Cu}$ due to a much larger area of Cu than γ. Therefore, $i_{a,Cu}$ and $i_{a,\gamma}$ values were obtained by extrapolating the linear regimes of their anodic polarization curves to $E_{oc,Cu}$. For the θ-Al couple, both θ and Al corrode at $E_{oc,Al}$ due to a much larger area of Al than θ. Therefore, $i_{a,Al}$ and $i_{a,\theta}$ values were obtained by extrapolating the linear regimes of

their anodic polarization curves to $E_{oc,Al}$. The ranking of the anodic dissolution rate was given as $i_{a,\gamma} > i_{a,Al} > i_{a,Cu} > i_{a,\theta}$. This ranking also held true for the 20ppm NaCl solution as shown in Fig. 5.5. These results indicate that γ should disappear from the ball-bond interface as a result of the bond failure at the γ-θ interface under higher chloride concentrations.

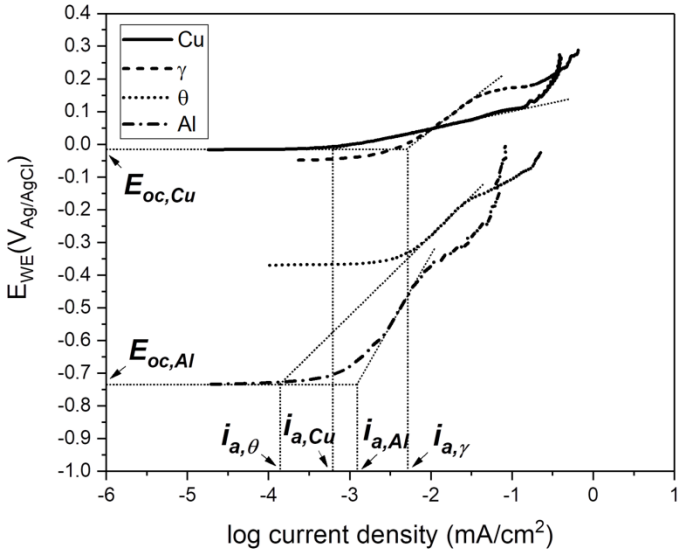

Figure 5.5 Anodic polarization curves of Cu, γ, θ, and Al measured in a 20ppm NaCl solution. The i_a values of all entities were obtained by linear extrapolation methods and marked in the figure.

In a 1ppm NaCl solution, the i_a values of all entities were obtained and shown in Fig. 5.6. The $i_{a,\gamma}$ and $i_{a,\theta}$ values were close, both of which were much higher than the $i_{a,Al}$ and $i_{a,Cu}$ values. Thus, both γ and θ might disappear as a result of the bond failure in an extremely dilute solution.

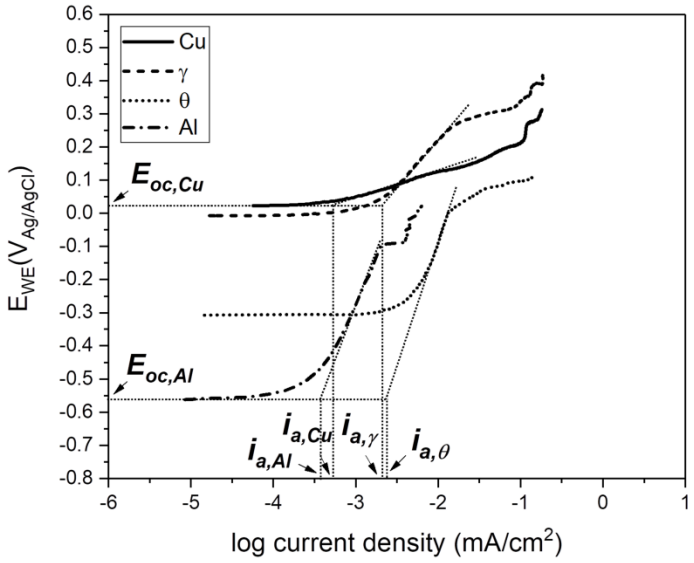

Figure 5.6 Anodic polarization curves of Cu, γ, θ, and Al measured in a 1ppm NaCl solution. The i_a values of all entities were obtained by linear extrapolation methods and marked in the figure.

5.2.3 Pd Effect on the i_g Values

Since Pd is only soluble in Cu and γ, only i_g(Cu:γ) and i_g(γ:θ) are affected. Pd concentrations in Cu and γ were measured and reported in several studies [22,40,45]. However, discrepancies in these results remain due to the different bonding parameters and the subsequent annealing conditions. In this study, Pd is assumed to be equally dissolved in Cu and γ. The values of i_g(CuPd:Pd-doped γ) and the i_g(Pd-doped γ:θ) with 2 wt.% Pd and 9 wt.% Pd addition were measured in a 20ppm NaCl solution and plotted versus the immersion time as shown in Fig. 5.7a and 5.7b, respectively. The i_g values remained positive throughout the measurement. This indicates that γ was the anode in the Cu-γ couple and θ was the anode in the γ-θ couple regardless of the Pd addition. The i_g values were stabilized after around 12 hours. The stabilized i_g values were tabulated and shown in Table 5.2. Pd addition decreased the i_g(Cu:γ) value and increased the i_g(γ:θ) value systemically.

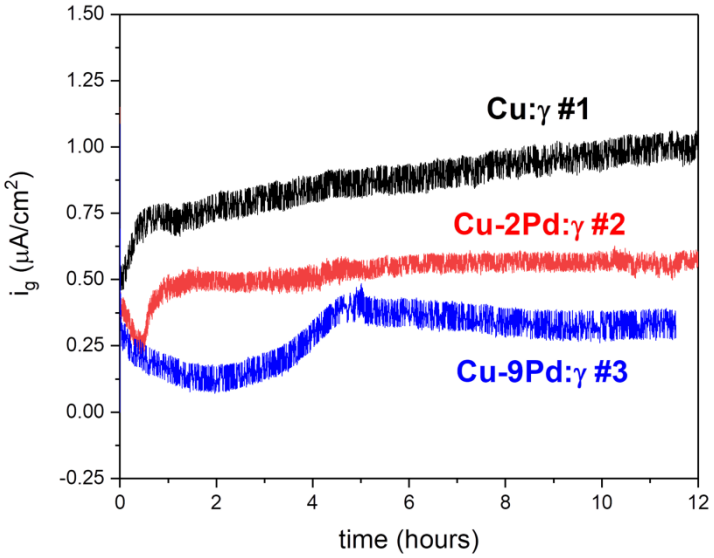

(a)

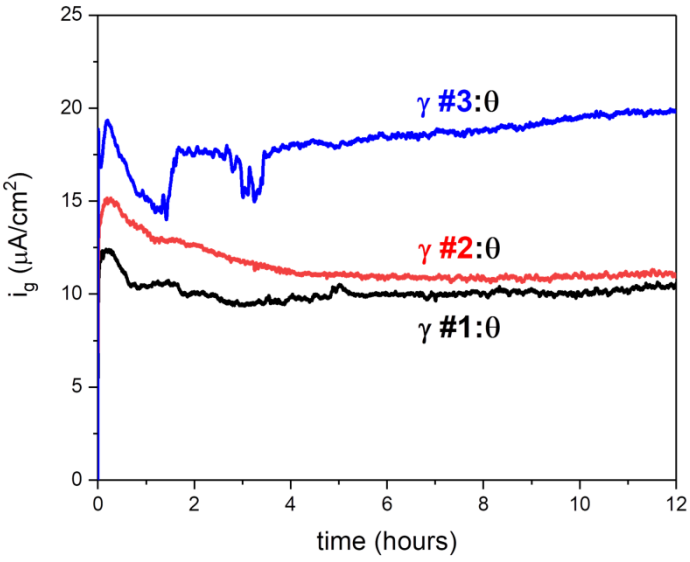

(b)

Figure 5.7 (a) values of i_g(CuPd:Pd-doped γ) and (b) values of i_g(Pd-doped γ:θ) measured in a 20ppm NaCl solution.

Table 5.2 Pd effect on the values of i_g(Cu:γ) and i_g(γ:θ) at 12-hour point in a near neutral 20ppm NaCl solution

WE	CE	i_g (μA/cm^2)
θ	γ #1	10.41±1.124
θ	γ #2	12.16±1.092
θ	γ #3	19.91±0.066
γ #1	Cu	1.062±0.153
γ #2	Cu-2Pd	0.580±0.091
γ #3	Cu-9Pd	0.441±0.052

The mixed potential plot for the γ-θ couple in Fig. 5.8 was used to understand the Pd effect on the i_g(γ:θ) value. The cathodic current density of γ increased with an increasing Pd addition due to the high catalytic activity of Pd to cathodic reactions [74]. The increasing cathodic current density of γ resulted in an increasing i_{couple} value. Therefore, the increase in the i_g(γ:θ) value with Pd addition was due to the increase in the cathodic current density of γ.

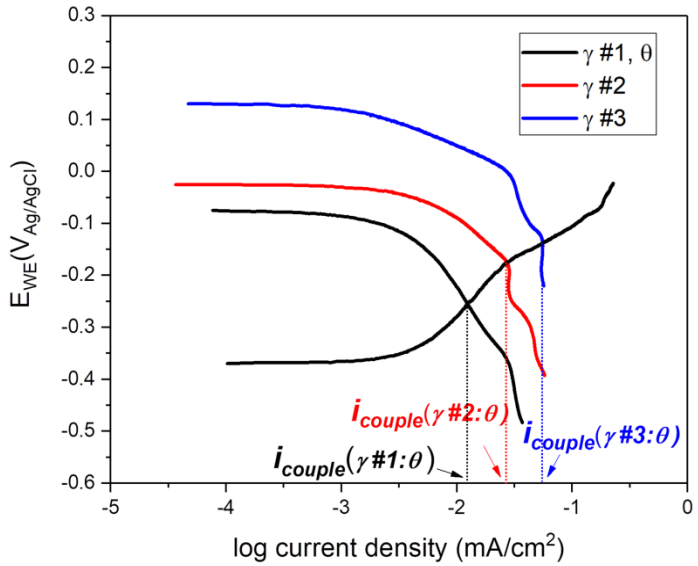

Figure 5.8 Values of i_{couple} obtained from the intercepts between the anodic polarization curves of θ and the cathodic polarization curves of γ #1, γ #2, and γ #3 measured in a near neutral 20ppm NaCl solutions. The i_{couple} value increased with an increasing Pd addition in γ due to the increase in the cathodic current density.

Unfortunately, the mixed potential plot for the Cu-γ couple could not be used to explain the Pd effect on the i_g(Cu:γ) value. As shown in Fig. 5.9, the i_{couple} value did not show a consistent decrease with an increasing Pd addition as the measured i_g values did.

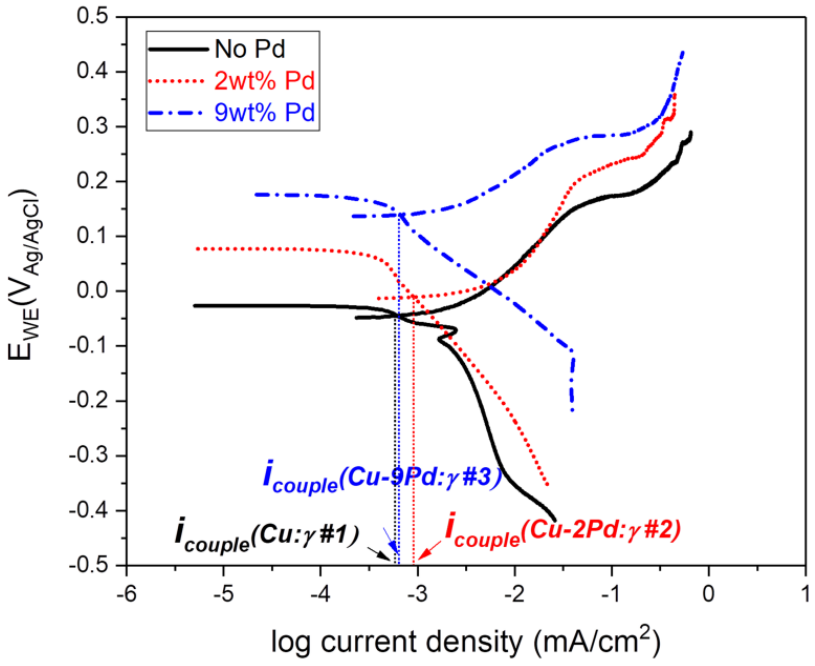

Figure 5.9 Values of i_{couple} obtained from the intercepts between the anodic polarization curves of Cu, Cu-2Pd, and Cu-9Pd and the cathodic polarization curves of γ #1, γ #2, and γ #3 measured in a near neutral 20ppm NaCl solutions. The i_{couple} values were marked in the figure. The i_{couple} value did not consistently decrease with Pd addition like the i_g value due to the overestimation of the cathodic current density of the Cu-Pd alloys

The deviation between i_g and i_{couple} should be due to the different surface conditions of the Cu-Pd alloys in the ZRA and polarization measurements. In the ZRA measurement, Cu-Pd alloys and Pd-doped γ IMCs were brought into contact and immersed in the electrolyte. They remained connected throughout the measurement. Although being exposed to the electrolyte, the Cu-Pd alloys as the cathode did not corrode due to the galvanic protection imposed by the γ IMCs. The cathodic polarization curves of the Cu-Pd alloys were measured after they were immersed in the electrolyte for an extended period of time. During this immersion period, Pd enriched at the surface as Cu was selectively leached out [79]. Thus, the cathodic polarization curve was measured on a corroded, Pd-enriched surface. Since the Pd-enriched surface has a higher catalytic activity to the cathodic reactions, the measured cathodic current density should be higher than an uncorroded surface. Therefore, in the mixed potential plot, the cathodic current

densities of Cu-Pd alloys were actually overestimated. This led to an overestimation of the i_{couple} value. Unfortunately, the pre-immersion period cannot be avoided since a stabilized E_{oc} is essential for obtaining a reproducible polarization curve. This further indicates i_{couple} cannot replace i_g as a quantitative measure of the galvanic corrosion rate.

5.2.4 Pd Effect on the Bond Failure Mechanism and Failure Rate

Pd effect on the bond failure rate should be understood from both the electrochemical and metallurgical perspectives. From the electrochemical perspective, Pd addition in Cu increases the $i_g(\gamma{:}\theta)$ value. This should increase the crack growth rate at the γ-θ interface. However, from the metallurgical perspective, the presence of Pd inhibits the Cu migration and therefore the resulting IMC growth and transformation [40,45,47]. As the θ-to-γ transformation slows down, the internal stress between γ and θ is lower. Lower stress leads to less void formation and thus a lower crack propagation rate between γ and θ [22]. Pd effect on the bond failure rate should depend on these two competing factors. The fact that a CuPd-Al bonding interface exhibits lower failure rate in the humidity reliability tests implies that the metallurgical factor is the more dominant.

Pd effect on the bond corrosion mechanism was investigated using the similar polarization analysis. For 2 wt.% Pd addition, the bond failure at the γ-θ interface results in the formation of two separated galvanic couples: (Cu-2Pd)-γ #2 and θ-Al. For the (Cu-2Pd)-γ #2 couple, the $i_{a,Cu\text{-}2Pd}$ and $i_{a,\gamma\ \#2}$ values were obtained by extrapolating the linear regions of their anodic polarization curves back to $E_{oc,Cu\text{-}2Pd}$ as shown in Fig 5.10a. For the θ-Al galvanic couple. the $i_{a,\theta}$ and $i_{a,Al}$ values were obtained by extrapolating the linear regions of their anodic polarization curves back to $E_{oc,Al}$. The ranking of the i_a values is given as $i_{a,\theta} < i_{a,Cu\text{-}2Pd} < i_{a,Al} < i_{a,\gamma\ \#2}$. For 9 wt.% Pd addition, the ranking of the i_a values was obtained using the similar extrapolation methods as

shown in Fig. 5.10b and given as $i_{a,\theta} < i_{a,Cu\text{-}9Pd} < i_{a,Al} < i_{a,\gamma\ \#3}$. Therefore, γ should corrode faster than the other three entities regardless of the amount of Pd addition. This is consistent with the experimental observation in the humidity-related reliability tests that γ disappeared when a CuPd wire was used for bonding [23].

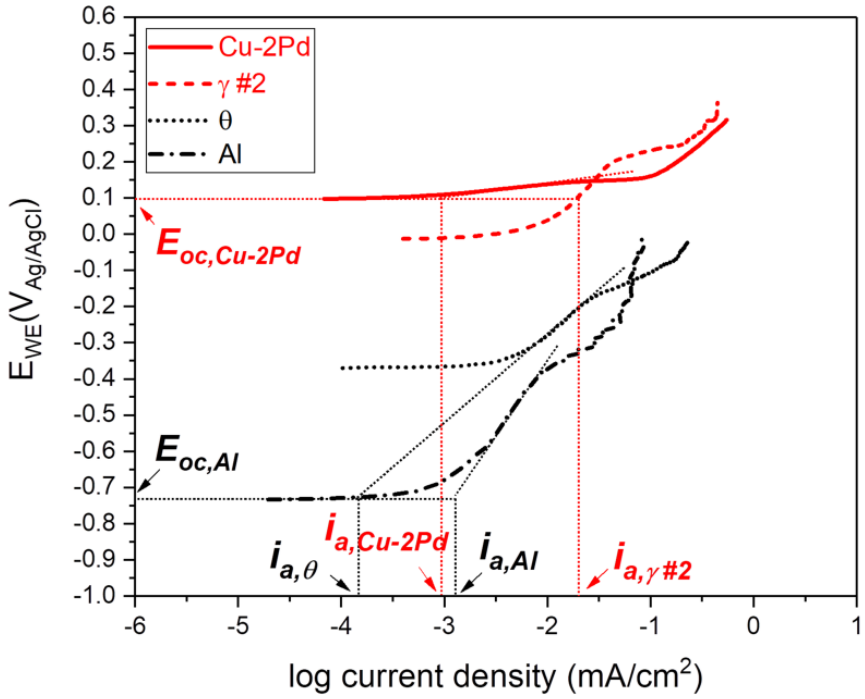

(a)

Figure 5.10 (a) Anodic polarization curves of Cu-2Pd, γ #2, θ, and Al, (b) Anodic polarization curves of Cu-9Pd, γ #3, θ, and Al. All the polarization curves were measured in a 20ppm NaCl solution. The i_a values of all entities were obtained by linear extrapolation methods and marked in the figure.

Figure 5.10 (cont'd)

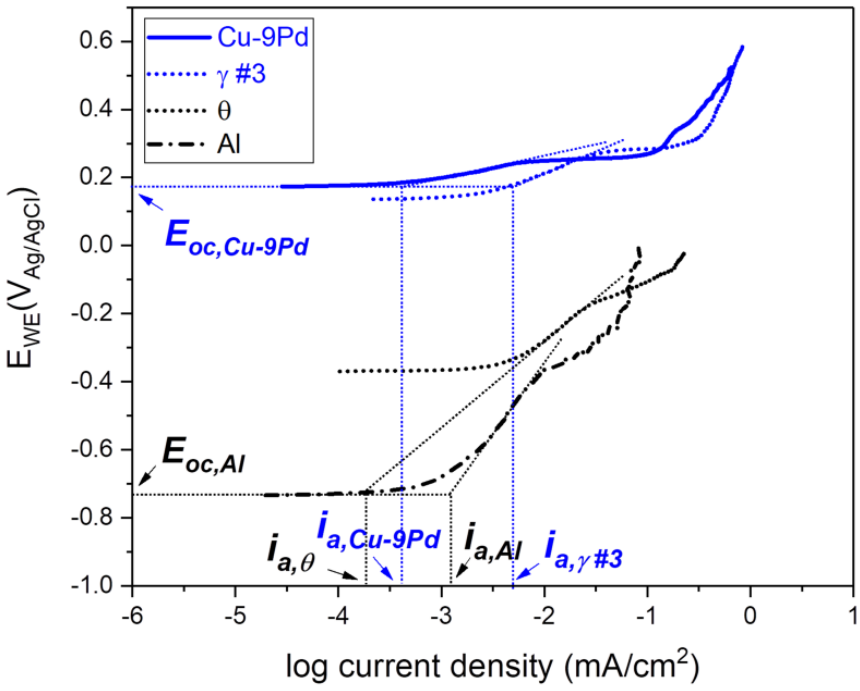

(b)

5.2.5 i_g(CuPd:Pd-doped γ) at Low Chloride Concentration and High Pd Addition

As shown in Table 5.2 and 5.3, increasing Pd addition and reducing chloride concentration can both lower the i_g(Cu:γ) value. The synergistic effect of the Pd and chloride concentration was studied by measuring i_g(Cu-9Pd:γ #3) in an near neutral electrolyte containing only 1ppm of NaCl. The i_g(Cu-9Pd:γ #3) value approached zero and became negative with an increasing immersion time as shown in Fig. 5.11. This indicates that the galvanic effect between γ and Cu was minimized or even reversed as the Pd addition was increased, and the chloride concentration was reduced simultaneously. This provides a new metallurgical approach to mitigate the bond corrosion. Due to the unlimited supply of Cu from the ball side, Al-rich entities such as θ and Al can be completely consumed and converted to γ through the annealing process [31]. In such case, the bond interface consists of Cu and γ only. The wire metallurgy, like the Pd addition, and the

molding compound chemistry, like the chloride concentration, can be tuned such that the Pd enrichment in both Cu and γ leads to the immunity of the bond interface to the galvanic corrosion attack. The bond failure rate can thus be significantly reduced.

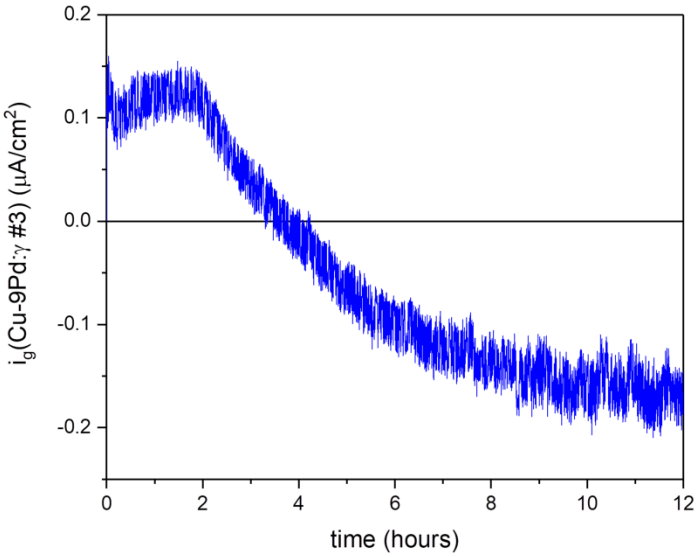

Figure 5.11 the value of i_g(Cu-9Pd:γ#3) as a function of the immersion time in a 1ppm NaCl solution

5.3 Conclusions

Both chloride concentration and Pd addition did not change the ball-bond corrosion behavior in terms of the initial failure at the γ-θ interface and the subsequent disappearance of γ. However, chloride concentration and Pd addition affected the bond failure rate in different ways. Lower chloride concentration led to a lower i_g(γ:θ) value. Thus, using chloride-free molding compound should be effective in reducing the bond failure rate. Pd in γ increased the i_g(γ:θ) value. However, Pd is also known to inhibit the IMC growth and the associated internal stress buildup. The latter factor should be more significant since Pd has been consistently found to improve the bond lifetime in humidity reliability tests. The galvanic corrosion effect between Cu and γ can be eliminated by simultaneously reducing the chloride concentration and increasing the Pd addition. This indicates that annealing and transforming the original four-metal bond interface to a two-

metal interface consisting only the Pd-enriched Cu and Pd-enriched γ can be an effective method to mitigate the bond corrosion rate.

CHAPTER 6 SUMMARY AND RECOMMENDATIONS

6.1 Summary

In chapter 3, key self-corrosion parameters such as E_{oc} and i_{corr} of Cu, γ, θ, and Al were evaluated as a function of Pd addition, chloride concentration, pH, and temperature. Based on the E_{oc} values, the nobility ranking is given as Cu > γ > θ > Al. From a galvanic corrosion point of view, this nobility ranking indicates that the Al-rich entities θ and Al should act as the anodes and corrode faster, while the Cu-rich entities γ and Cu should act as the cathodes and corrode slower in a four-metal galvanic system Cu-γ-θ-Al. Based on the i_{corr} value, the self-corrosion rate of γ was not significantly higher than those of θ and Al. The galvanic effect should be dominant enough to cause a faster dissolution rate of θ and Al than γ. The higher corrosion rate of θ and Al in a Cu-γ-θ-Al galvanic system was confirmed in a four-metal mass loss measurement, where Cu, γ, θ, and Al ingots were brought into contact and immersed in a chloride-containing electrolyte, as detailed in chapter 4. These findings suggest that γ should not disappear in a Cu-γ-θ-Al galvanic system, which implies that the bond corrosion does not continuously proceed as a four-metal galvanic system.

Due to the encapsulation, galvanic corrosion occurs through a thin layer of electrolyte at the mold-bond interface. The high ohmic resistance significantly shortens the ion conducting path. Therefore, the galvanic corrosion is constrained at the interfaces between two adjacent entities. Based on the galvanic current and mass loss measurements on Cu-γ, γ-θ, and θ-Al couples in chapter 4, the galvanic corrosion rate between γ and θ was higher than that between Cu and γ as well as between θ and Al. The corrosion-induced crack should propagate much faster along the interface between γ and θ than the other two interfaces. This localized galvanic corrosion is not the only force driving the crack growth. A large area of residual alumina originating from the

surface oxide on the Al pad has been consistently observed at the γ-θ interface. The bonding strength between γ and θ is much weaker in the alumina-occupied area. As the initially-formed θ layer is transformed to γ during the annealing process, the bond strength is further reduced due to the internal stress buildup caused by the volumetric shrinkage. The weakened γ-θ interface is prone to electrolyte seeping-in and the resulting corrosion-induced crack propagation. Therefore, it is highly likely that the bond failure happens at the γ-θ interface first. This failure results in the formation of two separate galvanic couples: Cu-γ and θ-Al. As shown in chapter 4 through polarization analysis, for the Cu-γ couple, the corrosion rate of γ the anode is significantly accelerated by the strong galvanic effect imposed by the much larger area of Cu the cathode. For the θ-Al couple, the corrosion rate of Al the anode is not significantly affected due to the much smaller area of θ the cathode. Thus γ appears to be preferentially attacked. This explained the disappearance of γ from the ball-bond interface during the humidity-related reliability tests.

Chapter 5 discussed the Pd and chloride concentration effect on the bond failure mechanism and failure rate using the similar electrochemical techniques introduced in previous chapters. The findings explained the corrosion-mitigating mechanism of using CuPd wire and a green molding compound. Neither chloride concentration nor Pd addition changes the ball-bond failure behavior in terms of the initial failure at the γ-θ interface and the subsequent disappearance of γ. However, chloride concentration and Pd addition affect the bond failure rate in different ways. Lowering chloride concentration reduced the galvanic corrosion rate between the two adjacent entities. Therefore, using a low-chloride molding compound is beneficial for long-term service reliability of the wire bonds. Based on the XRD analysis, Pd can be homogeneously incorporated into γ but not into θ. Pd in γ increased the galvanic corrosion rate between γ and θ. However, Pd inhibits the IMC growth and the associated internal stress buildup. The more significant effect of latter

factor explains the improved humidity reliability of CuPd wire bonded packages. Chapter 5 also shows that the galvanic effect between Cu and γ can be eliminated by simultaneously reducing the chloride concentration and increasing the Pd addition, as shown in the minimal galvanic corrosion between Cu-9Pd and γ #3 in a 1ppm NaCl solution. This implies that annealing and transforming the original four-metal bond interface to a two-metal interface consisting of only the Pd-enriched Cu and Pd-enriched γ can be an effective method to mitigate the bond corrosion rate.

6.2 Recommendations

Electrochemical characterizations were conducted using bulk samples fully-immersed in bulk electrolytes in this dissertation. But, it would be beneficial to monitor the in-situ electrochemical behavior of these entities along a real Cu-Al bonding interface in a thin layer electrolyte. The gained knowledge would be critical in verifying the proposed corrosion mechanism. A Cu-Al bonding interface can be formed by joining a Cu and an Al sheet together through diffusion bonding. This composite specimen can then be sliced, ground, and polished to expose the composite interfacial structure. The microstructure and chemical information of the IMC layers can be identified via scanning electron microscopy with energy dispersive X-ray spectroscopy (SEM/EDS). The in-situ electrochemical behavior of the metallic entities and the metal-metal interfaces in a thin layer electrolyte can be studied using scanning electrochemical microscopy (SECM). Various noble metal, such as Pd, Au, and Ag, can be doped into the Cu and the Al sheet to simulate the metallurgy modification on the Cu wire and Al pad. Effect of these modifying elements on the IMC growth, interfacial defects, and corrosion behavior are evaluated to find the optimal corrosion-inhibiting strategies.

APPENDICES

APPENDIX A: Electrochemical Characterizations of Cu-Ni Alloy and Ni-doped γ

A.1 Rationale and objectives

Like Pd, Ni has high corrosion resistance, and it can form an isomorphous solution with Cu [16]. Ni is much more cost-effective than Pd as a coating material. Therefore, electrochemical studies on the Cu-Ni alloy and Ni-doped γ were carried out using the same techniques as introduced in chapter 3.

Ni is much harder than Pd. Therefore, Ni addition can significantly increase the hardness of the FAB. An increasing FAB hardness can cause Al splash or even damage the dielectric layer beneath the Al pad during the bonding process. Therefore, a high amount of Ni addition is not recommended. As shown in Table A.1, the Vickers hardness of a Cu-Ni alloy containing only 1 wt.% Ni (Cu-1Ni) is already higher than that of a Cu-Pd alloy containing 9 wt.% Pd. Therefore, only the Cu-1Ni alloy and the corresponding Ni-doped IMCs were studied.

Table A.1 Vickers hardness of the Cu-Ni and Cu-Pd alloys

Samples	Vickers hardness (MPa)
Cu	~ 370
Cu-2Pd	~ 420
Cu-9Pd	~ 550
Cu-1Ni	~ 690

A.2 Preparation of Ni-doped IMCs and Phase Verification

As the synthesis of Pd-doped IMCs, similar two-step procedures were used to prepare Ni-doped γ and θ. The Cu-1Ni alloy was prepared first using the arc-melting process. The Cu-1Ni alloy was then melted with the appropriated amounts of Al to prepare the Ni-doped γ and θ. The crystal structure of the as-prepared Ni-doped IMCs was verified using powder XRD analysis. The XRD spectra of Ni-doped γ and θ IMCs are provided in Fig. A.1.

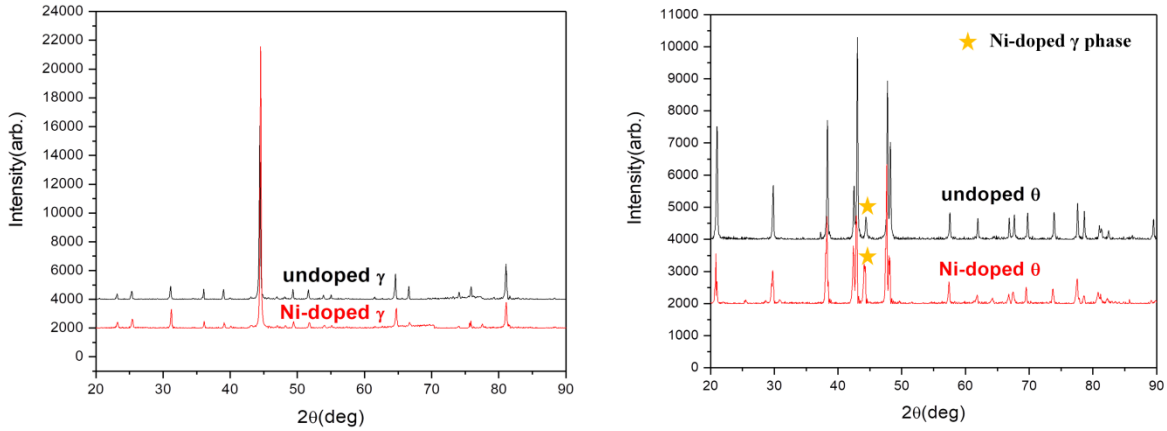

(a) (b)

Figure A.1 XRD spectra of powdered Ni-doped (a) γ and (b) θ; the powder was made from the as-produced samples via arc melting. Ni-doped IMCs were prepared using the Cu-1Ni alloy.

For γ, the XRD spectra of Ni-doped γ matched well with that of undoped γ. Additionally, since Ni has a similar atomic size with Cu, the incorporation of Ni in IMCs did not cause a visible peak shift as observed for Pd-doped IMCs in chapter 3. This result indicates that Ni can be homogenously incorporated in γ like Pd. On the contrary, the Ni-doped θ was not homogenous based on the XRD spectra. The height of the peak corresponding to the γ phase increased with the Ni addition. This indicates that Ni prefers to enrich in γ instead of θ like Pd.

A.3 Polarization behavior of Cu-Ni alloy and Ni-doped γ

Since Ni prefers to enrich in Cu and γ, the polarization curves of Cu-Ni alloy and Ni-doped γ were measured in a near neutral 20ppm NaCl solution and shown in Fig. A.2 and Fig. A.3, respectively. Apparently, the Ni addition did not cause a significant change in either the anodic or the cathodic current density. This might be due to the low Ni concentration in both Cu and γ such that its high corrosion resistance cannot be fully revealed. Unfortunately, the Ni addition cannot be increased significantly due to the hardness concern. Replacing Pd with Ni as the coating material might not be practical at this point.

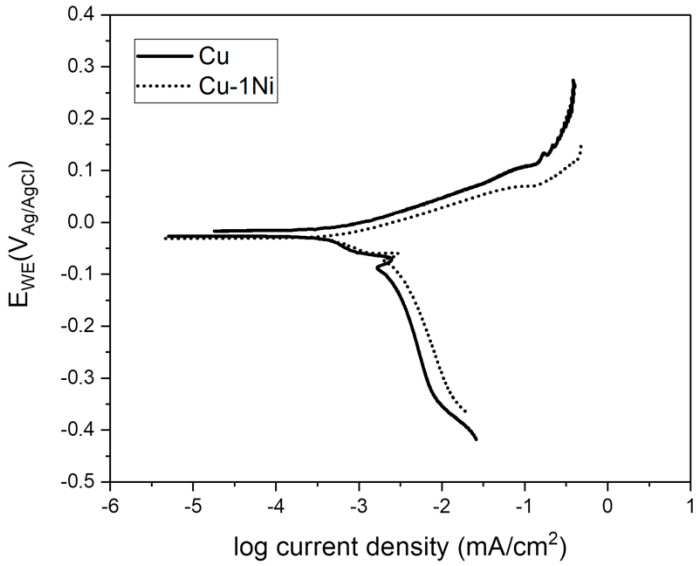

Figure A.2 Anodic and cathodic polarization curves of Cu and Cu-1Ni alloy measured in a pH 6, 20ppm NaCl solution

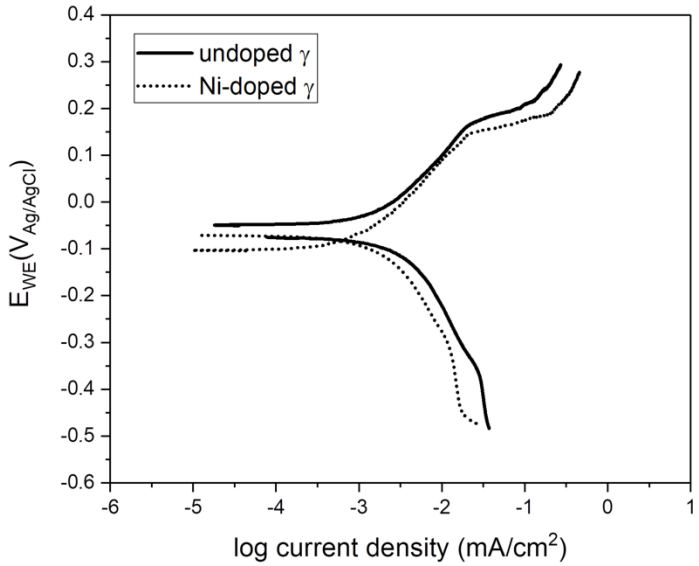

Figure A.3 Anodic and cathodic polarization curves of undoped γ and Ni-doped γ measured in a pH 6, 20ppm NaCl solution. The Ni-doped γ was prepared using Cu-1Ni alloy.

APPENDIX B: Pd Effect on the Electrochemical Behavior of Cu and γ in a Bromide-containing Solution

B.1 Rationale and Objectives

Besides chloride, bromide is the most common corrosive species in conventional molding compounds [22,40]. Although the bromide content in the molding compound has been minimized by using bromide-free flame retardant, the electrochemical corrosion behavior of Pd-doped entities in a bromide-containing electrolyte should be characterized to see if Pd addition can improve the resistance of the ball-bond interface to bromide-induced corrosion. In this study, the anodic and cathodic polarization curves of Pd-doped Cu and γ were measured in a pH 6, 20ppm NaBr solution.

B.2 Results and Discussion

The anodic and cathodic polarization curves of Cu, Cu-2Pd, and Cu-9Pd measured in a pH 6, 20ppm NaBr solution was shown in Fig. B.1. Due to the high catalytic activity of Pd to the cathodic reactions, the cathodic current density was significantly increased with only 2 wt.% Pd addition in Cu. As the Pd addition increased from 2 wt.% to 9 wt.% in Cu, the increase in the cathodic current density was not as significant. The appearance of the plateaus on the cathodic polarization curves of Cu-2Pd and Cu-9Pd indicates that the cathodic reaction, predominantly ORR, was limited by the oxygen diffusion at higher cathodic overpotentials. Pd addition reduced the anodic current density of Cu consistently.

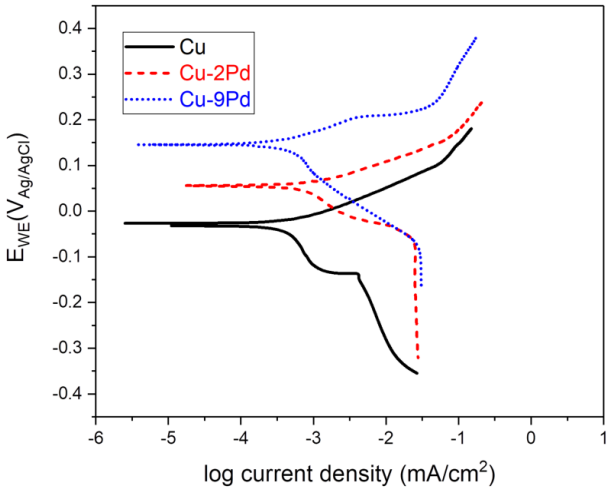

Figure B.1 Anodic and cathodic polarization curves of Cu, Cu-2Pd, and Cu-9Pd measured in a pH 6, 20ppm NaBr solution.

The anodic and cathodic polarization curves of γ #1, γ #2, and γ #3 measured in a pH 6, 20ppm NaBr solution was shown in Fig. B.2. The cathodic current density increased with the increasing Pd addition in γ. Interestingly, the anodic current density was not as sensitive to Pd addition as the cathodic current density. This might be due to the less aggressiveness of bromide as compared with chloride in attacking the surface passivation of γ.

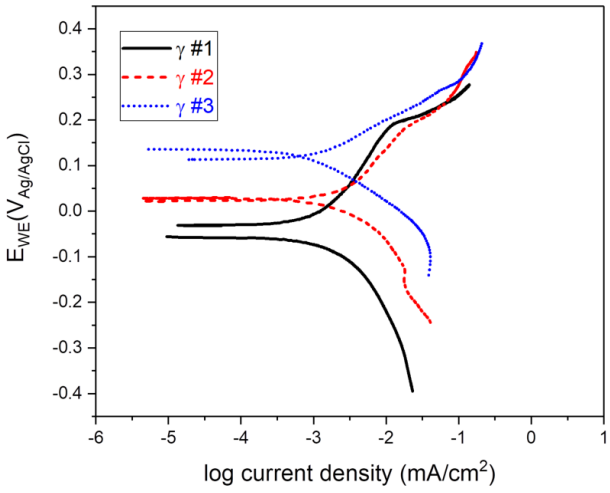

Figure B.2 Anodic and cathodic polarization curves of γ #1, γ #2, and γ #3 measured in a pH 6, 20ppm NaBr solution.

APPENDIX C: Electrochemical Behavior of (Pd-doped) Cu and γ in a Water Extract of the Molding Compound

C.1 Rationale and Objectives

Water extract of the molding compound can better represent the real chemistry environment inside the molding compound than electrolytes with controlled chloride concentrations and pH values. Therefore, electrochemical behavior of (Pd-doped) Cu and γ were also evaluated using the prepared water extract.

C.2 Experimental Details

The grinded powder of an epoxy-based molding compound was provided by the Freescale Semiconductor Company. 10 grams of the powder and 100mL pure water were mixed well and sealed in a pressure glass tube. The glass tube was then placed in an oven with the temperature set at 121℃ for 24 hours. After 24 hours, the liquid was filtered to obtain the filtrate containing ions leached out from the molding compound. The filtrate was commonly referred to as the water extract of EMC by the IC packaging industry. the pH of the water extract was measured first and estimated as 6.5. The electrolyte resistance was measured using the same current interrupt method introduced in chapter 2 and shown in Table C.1. Values of the electrolyte resistance of 100ppm, 20ppm, and 1ppm NaCl solutions at near neutral pH were also listed. Apparently, the electrolyte resistance of the water extract was close to that of a pH 6, 20ppm NaCl solution. Therefore, the polarization behavior of (Pd-doped) Cu and γ measured in the water extract should be compared with that measured in a 20ppm NaCl solution. However, the chloride concentration in the water extract was found to be much less than 20ppm. Therefore, the polarization curves measured in the water extract were compared with those measured in both 20ppm NaCl and 1ppm NaCl solutions as shown in Fig. C.1s and Fig. C.2s.

Table C.1 Comparison of measured solution resistance

Solution	Solution resistance (Ω)
100ppm NaCl (pH=5.8)	4530
20ppm NaCl (pH=5.8)	23840
1ppm NaCl (pH=5.8)	231000
Water extract of EMC (pH=6.5)	20700

C.3 Results and Discussion

As introduced in chapter 3, the small peak on the cathodic polarization curve of Cu was due to the reduction of CuCl formed during the pre-immersion period. This small peak disappeared in a 1ppm NaCl solution due to the less formation of CuCl. This peak was also absent on the cathodic polarization curve of Cu measured in the water extract. This indicates that the chloride concentration in the water extract should be much less than 20ppm although the water extract has a similar electrolyte resistance with a 20ppm NaCl solution.

The cathodic current density was not as sensitive to the electrolyte condition as the anodic current density as shown in Fig. C.1. The anodic current density of Cu measured in the water extract was lower than that measured in a 1ppm NaCl solution. The anodic current densities of Cu-2Pd and Cu-9Pd measured in the water extract were not consistently lower than those measured in a 1ppm NaCl solution, but, significantly lower than those measured in a 20ppm NaCl solution.

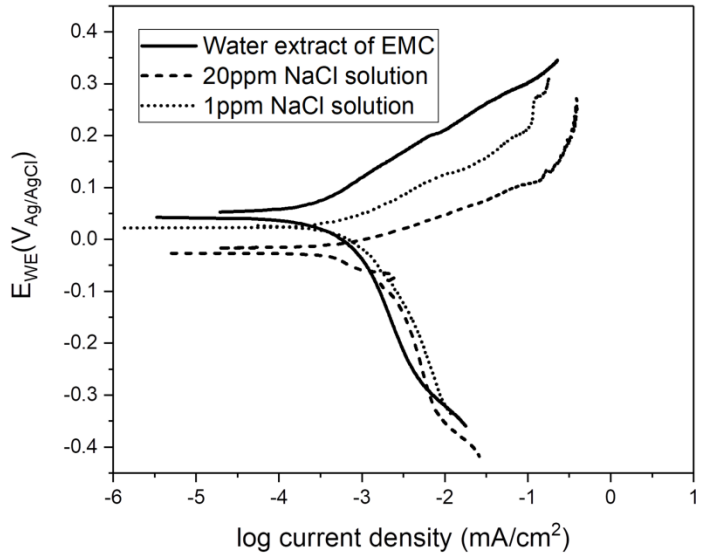

(a)

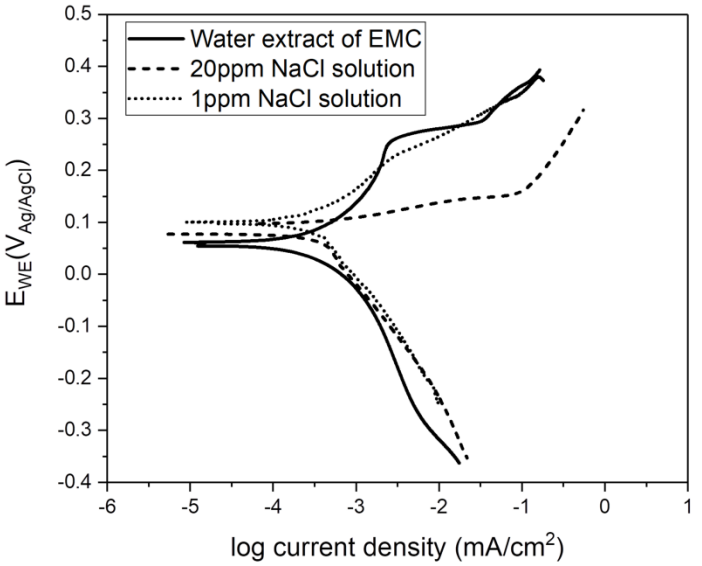

(b)

Figure C.1 Anodic and cathodic polarization curves of (a) Cu, (b) Cu-2Pd, and (c) Cu-9Pd measured in the water extract of EMC, 20ppm NaCl solution, and 1ppm NaCl solution.

Figure C.1 (cont'd)

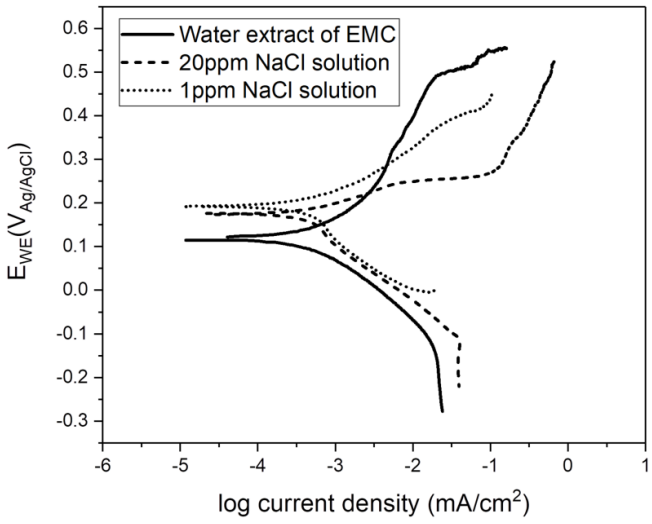

(c)

For γ IMCs, the anodic current densities measured in the water extract were all lower than those measured in a 20ppm NaCl solution. In addition, the cathodic current densities measured in the water extract were all significantly lower than those measured in 20ppm NaCl and 1ppm NaCl solutions.

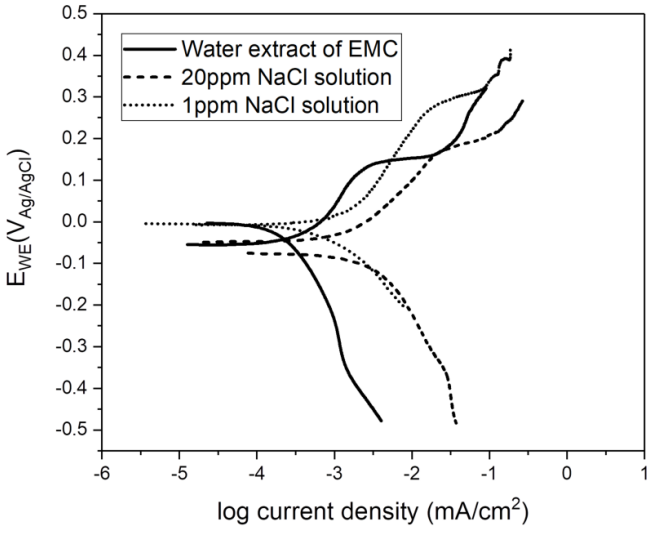

(a)

Figure C.2 Anodic and cathodic polarization curves of (a) γ #1, (b) γ #2, and (c) γ #3 measured in the water extract of EMC, 20ppm NaCl solution, and 1ppm NaCl solution.

Figure C.2 (cont'd)

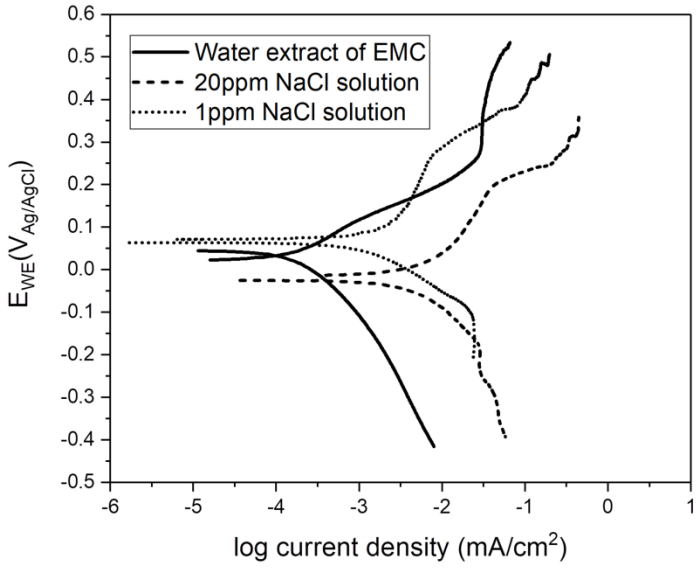

(b)

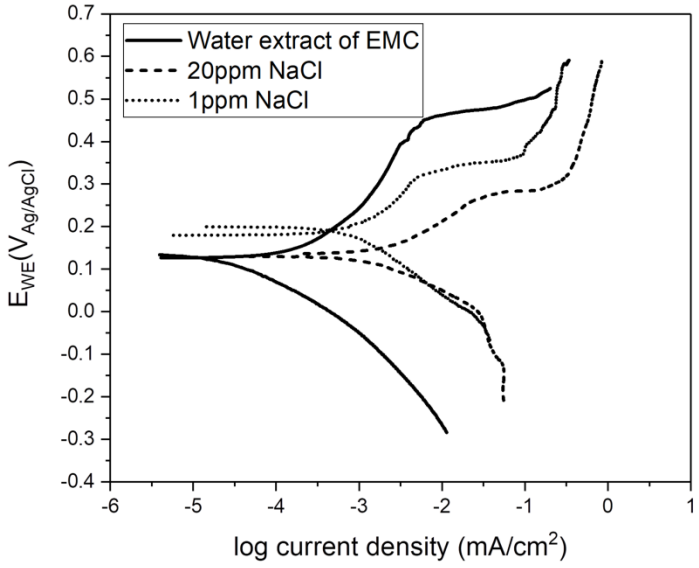

(c)

APPENDIX D: Galvanic Corrosion Rate between Adjacent Entities as Influenced by Oxygen

D.1 Rationale and Objectives

Oxygen content plays a significant role in the electrochemical corrosion behavior of metallic entities. Oxygen is directly involved in the cathodic reaction, namely ORR. Oxygen content also affects the surface passivation of Al [94]. Due to encapsulation, oxygen diffusion might not catch up with the cathodic reaction. In addition, as the crack propagates towards to the bond center region, oxygen might be depleted inside the crack zone due to a long oxygen diffusion path [95]. Thus, the galvanic corrosion rates between adjacent entities at the ball-bond interface were measured in an oxygen-free electrolyte. The oxygen in the electrolyte was removed by purging nitrogen for at least 2 hours before the tests.

C.2 Results and Discussion

As shown in Fig. D.1, for the undoped Cu-γ couple, lowering the oxygen content in the solution eliminated the galvanic effect since the measured i_g value approached zero. For the Pd-doped Cu-γ couples, lowering the oxygen content in the solution reversed the galvanic effect since the measured i_g value became negative. This indicates that CuPd alloy became the anode, while Pd-doped γ IMCs became the cathode in a low-oxygen solution. As shown in Fig. D.2, for all the γ-θ couples, lowering the oxygen content consistently reduced the galvanic corrosion rate between γ and θ.

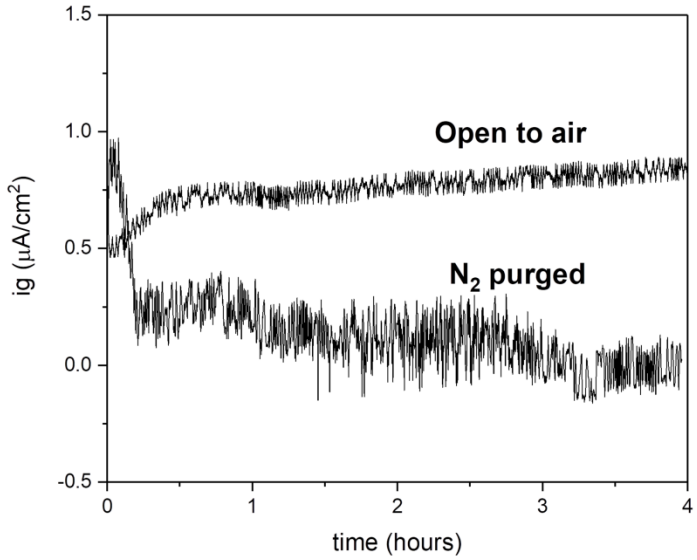

(a)

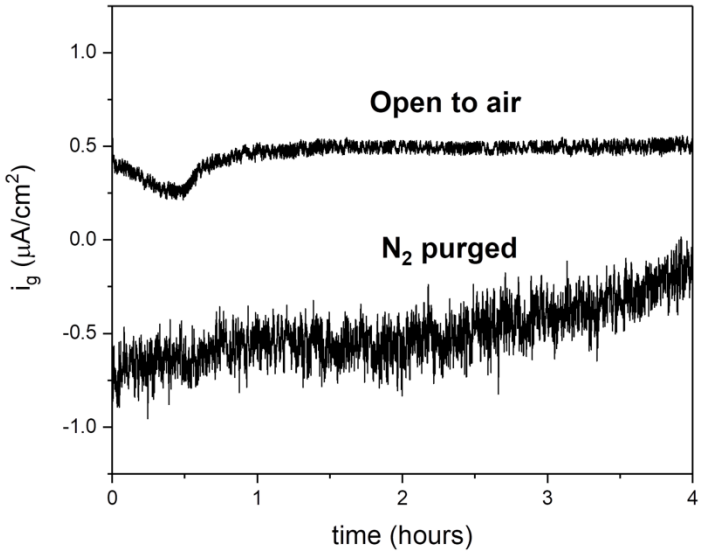

(b)

Figure D.1 Galvanic current density of (a) Cu:γ #1couple, (b) Cu-2Pd:γ #2 couple, and (c) Cu-9Pd:γ #3 couple in a 20ppm NaCl electrolyte open to air and purged with nitrogen.

Figure D.1 (cont'd)

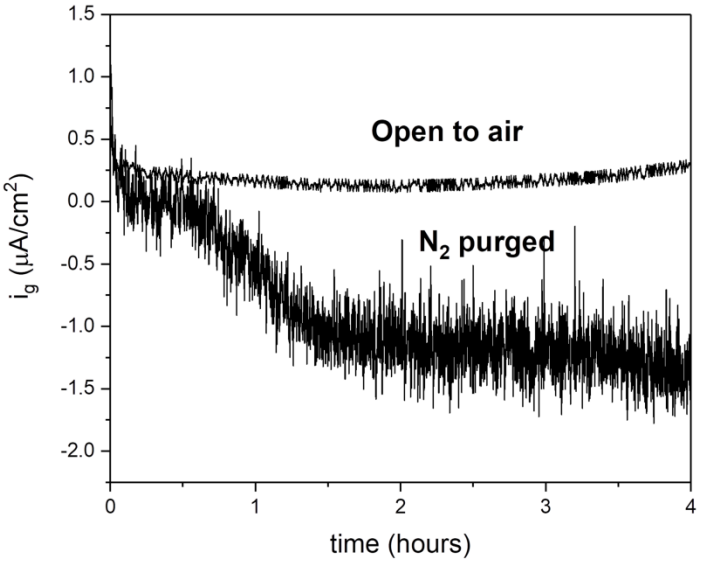

(c)

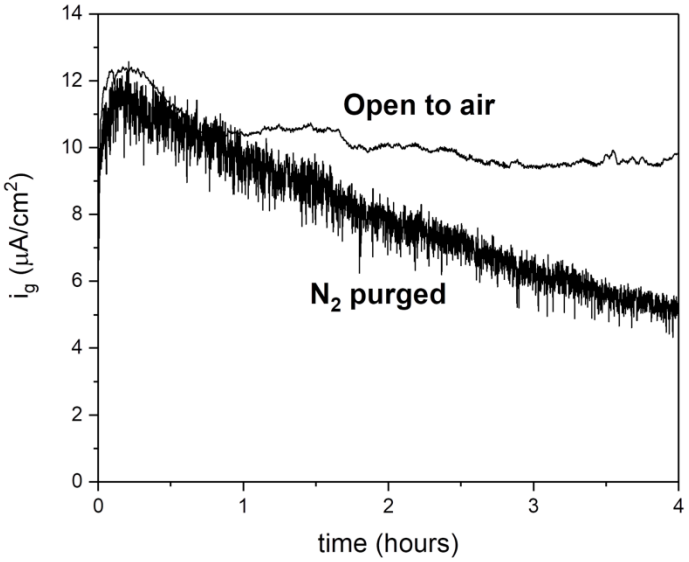

(a)

Figure D.2 Galvanic current density of (a) γ #1:θ couple, (b) γ #2:θ couple, and (c) γ #3:θ couple in a 20ppm NaCl electrolyte open to air and purged with nitrogen.

Figure D.2 (cont'd)

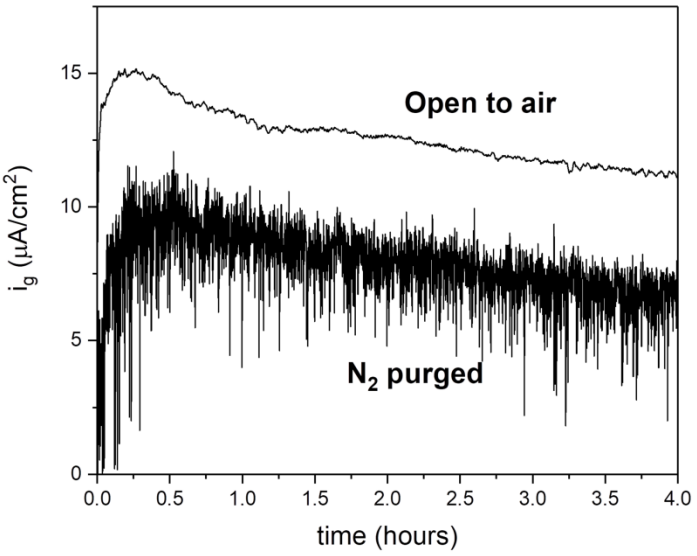

(b)

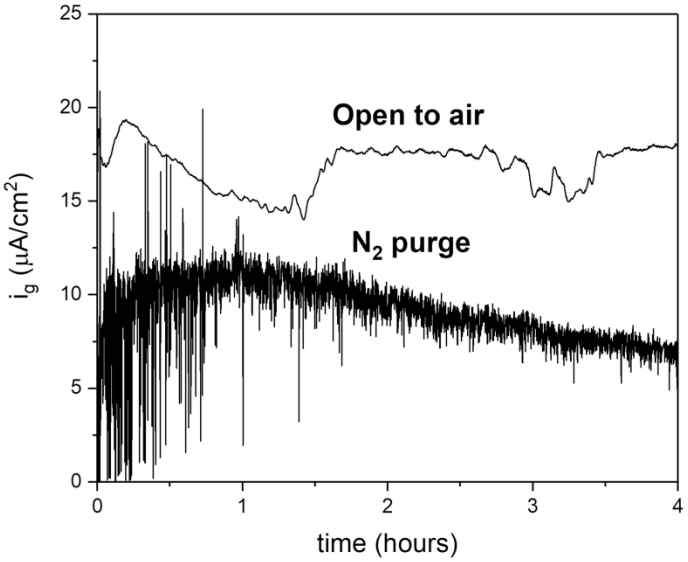

(c)

REFERENCES

REFERENCES

1. W. D. Brown: Introduction and overview of microelectronics packaging, in Advanced Electronic Packaging: With Emphasis on Multichip Modules, 1, Wiley-IEEE Press, 1999

2. P. S. Chauhan, A. Choubey, Z. W. Zhong, and M. G. Pecht: Copper wire bonding, Springer, New York, 2014, pp. 1-9

3. G. Harman: Wire bonding in microelectronics, McGraw-Hill, 2010, pp. 23-26

4. J. H. Lau: Recent advances and new trends in flip chip technology. ASME. J. Electron. Packag. 2016, 138(3), 030802

5. G. Harman: Wire bonding in microelectronics, McGraw-Hill, 2010, pp. 63-67

6. Z. Zhang and C. P. Wong: Recent advances in flip-chip underfill: materials, process, and reliability, IEEE Transactions on Advanced Packaging, 27(3), 2004, pp. 515-524

7. S. Holzinger and B. Sharenow: Advantages of a floating annular ring in three-layer tab assembly, IEEE Transactions on Components, Hybrids, and Manufacturing Technology, 10(3), 1987, pp. 332-334.

8. R. R. Tummala, E. J. Rymaszewski, and A. G. Klopfenstein: Microelectronics packaging handbook, Springer, pp. 220-221, 1997

9. R. R. Tummala, E. J. Rymaszewski, and A. G. Klopfenstein: Microelectronics packaging handbook, Springer, pp. 72-73, 1997

10. P. Elenius and L. Levin: Comparing flip-chip and wire-bond interconnection technologies, Chip Scale Review, July/August 2000

11. R. R. Tummala, E. J. Rymaszewski, and A. G. Klopfenstein: Microelectronics packaging handbook, Springer, pp. 272-273, 1997

12. G. Hu: Comparison of copper, silver and gold wire bonding on interconnect metallization, 2012 13th International Conference on Electronic Packaging Technology & High Density Packaging, Guilin, 2012, pp. 529-533

13. P. Liu, L. Tong, J. Wang, L. Shi, and H. Tang: Challenges and developments of copper wire bonding technology, Microelectronics Reliability, 52, pp. 1092–1098, 2012

14. C. Hang, C. Wang, M. Shi, X. Wu, and H. Wang: Study of copper free air ball in thermosonic copper ball bonding, in Electronic Packaging Technology, 2005 6th International Conference, 2005, pp. 414–418

15. P. S. Chauhan, A. Choubey, Z. W. Zhong, and M. G. Pecht: Copper wire bonding. Springer, New York, 2014, pp.39-45

16. Kejun Zeng, Wei Qun Peng, Corrosion-resistant copper-to-aluminum bonds, US20120001336, Jan 5, 2012

17. P. S. Chauhan, A. Choubey, Z. W. Zhong, and M. G. Pecht: Copper wire bonding. Springer, New York, 2014, pp.112

18. J. Foley, H. Clauberg, and B. Chylak: Enabling high volume fine pitch copper wire bonding: enhancements to process and equipment capability, in Electronic System-Integration Technology Conference (ESTC), 2010, pp. 1–4

19. P. S. Chauhan, A. Choubey, Z. W. Zhong, and M. G. Pecht: Copper Wire Bonding. (Springer, New York, 2014), pp.18-37

20. R. B. Comizzoli, R. P. Frankenthal, K. J. Hanson, K. Konstadinidis, R. L. Opila, J. Sapjeta, J. D. Sinclair, K. M. Takahashi, A. L. Frank, and A. O. Ibidunni: Electrochemical aspects of corrosion resistance and etching of metallizations for microelectronics. Mater. Sci. Eng., A, 198(1), 153-160, 1995

21. S. H. Kim, J. W. Park, S. J. Hong and J. T. Moon, The interface behavior of the Cu-Al bond system in high humidity conditions, in proceedings of the 2010 12th Electronic Components and Technology Conference (ECTC), Singapore, 2010, pp. 545–549

22. T. Uno: Bond reliability under humid environment for coated copper wire and bare copper wire, *Microelectron reliab.*, 51(1), 148-156, 2011

23. P. Su, H. Seki, C. Ping, S. Zenbutsu, S. Itoh, L. Huang, N. Liao, B. Liu, C. Chen, W. Tai, and A. Tseng: An evaluation of effects of molding compound properties on reliability of Cu wire components. *2011 IEEE 61st Electronic Components and Technology Conference (ECTC)*, 2011, pp. 363-369

24. J. Jeon et al.: High Reliability Challenges with Cu Wire Bonding for Automotive Devices in the AEC-Q006, 2017 IEEE 67th Electronic Components and Technology Conference (ECTC) in Orlando, FL, 2017, pp. 1968-1973

25. P. S. Chauhan, A. Choubey, Z. W. Zhong, and M. G. Pecht: Copper Wire Bonding, Springer, New York, 2014, pp.72-73

26. P. S. Chauhan, A. Choubey, Z. W. Zhong, and M. G. Pecht: Copper Wire Bonding, Springer, New York, 2014, pp. 92-93

27. L. England and T. Jiang: Reliability of Cu Wire Bonding to Al Metallization, 2007 Proceedings 57th Electronic Components and Technology Conference, Reno, NV, 2007, pp. 1604-1613

28. C. L. Gan, C. Francis, B. L. Chan, and U. Hashim: Extended reliability of gold and copper ball bonds in microelectronic packaging, Gold Bull, 2013, 46(2), pp. 103-115

29. F. W. Wulff, C. D. Breach, D. Stephan, Saraswati, and K. J. Dittmer: Characterization of intermetallic growth in copper and gold ball bonds on aluminum metallization, in Electronics Packaging Technology Conference, EPTC 2004, pp. 348–353

30. H. Xu, C. Liu, V. V. Silberschmidt, S. S. Pramana, T. J. White, Z. Chen, and V. L. Acoff: New mechanisms of void growth in Au-Al wire bonds: volumetric shrinkage and intermetallic oxidation," Scripta Materialia, 65, pp. 642–645, 2011

31. H. Xu, C. Liu, V. V. Silberschmidt, S. S. Pramana, T. J. White, Z. Chen, and V. L. Acoff: Behavior of aluminum oxide, intermetallics and voids in Cu–Al wire bonds, Acta Materialia, 59, pp. 5661–5673, 2011

32. S. Murali, N. Srikanth, and C. J. Vath III, An analysis of intermetallics formation of gold and copper ball bonding on thermal aging, Materials Research Bulletin, 38, pp. 637–646, 2003

33. L. Lantz, S. Hwang, and M. Pecht: Characterization of plastic encapsulant materials as a baseline for quality assessment and reliability testing, Microelectron reliab., 42(8), 1163-1170, 2002

34. J. W. Oldfield: Electrochemical Theory of Galvanic Corrosion. Galvanic Corrosion, H. Hack, Ed., ASTM International, West Conshohocken, PA, 1988, 5-22

35. ASTM G82-98 Standard Guide for Development and Use of a Galvanic Series for Predicting Galvanic Corrosion Performance, ASTM International, West Conshohocken, PA, 1998

36. A. B. Y. Lim, W. J. Neo, O. Yauw, B. Chylak, C. L. Gan, and Z. Chen: Evaluation of the corrosion performance of Cu–Al intermetallic compounds and the effect of Pd addition. Microelectron reliab., 56, 155–161, 2016

37. T. Boettcher, M. Rother, S. Liedtke, M. Ullrich, M. Bollmann, A. Pinkernelle, D. Gruber, H. Funke, M. Kaiser, K. Lee, M. Li, K. Leung, T. Li, M. L. Farrugia, O. Halloran, M. Petzold, B. Marz, and R. Klengel: On the intermetallic corrosion of Cu-Al wire bonds, 2010 12th Electronics Packaging Technology Conference, 585–590, 2010

38. B. Mazurkiewicz and A. Piotrowski: The electrochemical behavior of the Al_2Cu intermetallic compound, Corros. Sci., 23(7), pp. 697-707, 1983

39. N. Birbilis and R. G. Buchheit: Electrochemical characteristics of intermetallic phases in aluminum alloys: an experimental survey and discussion, J. Electrochem. Soc., 152(4), B140-B151, 2005

40. H. Xu, I. Qin, H. Clauberg, B. Chylak, V. L. Acoff: Behavior of palladium and its impact on intermetallic growth in palladium-coated Cu wire bonding, Acta Materialia, 61(1), pp. 79-88, 2013

41. J. H. Potgieter: Alloys cathodically modified with noble metals. Journal of Applied Electrochemistry, 471-482, 1991

42. L. J. Tang, H. M. Ho, Y. J. Zhang, Y. M. Lee, and C. W. Lee, Investigation of palladium distribution on the free air ball of Pd-coated Cu wire, in Electronics Packaging Technology Conference (EPTC), 2010, pp. 777–782

43. H. Clauberg, B. Chylak, N. Wong, J. Yeung, and E. Milke: Wire bonding with Pd-coated copper wire, in CPMT Symposium Japan, IEEE, 2010, pp. 1–4

44. L. J. Tang, H. M. Ho, W. Koh, Y. J. Zhang, K. S. Goh, C. S. Huang, and Y. T. Yu: Pitfalls and solutions of replacing gold wire with palladium coated copper wire in IC wire bonding, in Electronic Components and Technology Conference (ECTC), 2011, pp. 1673–1678

45. Y. W. Lin, W. B. Ke, R. Y. Wang, I. S. Wang, Y. T. Chiu, K. C. Lu, K. L. Lin, and Y. S. Lai, The influence of Pd on the interfacial reactions between the Pd-plated Cu ball bond and Al pad, Surf. Coat. Technol., 231, pp. 599-603, 2013

46. P. Ratchev, S. Stoukatch, and B. Swinnen: Mechanical reliability of Au and Cu wire bonds to Al, Ni/Au and Ni/Pd/Au capped Cu bond pads, Microelectron reliab., 46, pp. 1315–1325, 2006

47. A. B.Y. Lim, C. B. Boothroyd, O. Yauw, B. Chylak, C. L. Gan, and Z. Chen: Interfacial evolution and bond reliability in thermosonic Pd coated Cu wire bonding on aluminum metallization: Effect of palladium distribution, Microelectron reliab., 63, pp. 214-223, 2016

48. H. Liu, Z. Zhao, Q. Chen, J. Zhou, M. Du, S. Kim, J. Chae, and M. Chung: Reliability of copper wire bonding in humidity environment, in Electronics Packaging Technology Conference (EPTC), 2011, pp. 53–58

49. F. Kawashiro et al.: Reliability of copper wire bonds on a novel over-pad metallization, Jpn. J. Appl. Phys., 54, 05EC01, 2015

50. L. Lantz and M. G. Pecht: Ion transport in encapsulants used in microcircuit packaging, in IEEE Transactions on Components and Packaging Technologies, 26(1), pp. 199-205

51. Z. S. Smialowska, Pitting corrosion of aluminum, Corros. Sci., 41(9), pp. 1743-1767, 1999

52. G. Kear, B. D. Barker, and F. C. Walsh: Electrochemical corrosion of unalloyed copper in chloride media-a critical review. Corros. Sci., 46(1), 109-135, 2004

53. C. L. Gan, E. K. Ng, B. L. Chan, U. Hashim, and F. C. Classe, Technical barriers and development of Cu wire bonding in nano-electronics device packaging, J. Nanomater., 173025, 7 pages, 2012

54. Y. T. Chiu, T. H. Chiang, Y. F. Chen, P. F. Yang, L. Huang and K. L. Lin: The corrosion performance of Cu alloy wire bond on Al pad in molding compounds of various chlorine contents under biased-HAST, 2014 IEEE 64th Electronic Components and Technology Conference (ECTC), Orlando, FL, 2014, pp. 419-424

55. Y. Zeng, K. Bai, and H. Jin: Thermodynamic study on the corrosion mechanism of copper wire bonding. Microelectron. reliab., 53(7), 985–1001, 2013

56. T. J. L. Yap, Y. K. Au, and P. L. Eu: Importance of Cu/Al intermetallic coverage in copper wire bonding with sensitive pad structure, 2012 14th International Conference on Electronic Materials and Packaging (EMAP), Lantau Island, 2012, pp. 1-5

57. C. S. Goh, W. L. E. Chong, T. K. Lee and C. Breach, Corrosion study and intermetallics formation in gold and copper wire bonding in microelectronics packaging, Crystals, 3(3), 391-404, 2013

58. T. K. Lee, C. D. Breach, W. L. Chong and C. S. Goh: Oxidation and corrosion of Au/Al and Cu/Al in wire bonding assembly, 2012 13th International Conference on Electronic Packaging Technology & High Density Packaging, Guilin, 2012, pp. 244-249

59. G. S. Frankel. Electrochemical Techniques in Corrosion: Status, Limitations, and Needs, Journal of ASTM International, 5(2), 1–27, 2008

60. ASTM G215-17 Standard Guide for Electrode Potential Measurement, ASTM International, West Conshohocken, PA, 2017

61. Different Forms of Corrosion Classified on the Basis of Appearance. In: Bardal E. (eds) Corrosion and Protection. Engineering Materials and Processes. Springer, London, 2004, pp 122-131

62. ASTM G5-14 Standard Reference Test Method for Making Potentiodynamic Anodic Polarization Measurements, ASTM International, West Conshohocken, PA, 2014

63. W. C. Ehrhardt: IR drop in electrochemical corrosion studies-Part I: Basic concepts and estimates of possible measurement errors, The Measurement and Correction of Electrolyte Resistance in electrochemical Tests, ASTM STP 1056, L. L. Scribner and S. R. Taylor, Eds., American Society for Testing and Materials, Philadelphia, 1990, pp. 27-58

64. Ehrhardt, W. C., "IR Drop in Electrochemical Corrosion Studies-Part 2: A Multiple Method IR Compensation System," The Measurement and Correction of Electrolyte Resistance in Electrochemical Tests, ASTM STP 1056, L. L. Scribner and S. R. Taylor, Eds., American Society for Testing and Materials, Philadelphia, 1990, pp. 78-94

65. M. Mokaddem, P. Volovitch, F. Rechou, R. Oltra, K. Ogle: The anodic and cathodic dissolution of Al and Al-Cu-Mg alloy, Electrochimica Acta, 55(11), pp. 3779-3786, 2010

66. K. Ogle, M. Serdechnova, M. Mokaddem, P. Volovitch: The cathodic dissolution of Al, Al_2Cu, and Al alloys, Electrochimica Acta, 56(4), pp. 1711-1718, 2011

67. X.L. Zhang, Zh.H. Jiang, Zh.P. Yao, Y. Song, Zh.D. Wu: Effects of scan rate on the potentiodynamic polarization curve obtained to determine the Tafel slopes and corrosion current density, Corros. Sci., 51(3), pp. 581-587, 2009

68. ASTM G3-14 Standard Practice for Conventions Applicable to Electrochemical Measurements in Corrosion Testing, ASTM International, West Conshohocken, PA, 2014

69. F. King, M. J. Quinn, C. D Litke: Oxygen reduction on copper in neutral NaCl solution, J. Electroanal. Chem., 385(1), pp. 45-55, 1995

70. ASTM G71-81 Standard Guide for Conducting and Evaluating Galvanic Corrosion Tests in Electrolytes, ASTM International, West Conshohocken, PA, 2014

71. D. Larcher, L. Y. Beaulieu, O. Mao, A. E. George, J. R. Dahn: Study of the reaction of lithium with isostructural A_2B and various Al_xB alloys, J. Electrochem. Soc., 147(5), 1703-1708, 2000

72. C. Deslouis and B. Tribollet: Electrochemical behavior of copper in neutral aerated chloride solution. I. Steady-state investigation. J. Appl. Electrochem., 18, 374-383, 1988

73. J. R. Scully, T. O. Knight, R. G. Buchheitt, and D. E. Peeblest: Electrochemical Characteristics of the Al_2Cu, Al_3Ta and Al_3Zr Intermetallic Phases and Their Relevancy to the Localized Corrosion of Al Alloys, Corros. Sci., 35, pp. 185-195, 1993

74. Electrode Kinetics. In: Bardal E. (eds) Corrosion and Protection. Engineering Materials and Processes. Springer, London, 2004, pp 40

75. T. Hurlen, H. Lian, O. S. Ødegard, and T. Valand: Corrosion and passive behavior of aluminum in weakly acid solution, Electrochim. Acta. 29(5), 579, 1984

76. R. T. Foley, and T. H. Nguyen: The Chemical Nature of Aluminum Corrosion, J. Electrochem. Soc., 129(3), 464–467, 1982

77. N. Birbilis and R. G. Buchheit: Investigation and Discussion of Characteristics for Intermetallic Phases Common to Aluminum Alloys as a Function of Solution pH, J. Electrochem. Soc., 155(3), pp. C117-C126, 2008

78. J. Osenbach, B. Q. Wang, S. Emerich, J. DeLucca and D. Meng: Corrosion of the Cu/Al interface in Cu-Wire-bonded integrated circuits, 2013 IEEE 63rd Electronic Components and Technology Conference, Las Vegas, NV, 2013, pp. 1574-1586

79. J. Petro, T. Mallat, S. Szabo, and F. Hange, Anodic dissolution of palladium+copper alloys, *J Electroanal. Chem*., 160, pp. 289-297, 1984

80. Electrode Kinetics. In: Bardal E. (eds) Corrosion and Protection. Engineering Materials and Processes. Springer, London, 2004, pp. 36

81. F. Gobal and R. Arab: A preliminary study of the electro-catalytic reduction of oxygen on Cu–Pd alloys in alkaline solution. J. Electroanal. Chem., 647(1), pp. 66–73, 2010

82. J. Gniewek, J. Pezy, B. G. Baker, and J. O'M. Bockris: The effect of noble metal additions upon the corrosion of copper: an Auger-Spectroscopic study, *J. Electrochem. Soc.,* 125(1), pp. 17–23, 1978

83. H. W. Pickering: Characteristic features of alloy polarization curves, *Corros. Sci*, 23(10), pp. 1107–1120, 1983

84. Y. H. Lu, H. B. Xu, J. Wang, and X. F. Kong: Oxygen reduction mechanism on copper in a 0.5M H_2SO_4. Electrochim. Acta., 54(15), pp. 3972–3978, 2009

85. M. H. Ghandehari, and T. N. Andersen: The electrochemical reduction of oxygen on copper in dilute sulphuric acid solutions, Corros. Sci., 16, pp. 123–135, 1976

86. P. Han and D. M. Bartels: Temperature dependence of oxygen diffusion in H_2O and D_2O, J. Phys. Chem., 100 (13), pp. 5597-5602, 1996

87. N. Hackerman: Effect of temperature on corrosion of metals, Ind. Eng. Chem., 44 (8), pp. 1752-1755, 1952

88. P. S. Chauhan, A. Choubey, Z. W. Zhong, and M. G. Pecht: Copper wire bonding, Springer, New York, 2014, pp. 93

89. K. B. Deshpande: Numerical modeling of micro-galvanic corrosion, Electrochimica. Acta., 56(4), pp. 1737-1745, 2011

90. ASTM G102-89 Standard practice for calculation of corrosion rates and related information from electrochemical measurements, ASTM International, West Conshohocken, PA, 2015

91. Electrode Kinetics. In: Bardal E. (eds) Corrosion and Protection. Engineering Materials and Processes. Springer, London, 2004.

92. G. L. Song, Potential and current distributions of one-dimensional galvanic corrosion systems, Corros. Sci., 52(2), pp. 455-480, 2010

93. H. G. Kim, S. M. Kim, J. Young Lee, M. R. Choi, S. H. Choe, K. H. Kim, J. S. Ryu, S. Kim, S. Z. Han, W. Y. Kim, and S. H. Lim: Microstructural evaluation of interfacial intermetallic compounds in Cu wire bonding with Al and Au pads, *Acta Materialia*, 64, pp. 356-366, 2014

94. K. Jafarzadeh, T. Shahrabi, S. M. M. Hadavi, and M. G. Hosseini: Role of chloride ion and dissolved oxygen in electrochemical corrosion of AA5083-H321 aluminum-magnesium alloy in NaCl solutions under flow conditions, J. Mater. Sci. Technol., 23(5), 2007

95. G. S. Frankel: Pitting corrosion of metals: a review of the critical factors, J. Electrochem. Soc., 145(6), pp. 2186-2198, 1998